Thesis for the Degree of Doctor of Philosophy

Optical and biological responses of enhanced photothermal applications against cancer tissue

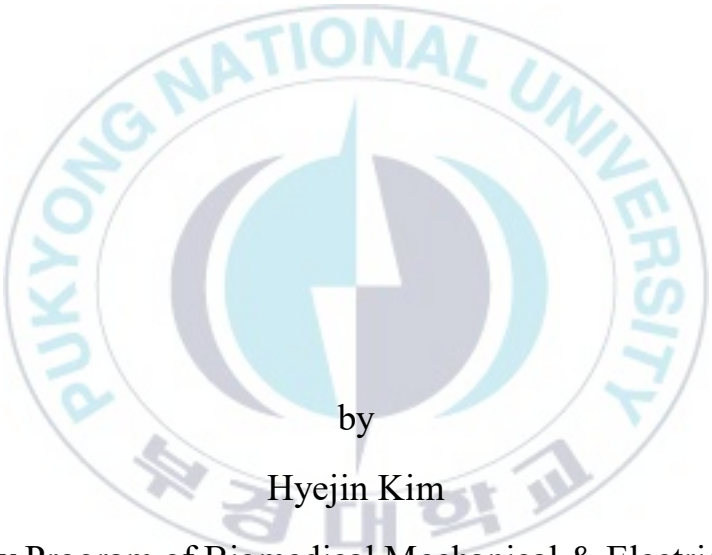

by

Hyejin Kim

Interdisciplinary Program of Biomedical Mechanical & Electrical Engineering

The Graduate School

Pukyong National University

February 2022

Optical and biological responses of enhanced photothermal applications against cancer tissue

(다양한 광열 어플리케이션을 이용한 암조직의 광학 및 생물학적 반응 연구)

Advisor: Prof. Hyun Wook Kang

by

Hyejin Kim

A thesis submitted in partial fulfillment of the requirements

for the degree of

Doctor of Philosophy

in Interdisciplinary Program of Biomedical Mechanical & Electrical Engineering, The Graduate School,

Pukyong National University

February 2022

Optical and biological responses of enhanced photothermal applications against cancer tissue

A dissertation

by

Hyejin Kim

Approved by:

(Chairman) Myunggi Yi Ph. D

(Member) Byeong-il Lee Ph.D

(Member) Songyi Lee Ph. D

(Member) Hyoung Shin Lee M.D

(Member) Hyun Wook Kang Ph. D

February 25, 2022

Optical and biological responses of enhanced photothermal applications against cancer tissue

Hyejin Kim

Interdisciplinary Program of Biomedical Mechanical & Electrical Engineering

The Graduate School

Pukyong National University

Abstract

현대사회에서 치명적인 사망원인 중 하나인 암은 현재 많은 기술이 발달했음에도 불구하고 여전히 완전한 치료를 기대하기 어려운 질병으로 손꼽히고 있다. 외과적 수술이나, 약물, 방사선, 면역치료와 같은 다양한 암 치료 관련 연구 및 개발로 생존율은 지속적으로 향상되고 있으나, 여전히 재발의 가능성이 높고 정상세포에까지 영향을 미치는 부작용은 남아있다. 최근 표적치료법으로써 레이저를 이용한 광열치료 (Photothermal therapy)가 유망한 암 치료법 중 하나로 여겨지고 있다. 광열치료란 레이저 빛을 광반응제에 조사하여 국소적으로 열을 발생시킴으로써 암세포의 사멸을 유도하는 치료법이다. 효과적인 광열치료를 위해서는 레이저로 인한 정상조직의 손상은 최소화하고 높은 열효율을 내는 것이 가장 중요하다고 볼 수 있다. 따라서 본 연구에서는 다양한 광반응제와 광학 응용법을 통한 효과적인 광열 암치료에 대해 조사하였다. 먼저 항암 물질인 독소루비신 (Doxorubicin)과 후코이단 (Fucoidan)이 합성된 금 나노입자를 이용하여 광열과 약물 치료가 통합된 안구 종양 치료 연구를 진행하였다. 제조된 나노입자는 생리적 환경에서 높은 안정성을 보이고 강한 광흡수율 및 열 변환 효율 때문에 광열 및 약물 효과 모두 발생시켜 종양을 완전히 제거할 수 있었다. 또한

유기합성물질 (NI2 NPs)를 이용하여 기존 유기물질의 한계점인 낮은 광안정성과 광열반응을 향상시켜 직장암치료에 대한 광열치료 효율을 높이고자 하였다. 실험 결과, 제안된 NI2 NPs 는 기존 유기물질과 비교하여 뛰어난 광안전성을 가지며 효과적인 광열 변환효율가지고 있었고, 직장암 세포 및 직장암 종양모델에서 대조군과 대비하여 뛰어난 암 치료 효과를 보였다. 그러나, 이러한 전형적인 광열치료에 사용되는 레이저 조사는 Gaussian 광 분포를 따른다. 이러한 분포는 종양에 전체적으로 고르게 분포되지 않고 중심에서 가장 큰 세기를 가지기 때문에 암이 잔류하게 될 가능성이 있어 균일한 열분포를 위한 광학적인 응용실험 또한 진행하였다. 먼저 같은 에너지 양에서 레이저 세기 조절을 이용하여 직장암 종양 모델의 광열치료 효과에 대하여 조사하였다. 강한 세기로 짧게 조사하는 경우, 전반적인 열손상은 넓게 나타나지만 종양내부 깊숙이 응고괴사를 유도하기에는 부족했고, 약한 세기로 오래 조사하는 경우는 충분한 온도 도달이 어려워 종양이 없어지지 않고 성장하는 효과를 보였다. 그러나 강한 세기로 일정기간 조사하고 약한 세기로 바꿔준 경우, 전반적인 열손상과 종양내부 깊숙이 응고괴사가 유도되는 것을 확인 할 수 있었다. 또한 Multi-lens arrays (MLA)를 이용한 마이크로빔 패턴을 이용하여 불균일한 전방 조사의 한계점을 보완할 수 있는 광열치료법 연구를 진행하였다. 그 결과, 전방형 광섬유보다 MLA 를 이용하여 조사하였을 때, 더 넓고 더 깊게 광분포를 나타내었고, 직장암 종양모델에서 또한 더 균일한 광열손상을 보여 효과적인 종양제거를 유도하였다. 이러한 실험 결과들은 임상적으로 사용할 수 있는 광열 암치료에 대한 다양한 방법을 제공하여 완전한 암치료에 대한 가능성을 제공하였다. 그러나, 이러한 광열치료 진행 시 잔여 암에 대해서 종양성장이 촉진되는 경향이 확인되어, 이러한 레이저 조사에 따른 종양성장 촉진 효과를 확인하기 위하여 다양한 파장대에 대한 종양 성장 매커니즘에 대하여 조사하였다. 직장암 마우스 모델을 제작하여 각각 405 nm, 635 nm, 808 nm 레이저를 조사하여 적출한 후 웨스턴 블랏 (Western blot), 실시간 중합효소연쇄반응 (qRT-PCR),

면역조직화학염색 (Immunohistochemistry)을 통하여 악성 증식 및 혈관 생성 관련 단백질 인자들을 정량분석 진행하였고, 그 결과 405 nm 레이저에서 가장 높은 촉진 효과를 관찰하였으며 그 다음 808 nm, 635 nm 순으로 촉진 효과를 확인할 수 있었다. 이러한 종양 촉진 매커니즘 연구를 통하여 레이저 치료에 대한 안전성 확보를 강조하였다. 결과적으로 본 연구에서는 다양한 나노입자와 에너지 전달법을 이용한 광열 치료는 효과적으로 암을 치료할 수 있는 방법 및 레이저 사용으로 인해 발생할 수 있는 광 자극 반응에 대한 안전역을 제공할 수 있었다. 추후 정확한 선택성과 영상 진단을 위한 나노입자 개발 및 다양한 광전달 응용법에 대한 연구를 통하여 치료 효율을 높여야 할 것으로 여겨진다.

Table of contents

List of Figures

List of Tables

Chapter 1. Introduction

1.1. Conventional cancer treatment

Over the decades, cancer has been considered as a leading cause of morbidity and mortality worldwide [1]. According to estimates of the World Health Organization (WHO) in 2019, cancer is the most lethal diseased, indicating that the enormous burden of health is increasing worldwide [2]. 19.3 million new cases and 10 million cancer death were estimated for both men and women worldwide in 2020 [2]. In fact, cancer is caused by uncontrolled cell growth of gene mutations within cells, eventually leading to cancer formation [3]. Since cancer occurs for various reasons, treatment options can be applied in various ways accordingly (Figure. 1). Traditionally, surgery have been widely used for cancer patients to remove tumor tissues physically [4, 5]. For early stage of cancer patients, radiotherapy is widely utilized as a non-invasive therapeutic method [6]. However, after surgery of radiotherapy, patients could suffer from serious complications such as loss of organ function, bleeding, and infection [7, 8]. In addition, despite of universal usage for most cancer patients, surgery and radiotherapy are required to high capital costs and clinical outcomes are staff-intensive [9]. Thus, combined therapy with chemotherapy or immunotherapy has been considered as an alternative treatment options for effective cancer removal [10, 11]. Despite existence of many conventional cancer treatment options and improving survival rate of patients, complete cancer treatment is still unmet due to high recurrence rate on residual tumor, drug resistance, and severe complications after treatment [12]. Hence, the exploration

to improve therapeutic capabilities and reduce aggressiveness as well as complications is urgently required.

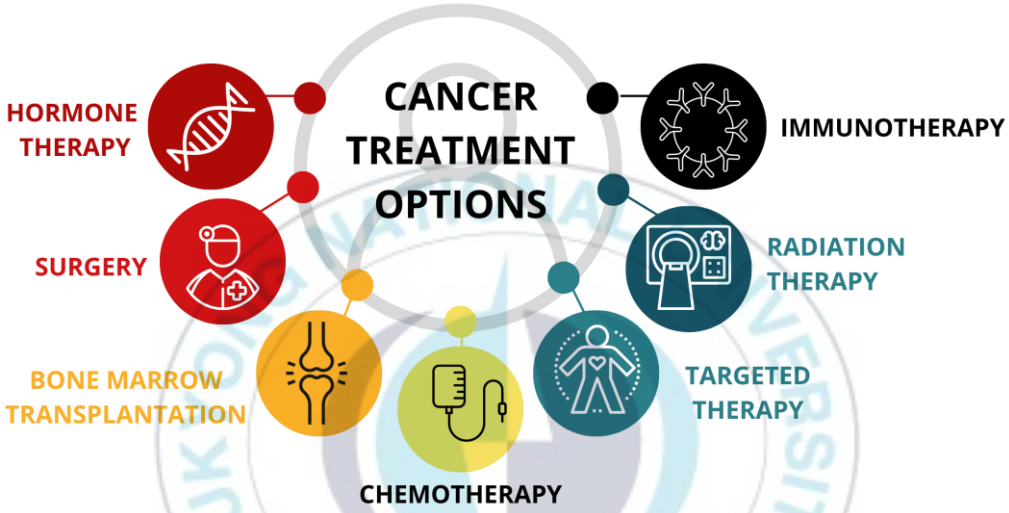

[Figure adopted from Ref. ["EBIS medial website"]

Figure 1. Conventional cancer treatment options

1.2. Photothermal therapy (PTT)

Photothermal therapy (PTT) has been widely investigated as a non- or minimally invasive therapeutic strategy, which uses photon energy to convert into heat for irreversible cancer cell damage [13] (Figure. 2). PTT mainly relies on triggering a photoabsorbing agents by an electromagnetic radiation such as radio frequency, microwaves, near-infrared or visible light, leading to release of vibrational energy [14]. Even though photodynamic therapy needs presence of oxygen to generate reactive oxygen species for antitumor effects, PTT does not require oxygen for targeted cell death [15, 16]. As PTT affects to cells by locally increasing temperature, PTT have attracted massive attention to clinicians [17].

According to operating temperature, PTT effects can be classified as shown in Figure. 3 [18]. Thermal treatment within 40-45 ℃ temperature range is called Hyperthermia treatment normally used in adjunctive therapy with other cancer treatments [19, 20]. Since protein denaturation starts over 39 ℃, aggregation and destruction of protein can be occurred after hyperthermia treatment [21, 22]. However, the efficacy of hyperthermia as a stand-alone modality is still far from being completely understood due to cellular self-repairing mechanisms, leading to cancer cell activation [23]. When operating temperature is over 50 ℃, the irreversible thermal damage is achieved in accordance with coagulative necrosis processes [24]. Although coagulative necrosis is highly efficient for tumor destruction, surrounding healthy tissue damage can also be accompanied due to poor selectivity. Above 60 ℃, collagen denaturation

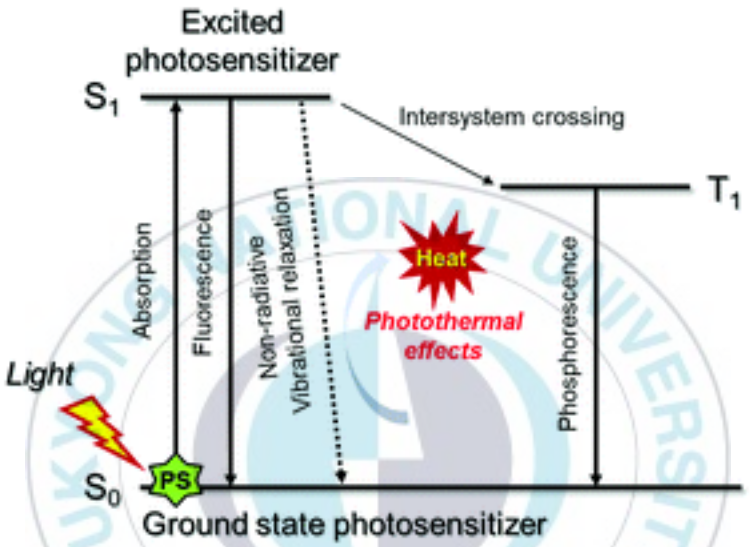

[Figure adopted from Ref. (Jung et al., "Organic molecule-based photothermal agents: an expanding photothermal therapy universe", Chemical Society Reviews, 47, 2280-2297, 2018)]

Figure 2. Underlying mechanism of photothermal therapy

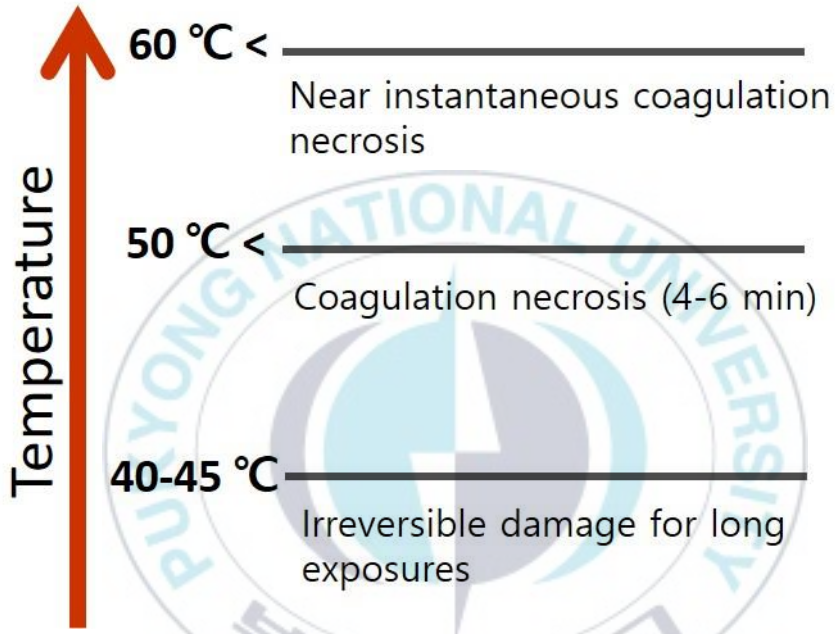

Figure 3. Classified diagram of different thermal effects on tissue by the corresponding operating temperature [18].

and tissue ablation are taking place, leading to severe damage in tissues [25].

As described earlier, photothermal-based treatment can induce nonspecific injury in the surrounding healthy tissue along the light path due to chromophores containing in tissues and nonuniform dispersity in the whole tumor [23]. Furthermore, PTT is facing limitations such as the shallow penetration depth in large volume of tumor [26]. Therefore, the development of novel therapeutic approaches is investigated to improve therapeutic efficacy with clinical safety assurance of PTT on tumor.

1.3 Strategies for enhanced photothermal therapy

Basically, to promote strong thermal effect on cancer, the role of the photoabsorbing is critical. With poor photoabsorbing agents, clinical outcomes are not sufficient due to undesired damage to healthy tissue and lack of heating for destroying tumor [26]. In the past decades, the enormous development of nanotechnology has provided for effective laser treatment on cancer. While many inorganic nanomaterials, Gold nanoparticles are attracting extensive attentions in various applications for drug delivery, photothermal effect, and contrast agents [27]. Especially, functionalized gold nanoparticles such as nanospheres, nanorods, and nanoshells (Figure. 4) have been demonstrated in PTT due to strong light absorption in the visible and near-infrared ranges [28, 29]. Nanosized graphene oxide has been also considered as a promising carbon-based photothermal agents owing to effective light-to-heat conversion and unique physical properties [30]. In addition, as organic molecules are advantageous such as easy chemical structure tuning and good biocompatibility, organic dyes have been also beneficial for tumor tissue diagnosis and PTT [31-33]. Despite numerous researches, the development of nanomaterials for complete cancer removal is still challengeable due to low photothermal conversion efficiency and systemic toxicity [34, 35].

Furthermore, maldistribution of laser density from optical fiber can be one of possible reason for poor clinical outcomes [36]. In fact, a bare-cut flat fiber is generally used to deliver laser light on tissue with Gaussian beam profile [37]. As tumor tissue

has three-dimensional irregular shape, uneven temperature distribution is often experienced, indicating insufficient temperature increase and deficient tumor removal. To prevent these potential complications, new approach of laser beam transmission is necessary as well.

Therefore, the aim of this dissertation is to enhance photothermal efficacy on cancer through development of photoabsorbing agents and irradiation methods. In chapter 2 and 3, novel photoabsorbing agents were presented and demonstrated for effective cancer treatment *in vitro* and *in vivo*. In chapter 4 and 5, multi-lens arrays (MLA)-assisted and power modulated PTT were evaluated with conventional photoabsorbing agents to explore feasibility of optical applications. Finally, laser stimulatory effects on cancer cells depending on various wavelengths were described to establish safety margin for clinical laser treatment in chapter 6.

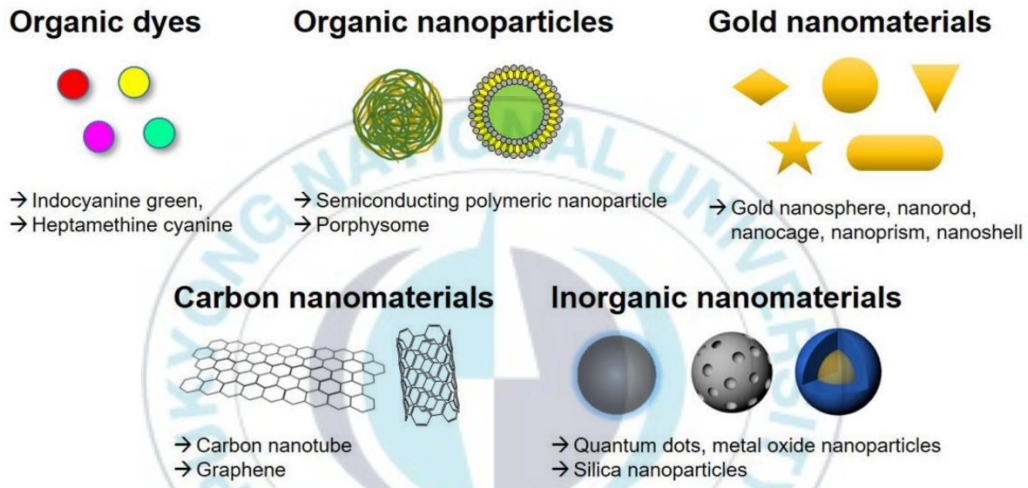

[Figure adopted from Ref. (Han et al., "Advances in Nanomaterial-Mediated Photothermal Cancer Therapies: Toward Clinical Applications", Biomedicines, 9(3), 305, 2021)]

Figure 4. Various types of photothermal agents

Chapter 2. Dual-chemo-photothermal treatment with Doxorubicin-fucoidan-gold nanoparticles

2.1. Introduction

Choroidal melanoma is the most common primary intra-ocular malignant tumor, and the incidence rate is approximately 6 per million in the United States [38]. The melanoma appears as a brown elevated dome-shaped tumor occurring in the sub-retinal space, and the malignant choroidal melanoma can metastasize to other parts of the body such as liver. Although the eye tumor is typically asymptomatic, the development of the choroidal melanoma can cause irregular astigmatism (blurred vision), retinal detachment along with decreased visual acuity, and even glaucoma with permanent vision loss. Over the last few decades, a great number of eye tumor treatments have been introduced, such as surgical incision, electromagnetic wave radiation, radiotherapy, hyperthermia, and photothermal treatment (PTT) [39-44]. However, the current treatments of the eye tumors still suffer from infection, invasive or ionizing natures, unpredictable thermal injury, and tumor recurrence [45]. Therefore, the alternative approach is still required to enhance the efficacy and safety of the eye tumor treatment even in a minimally invasive manner.

Nanomaterial-based PTT has extensively been investigated as a non-invasive or minimally invasive and effective therapeutic technique to treat various types of tumors *in vitro* and *in vivo* [46-50]. The primary purpose of this method is to employ light-absorbing agents and to locally generate heat upon light absorption, leading to

irreversible thermal injury selectively to the targeted tumors. The nanomaterials have attracted an increasing interest in the biomedical field due to their facile synthesis and unique physicochemical properties. In addition, various nano-agents to enhance PTT efficacy have widely been investigated such as copper sulfide and golden carbon-based materials [48, 51, 52]. Among the potential photothermally active nanomaterials, gold nanoparticles (AuNPs) have been studied extensively for drug delivery, cellular/tissue imaging, and thermal therapy on account of strong optical coupling, extraordinary photon-to-thermal energy conversion efficiency, and easy functionalization [27-29]. In addition, Fucoidan (Fu) has been investigated as a chemo-preventive substance for nanomedicine due to their antitumor and anti-inflammation effects that suppress the tumor growth as well as significantly reduce the inflammation periods [53, 54]. Fu has often been employed for coating AuNPs to reduce the toxicity of the metallic nanoparticles [55-57]. However, *in vivo* applications of the Fu-coated AuNPs have yet been explored in terms of surface functionalization and therapeutic effects particularly on the eye tumors. Recently, chemotherapy drugs have also been encapsulated or conjugated with AuNPs to enhance PTT efficacy and to minimize tumor recurrence [58]. Doxorubicin (Dox) is a common chemotherapeutic agent that is used to treat human malignancies by inhibiting nucleic acid synthesis [56, 58-60]. Several researchers have suggested the potential use of polymers as drug carriers to maximize the efficacy of Dox by limiting toxicity [61]. However, the current Dox chemotherapy still have the primary limitations including administration of large volume, resultant high toxicity on normal healthy cells, and a short lifetime in the body [62]. Therefore,

conjugation with hydrophilic polymers to overcome non-specificity and toxicity of Dox have been researched [63]. Moreover, as most nanomaterial-based PTT has been performed on the small-sized mice, further evaluations with larger animals are still required for clinical translation of the proposed technique. In fact, the large animals can be investigated effectively for the targeted therapy due to their larger tissue volume [64]. Therefore, to achieve synergistic cancer treatment with both thermal necrosis of PTT and chemotherapeutic effect by loaded Dox, gold nanoparticles were synthesized in the presence of Fu and were subsequently adsorbed by Dox. Due to anti-tumor and anti-inflammation effects as well as biocompatibility, Fu was selected to conjugate Dox with AuNPs by means of electrostatic physisorption interactions between positively charged groups (AuNPs and Dox) and negatively charged sulfate groups (Fu). The aim of the current study was to investigate the feasible application of Dox-conjugated Fu-encapsulated gold nanoparticles (Dox-Fu@AuNPs) in VX2 cells and xenograft tumors in mid-sized rabbits as an anti-cancer theranostic agent for effective eye tumor management (Figure. 5.).

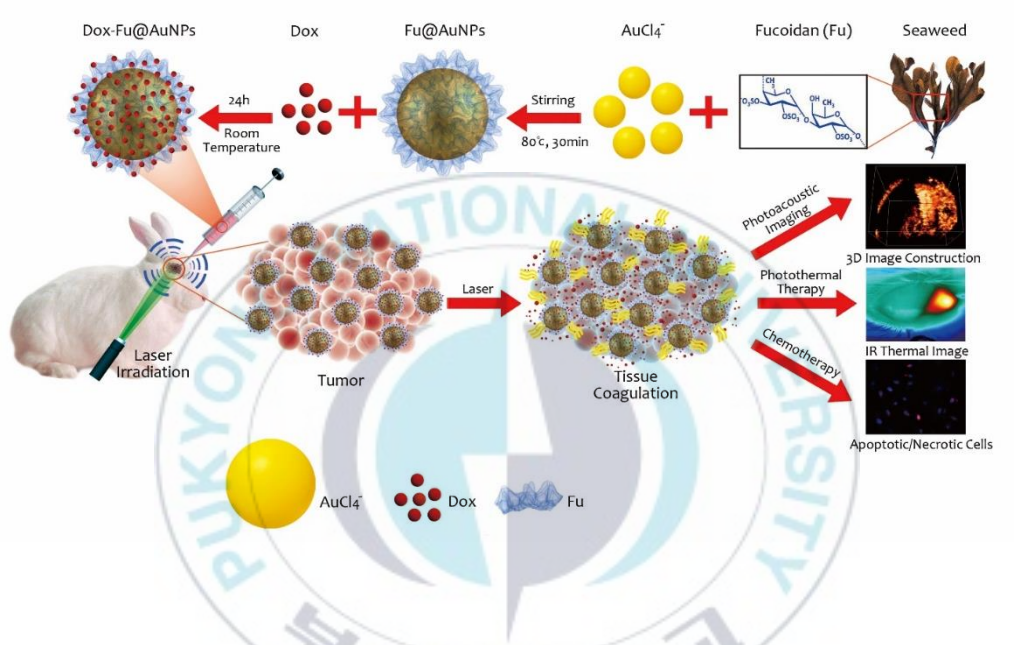

Figure 5. Description of Fu and Dox chemical structures and synthetic procedure for biocompatible Dox-Fu@AuNPs

2.2. Materials and methods

2.2.1 Chemical materials

Fu extracted from *Fucus vesiculosus* was obtained from Sigma (Sigma, St. Louis, Mo, U.S.A.). Chloroauric acid trihydrate ($HAuCl_4 \cdot 3H_2O$, > 99.9%) and doxorubicin hydrochloride (Dox·HCl) were purchased from Sigma-Aldrich Co. (St. Louis, MO, USA). Dulbecco's modified eagle's medium/F12 (DMEM-F12) was obtained from Cellgro (Mediatech, Massachusetts, USA). Dulbecco's modified eagle's medium (DMEM), trypsin–ethylenediaminetetraacetic acid (trypsin-EDTA), antibiotics, fetal bovine serum (FBS), and phosphate-buffered saline (PBS) were purchased from Gibco BRL, Life Technologies (Grand Island, NY, USA). 3-(4,5-Dimethyl-2-thiazolyl)-2,5-diphenyl-2H-tetrazolium bromide (MTT), dimethyl sulfoxide (DMSO), Hoechst 33342, and propidium iodide (PI) were obtained from Sigma-Aldrich. Double-distilled water was used for all aqueous solutions in the experiments. All chemicals were used directly as received without further purification.

2.2.2 Synthesis of Dox-Fu@AuNPs

0.005 g of Fu was poured into 10 ml $HAuCl_4 \cdot 3H_2O$ aqueous solution at a concentration of 1×10^{-4} M, and the solution was stirred at 80°C for 30 min on a magnetic hot plate. The synthesized AuNPs were isolated by centrifuging the mixed solution at 13,000 rpm for 30 min. Then, several cycles of washing with deionized water and centrifuging were performed to remove excess fucoidan and unreacted particles for the further

experiments. Filtration was performed for 24 h through a dialysis tube with a 12,000 Da molecular weight cutoff to remove ionic impurities. Dox-Fu@AuNPs were prepared by adding Dox·HCl to the solution containing the fucoidan-coated AuNPs. The final concentration of Dox was adjusted to 10^{-4} M in a solution. The resulting mixture was stirred for 2 min to obtain a homogeneous distribution of AuNPs and then incubated for 24 h at room temperature. The resulting solution was centrifuged at 10,000 rpm for 15 min to remove excess non-reacted compounds. The acquired pellet after centrifugation was distinguished from the supernatant solution and re-dispersed in deionized water prior to the further characterization [56].

2.2.3 Characterization of Dox-Fu@AuNPs

To select the excitation wavelength for PTT, the absorbance of Dox-Fu@AuNPs was measured from 300 to 1100 nm by using a spectrometer (XS2, BioTek, Winooski, VT, USA). High-resolution transmission electron microscopy (HR-TEM) (JEM 2010, JEOL Ltd, Tokyo, Japan) was used to visualize the fabricated nanoparticles. The HR-TEM images provided the estimated size and morphology of the nanoparticles. The median size of the nanoparticles was then calculated with Image J (National Institute of the Health, Bethesda, MD, USA). For comparison, the particle size was analyzed again with dynamic light scattering (DLS) by using an electrophoretic light scattering spectrophotometer (ELS-8000, OTSUKA Electronics Co. Ltd., Japan) at a fixed angle of 90° and room temperature. Zeta potential (ZP) values of Dox-Fu@AuNPs were measured by utilizing an electrophoretic light scattering spectrophotometer (ELS-8000,

OTSUKA Electronics Co. Ltd., Japan).

The elemental analysis of the synthesized Dox-Fu@AuNPs was evaluated by using energy dispersive x-ray spectroscopy (EDS; Hitachi, S-2400, Japan/Kevex Ltd, Sigma). The surface elemental compositions and impurities of Dox-Fu@AuNPs were identified by using EDS analysis in a specific scan area on the SEM sample at 20 keV. The crystalline structure of the powdered nanoparticles was analyzed by using an X-ray power diffraction (XRD) machine (X'Pert-MPD System, Philips, Almelo, Netherlands). The chemical functional groups of the nanoparticles were determined by using Fourier-transform infrared spectroscopy (FT-IR) spectrometer (FT/IR 6100, Jasco, Easton, Pennsylvania, USA) in a diffuse reflectance mode. The contents of the nanoparticles (i.e., organic and inorganic elements) were characterized by performing thermogravimetric analysis (TGA) (TGA7, Pyris 1, Perkin Elmer, Waltham, Massachusetts, USA). The TGA analysis of the nanoparticles was determined by the nanoparticles placed in an alumina pan under the nitrogen atmosphere and heated from room temperature to 700℃ at a ramping time of 10℃/min.

2.2.4. Light Source for Dox-Fu@AuNPs

For laser irradiation, a quasi-cw Q-switched 532-nm laser system (GreenLight PV®, American Medical Systems, Inc., San Jose, USA) was employed at various irradiances (i.e., 0.06, 0.08, 0.09, and 0.11 W/cm^2) and times (i.e., 2, 3, and 5 min). A multimode 600-μm optical fiber (NA = 0.22) was used to deliver the laser light into each sample.

The spot size was estimated to be 10.2 mm^2. To assess photothermal effects of the synthesized Dox-Fu@AuNPs, four different concentrations of Dox-Fu@AuNPs in solution [0 (saline), 100, 200, and 300 μg/ml] were initially tested with the laser irradiation. The samples were poured in the wells of a sterile 96-well plate (total volume of 100 μl per each well). An infrared thermal camera (FLIR A300, FLIR System, Inc., Sweden) was used to monitor spatio-temporal development of temperature in the aqueous solution during the laser exposure.

2.2.5. *In vitro* chemo-photothermal therapy

To measure cell viability of Dox-Fu@AuNPs without laser irradiation, VX2 cells and Raw 264.7 cells were seeded into a 96-well culture plate at a density of 2×10^4 cells/well and 5×10^4 cells/well in a 100 μl of culture medium, respectively. The seeded cells were then washed with PBS and incubated with the Dox-Fu@AuNP solution at various concentrations (0, 20, 40, 60, 80, 100, 200, 300 μg/ml) for 24 or 48 h at 37˚C in the humidified atmosphere of 5% CO_2. The cells without Dox-Fu@AuNPs were used as a control. After various incubation times, MTT tetrazolium bromide solution (1 mg/ml) was added to each well. The cells were incubated for 4 h, and DMSO was replaced to dissolve formazan crystal. The optical density was quantified at 570 nm by using an ELISA micro plate reader (SpectraMax, 340, Molecular Device, Sunnyvale, CA, USA). The relative cell viability was calculated and compared with that of a non-treated blank group. To evaluate chemo-photothermal therapy on the cells, VX2 cells were seeded in to 96-well culture plate at a density of 2×10^4 cells/well. The seeded cells were

incubated with a 200 µg/ ml concentration of Dox-Fu@AuNPs for 4 h at 37˚C. The treated cells were then washed with PBS and fresh media was replaced. The cultured cells were then placed in a water bath maintained at 37°C prior to laser treatment. Laser light at an irradiance of 0.11 W/cm^2 was used to illuminate the samples for 2 min. To assess cell death, MTT assay was performed after 24 h incubation.

2.2.6. Hoechst 33342 and PI staining

VX2 cells were cultured in 6-well plates at 2×10^5 cells/well and incubated for 24 h at 37˚C in the humidified atmosphere of 5% CO_2. The cells were then treated with Dox-Fu@AuNP solution at the final concentration of 200 µg/ml and further incubated for 4 h. The cultured cell plates were washed three times with PBS to remove unattached nanoparticles before double-staining with Hoechst 33342 and PI fluorescent dyes. After washing, 300 µl of 10 µg/ml Hoechst solution was added to the cells and incubated for another 20 min at 37˚C in the dark environment. The cells were then washed twice with PBS, and 300 µl PI (10 µg/ml) was added. The sample was incubated for an additional 10 min at 37˚C. Finally, the stained cells were washed three times and observed with a Leica fluorescence microscope equipped with a DFC450C color digital camera (Leica, Wetzlar, Germany).

2.2.7. *In vivo* PTT with Dox-Fu@AuNPs

24 New Zealand White rabbits (3-4 months old and 2.2-2.6 kg) were used for *in vivo* PTT testing and purchased from Taesung Laboratory Animal Science (Busan, Korea).

VX2 tumor cells were used for tumor inoculation into eyes of each animal. The cultured VX2 cells were collected by using a centrifuge at 750 rpm for 5 min. A suspension was prepared of 1.0×10^7 tumor cells in 500 µl HBSS (Hank's balanced salt solution, Gibco® Thermo Fisher Scientific). To create tumors in the eyes of the rabbits, each rabbit was intramuscularly anesthetized with 10 mg/kg ketamine and 3 mg/kg xylazine and secured in a supine position, and their conjunctival areas were exposed under visual guidance. Using a 27-gauge needle, 0.4 ml of a suspension of VX2 cells (1×10^7) was injected into the subconjunctival space directly over the pars plana. When the tumor grew to a volume of approximately 100 mm^3, the tumor-bearing rabbit eyes were randomly divided into the following four experimental groups: (1) control group injected with saline and without laser application (N = 5), (2) treatment with laser only (2 min; N = 6), (3) intratumoral injection of 100 µl Dox-Fu@AuNPs dispersed in saline at 200 µg/ml (N = 5) without laser irradiation, and (4) injection of Dox-Fu@AuNPs (100 µl, 200 µg/ml) and laser irradiation (2 min; N = 8). All rabbit studies satisfied the guidelines of the Korean National Institutes of Health (KNIH) on the care and use of laboratory animals. The experimental procedures were approved by the Committee on Animal Research of the College of Medicine at Kosin University (Permit number: KMAP-16-24).

For *in vivo* testing, all the rabbits were anesthetized with an intramuscular injection of ketamine (35 mg/kg) and xylazine (5 mg/kg) prior to Dox-Fu@AuNP intratumoral injection. Twenty minutes after the injection, the rabbit models with and without the injected nanoparticles were illuminated with a 532-nm laser system at 0.11

W/cm^2 (irradiation time of 2 min and beam size of 10.2 mm^2). An IR thermal camera was employed to real-time monitor temperature development of the tissue during the laser irradiation. Only a single treatment was given to all the animals. The growth of tumors was examined by a caliper every day for 14 days after the treatments. The tumor volume was calculated by using the formula of $v = (l \times w^2)/2$, where *v, l,* and *w* represent the tumor volume (mm^3), tumor length (mm), and tumor width (mm), respectively [29].

To identify tumor margins before treatment, a custom-made photoacoustic imaging (PAI) system was used on the tumor-bearing eyes *in vivo*. A detailed description of the system was reported in previous study [65]. To maintain anesthesia during the *in vivo* experiments, anesthetic (i.e., ketamine = 17.5 mg/kg/h and xylazine = 2.5 mg/kg/h) was injected at an interval of 30 min to the animals. Prior to the experiments, the temperature of each rabbit was maintained by using an electric heating pad. After the anesthesia, the rabbits were positioned on the sample stage, and the areas of interest were fixed with transparent tape to stabilize and to minimize any breathing or other motion artifacts. A water bath with an open bottom wrapped with plastic film was placed on the top of the eye tumor. The ultrasound gel was sandwiched between the water bath and the tumor region. An ultrasound transducer was mounted in the water bath, allowing it to move freely in 3D while not applying any physical pressure on the rabbit. Then, the targeted regions were photoacoustically imaged. After acquiring the control PA image, Dox-Fu@AuNPs (0.1 ml and 200 μg/ml) were intratumorally injected into the tumors with a syringe. Twenty minutes after the injection, PAI of the injected tumor was performed. After the *in vivo* experiments, each rabbit was

immediately returned to its kennel. To distinguish the position between the normal tissue and the tumor tissue, image segmentation was performed as post-image processing using Matlab software (MathWorks, Massachusetts, USA)

2.2.8. Histological analysis

To evaluate *in vivo* treatment efficacy of Dox-Fu@AuNPs, all rabbits with eye tumors were euthanized with overdose with CO_2 gas 14 days after the testing. The eye tumor tissues were removed aseptically for histological examination. The acquired samples were fixed in 10% neutral buffered formalin (VWR, Radnor, PA) for two days. The fixed tissues were cross-sectionally cut in 3 mm sections and embedded in paraffin. Then, the paraffin-embedded tissues were sliced to a thickness of 4 μm and stained with hematoxylin and eosin (H&E). Each slide was evaluated by using an Olympus BX51 light microscope (Olympus Corp., Tokyo, Japan).

2.2.9. Statistical analysis

All experiments were executed and repeated three times, and data were expressed as mean ± standard deviation (SD). For non-parametric statistical analysis, Mann-Whitney U test in conjunction with SPSS (Ver 22, IBM Corporation, Armonk, New York) was used, and $p < 0.05$ was considered statistically significant.

2.3. Results

2.3.1. Characterization of Dox-Fu@AuNPs

For effective chemo-photothermal therapy of eye tumor, Dox-Fu@AuNPs were characterized in Figure 6. High-resolution TEM (HRTEM) images in Figure 6(a) demonstrate that Dox-Fu@AuNPs had spherical shape with a size of 101.5 ± 23.2 nm. AuNPs encapsulated by Fu was successfully coated with Dox, which is indicated by white dotted arrows [Figure 6(b)]. The average particle size of Dox-Fu@AuNPs was 116.7 ± 40.6 nm [Figure 6(c)] whereas the average sizes of both AuNPs and Fu@AuNPs were 15 nm [66] and 82 ± 11.5 nm [54]. Table 1 summarizes the measure particle sizes. Zeta Potential value of Dox-Fu@AuNPs in an aqueous solution was measured to be −46.2 mV, indicating that the surface of AuNPs was mainly coated with negatively charged groups and also responsible for the moderate stability of the nanoparticles in the aqueous solution. XRD patterns of Dox, Fu, and Dox-Fu@AuNPs confirm the crystal structures of the synthesized nanoparticles [Figure 6(d)]. The Dox-Fu@AuNPs sample exhibited the distinctive peaks at 2θ values of 38.6o, 44.5o, 64.7o, and 77.6o, which corresponded to the (111), (200), (220), and (311) reflection of the crystalline metallic of AuNPs (JCPDS 04-0784). The FT-IR spectra exhibit the characteristic peaks of different functional groups at various positions shown in Figure 6(e). Overall, the spectra of Dox, Fu and Dox-Fu@AuNPs samples displayed strong broadband of O-H stretching of alcohols groups bound to the AuNPs at 3320, 3420, and 3332 cm-1, respectively. The peak around 2900 cm-1 is attributed to the C-H

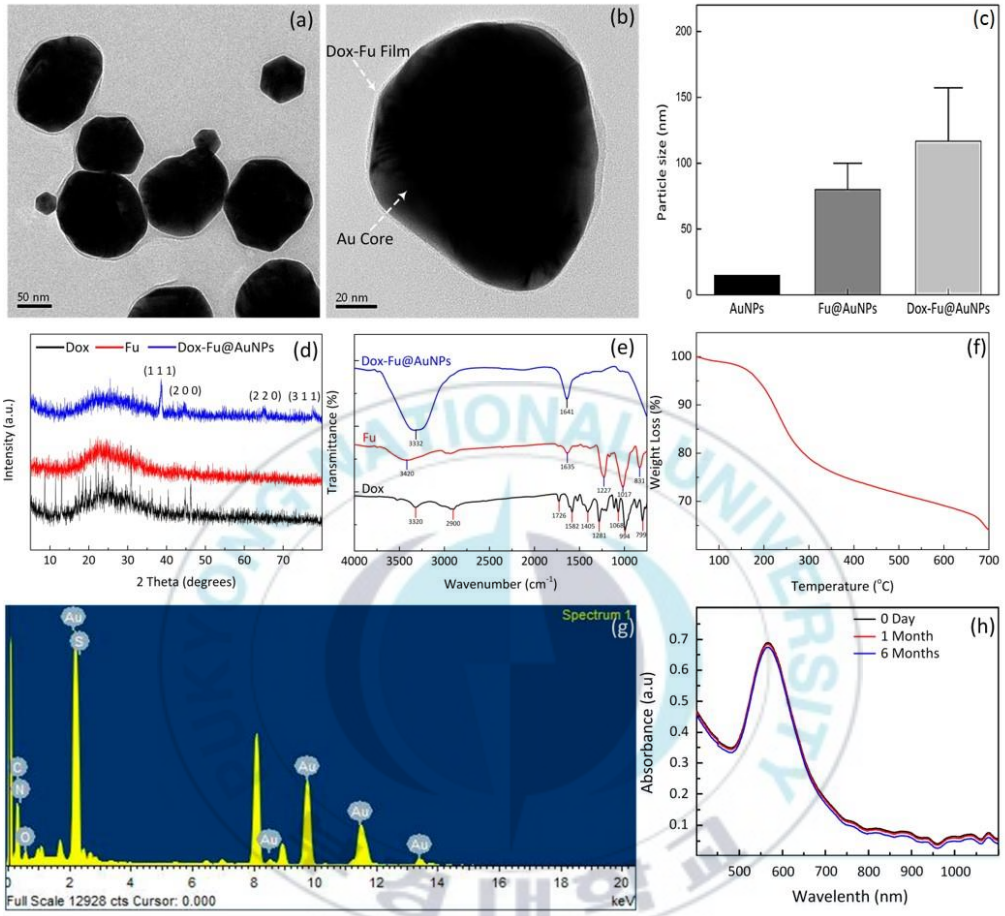

Figure 6. Charaterization of synthesized Dox-Fu@AuNPs. TEM images of (a) Dox-Fu@AuNPs and (b) Dox-Fu@AuNPs surrounded with grey shell representing Fu-coated Dox, (c) comparison of AuNPs [66], Fu@AuNPs [56], and Dox-Fu@AuNPs estimated by DLS, (d) and (e) XRD patterns and FT-IR spectra of Dox, Fu, and Dox-Fu@AuNPs, respectively, (f) TGA curve of Dox-Fu@AuNPs, (g) EDS analysis of Dox-Fu@AuNPs, and (h) absorption spectra of Dox-Fu@AuNPs as function of wavelength at various times (0 day, 1 day, and 6 months)

Sample name	Modification	PD* by TEM	HD** by DLS
Dox-Fu@AuNPs	-Fucoidan	101.5 ± 23.2	116.7 ± 40.6
Dox-Fu	-	5.7 ± 1.3	-

Table 1. Particle diameter (*PD: particle diameter; **HD: hydrodynamic size of Dox-Fu@AuNPs)

stretching of alkanes. The band at 1726 cm-1 exhibits the stretch of the saturated ester C=O groups. The two peaks at 1641 and 1635 cm-1 correspond to the stretching vibration from the primary amines. The bands at 1582 cm-1 are assigned to aromatic C-C ring stretching groups. The characteristic peak at 1405 cm-1 can be assigned to the bending of –COO- group. The bands at 1227 and 1281 cm-1 correspond to the C-H wag alkyl halides. The peaks around 1017 and 1068 cm-1 correspond to the C-N stretching of aliphatic amines. The TGA curve shows a significant weight loss of the sample as a function of temperature in Figure 6(f). The weight loss was initiated at the temperature of 100 ˚C, which corresponded to the removal of residual moisture in the sample. In addition, the weight showed a slight decrease (about 1.7 %) but induced a sudden weight loss at the temperature between 135 to 300 ˚C due to decomposition of Fu [67]. Then, the gradual weight decrease indicates that the organic compounds from Dox and Fu surrounding Dox-Fu@AuNPs were completely degraded at the higher temperatures. As a result of the temperature increase to 700 ˚C, the percentage of the total weight loss of the coating layer for Dox-Fu@AuNPs was measured to be approximately 35%. Thus, the residual weight of the corresponding AuNPs was 65%. The EDS spectra confirm the presence of Au as the main element signal in Dox-Fu@AuNPs [Figure 6(g) and Table 2]. The fabricated nanoparticles were composed of 88.8 % Au, 9.4 % C, 0.4 % N, 0.2 % O, and 0.3 % S by weight. Absorption spectra of Dox-Fu@AuNPs at various times (0-day, 1 month, and 6 months) demonstrate strong light absorption at 532nm and absorbance stability regardless of the time [Figure 6(h)], which means heat generation can be occurred effectively at 532 nm wavelength. Thus,

Element	EDS	
	Weight (%)	Atomic (%)
Au	88.77	33.57
C	9.36	58.06
N	0.42	2.24
O	1.18	5.50
S	0.27	0.63

Table 2. Atoms analysis of Dox-Fu@AuNPs measure by EDS

it was confirmed that the fabricated Dox-Fu@AuNPs can be applicable for PTT and PAI. Characterization of the other control particles (i.e., Fu@AuNPs) has been reported in our previous study [56].

2.3.2. Photothermal effects of Dox-Fu@AuNPs

Thermal responses of Dox-Fu@AuNPs during 532-nm laser irradiation for 5 min were evaluated in terms of temporal development of temperature [Figure 7(a)] and peak temperature [Figure 7(b)]. The temporal elevation of the temperature during the irradiation [0.11 W/cm^2; Figure 7(a)] demonstrated that regardless of the concentration, the temperature in the Dox-Fu@AuNPs aqueous solution began to increase rapidly, but after 1 min, the temperature became almost saturated. The corresponding steady-state temperatures were 48.6 ± 3.0, 56.8 ± 1.6, and 64.6 ± 1.7 °C for 100, 200, and 300 μg/ml, respectively. Thomsen et al. reported that the temperature of approximately 55~70 °C could lead to irreversible damage to tumor cells [68]. The peak temperature almost linearly increased with laser intensity and concentration of Dox-Fu@AuNPs. Control (saline) shows no considerable changes in the temperature during the irradiation. At the lowest irradiance (0.06 W/cm^2), the temperature increased from 40.7 ± 1.5 °C with 100 μg/ml Dox-Fu@AuNPs (thermal gradient = 0.04 °C/s) to 48.7 ± 2.0 °C with 300 μg/ml Dox-Fu@AuNPs (0.07 °C/s). At the highest laser irradiance (0.11 W/cm^2), the peak temperature significantly increased from 48.6 ± 3.0 °C with 100 μg/ml Dox-Fu@AuNPs (0.07 °C/s) to 64.6 ± 1.7 °C with 300 μg/ml Dox-Fu@AuNPs (0.12 °C/s). The maximum temperature increases were estimated to be 16.0, 24.1, and 29.1 °C for

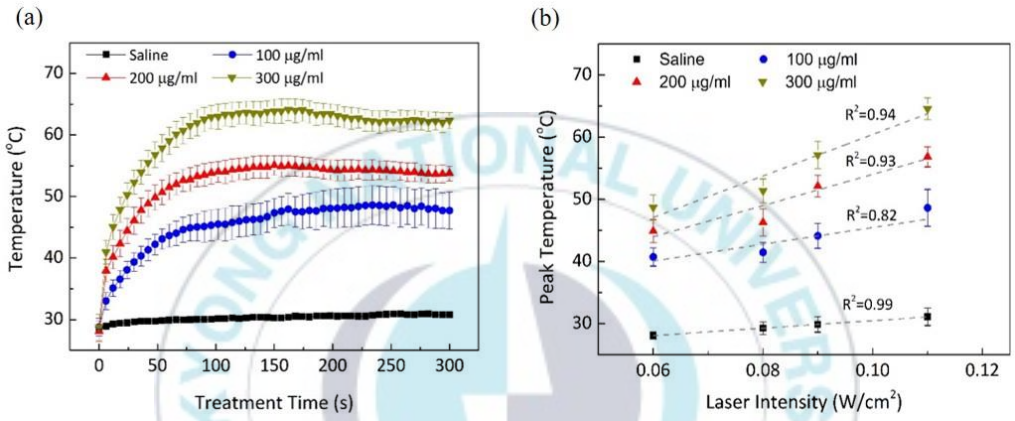

Figure 7. Photothermal effects of Dox-Fu@AuNPs. (a) Temporal development of Dox-Fu@AuNPs in 1 ml of saline was monitored during laser exposure at 0.11 W/cm^2 for 5 min. (b) The peak temperatures from saline and Dox-Fu@AuNPs in aqueous solution at various concentrations (0 from saline, 100, 200, and 300 μg/ ml) after 5-min laser irradiation was compared as a function of laser intensity.

Dox-Fu@AuNPs samples at 100, 200, and 300 μg/ml, respectively (initial temperature = 28.1 °C). Thus, due to the steady-state temperature higher than 65 °C, both 200 μg/ml of Dox-Fu@AuNPs and 2-min irradiation (at 0.11 W/cm^2) could be appropriate conditions to induce the irreversible thermal damage to cancer cells.

2.3.3. *In vitro* cytotoxicity effect of Dox-Fu@AuNPs

VX2 squamous carcinoma cells and Raw 264.7 cells were tested to investigate anti-tumor effect of Dox-Fu@AuNPs in vitro as a function of concentration at two different incubation times [Figures 8(a) and 9]. Regardless of incubation time, control (no particles) demonstrated no changes in the cell viability. The viability of the VX2 cells rapidly decreased with the increasing concentrations of Dox-Fu@AuNPs. However, above the concentration of 200 μg/ml, the cell viability became saturated (24h; cell viability of 100 μg/ml: 49.3±4.6%, 200 μg/ml: 42.1±11%, 300 μg/ml: 39.1±19.2%). In spite of the comparable trend [Figure 8(a)], the longer incubation time (48 h) further decreased the cell viability by up to 39% (at 300 μg/ml), in comparison with 24 h.

2.3.4. *In vitro* chemo-photothermal therapy with Dox-Fu@AuNPs

Cell viability was evaluated to assess effect of various conditions on VX2 tumor cells [Figure 8(b)]: control, laser only, Fu@AuNPs only, Dox-Fu@AuNPs only, laser with Fu@AuNPs, and laser with Dox-Fu@AuNPs (concentration = 200 μg/ml, irradiance = 0.11 W/cm^2, and irradiation time = 2 min). Both control and laser only exhibited almost

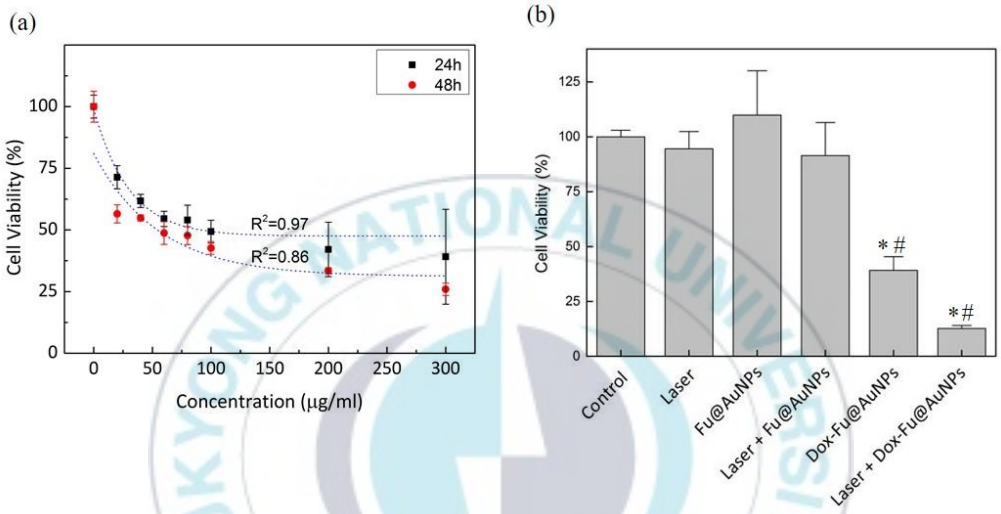

Figure 8. Photothermal and cytotoxicity effects against VX2 cells with Dox-Fu@AuNPs. (a) The cell viability of Dox-Fu@AuNPs in VX2 at various concentrations (0, 20, 40, 60, 80, 100, 200, and 300 μg/ml) with different incubation times (24 and 48 h) was measured by using MTT assay. (b) VX2 cell viability under various treatment conditions (control, laser, Fu@AuNPs, Dox-Fu@AuNPs, Fu@AuNPs-assisted laser irradiation, and 200-μg/ml Dox-Fu@AuNPs-assisted laser irradiation for 2 min) was analyzed by using MTT assay (* and #: $p < 0.05$ compared with control and laser group, respectively).

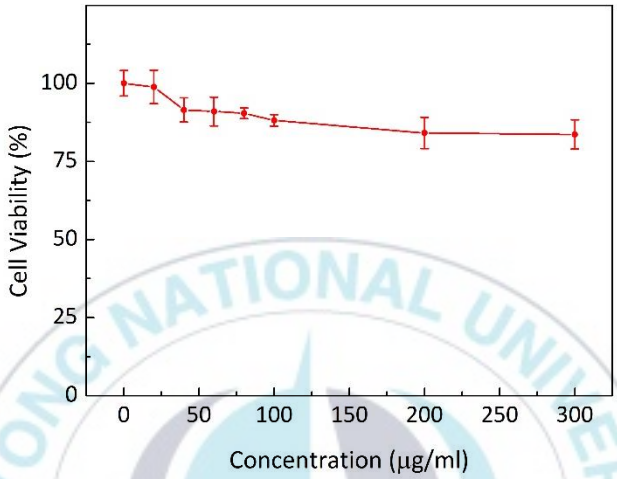

Figure 9. Effect on Dox-Fu@AuNPs on Raw 264.7 macrophages at various concentration for 24 h.

insignificant effects (≥ 90%). In addition, Fu@AuNPs also had no significant thermal damage on the VX2 cells. Fu@AuNPs with laser irradiation hardly promoted cell death possibly due to less significant temperature increase (up to 41 ˚C) in the cells. However, the addition of Dox-Fu@AuNPs noticeably decreased the cell viability. Moreover, Dox-Fu@AuNPs under laser irradiation resulted in the maximal cellular death of 88%, which is up to 7-fold higher than those of the other conditions.

The treated VX2 cells were stained with Hoechst 33342 and PI and observed with a fluorescence microscope to evaluate the anti-tumor effect of Dox-Fu@AuNPs-assisted PTT (concentration = 200 μg/ml, irradiance = 0.11 W/cm^2, and irradiation time = 2 min) on tumor cells (Figure 10). Blue emission is from the Hoechst dye that stains the nuclei of viable VX2 cells, and red emission from PI staining indicates dead cells. Both control [Figure 10(a)] and laser only [Figure 10(b)] displayed clear blue emissions from the nuclei along with minimal red emissions, indicating that cells were viable due to insignificant cytotoxicity. The treated cells with Dox-Fu@AuNPs (no irradiation) exhibited a slight increase in the red fluorescence, thus representing a slight increase in the dead cells [Figure 10(c)]. In contrast, the VX2 cells treated with Dox-Fu@AuNPs and laser irradiation yielded a marked increase in the cellular death. The fluorescence images of the treated VX2 cells were also taken at various positions: the following positions: (a) outside, (b) inside (center), and (c) at the border of irradiation zone (Figure 11). The cells located outside the laser beam showed good viability [Figure 11(a)] whereas most of the cells in the area of laser exposure were dead [Figure 11(b)]. Figure 11(c) clearly exhibits a mixture of the treated and the non-treated regions at the

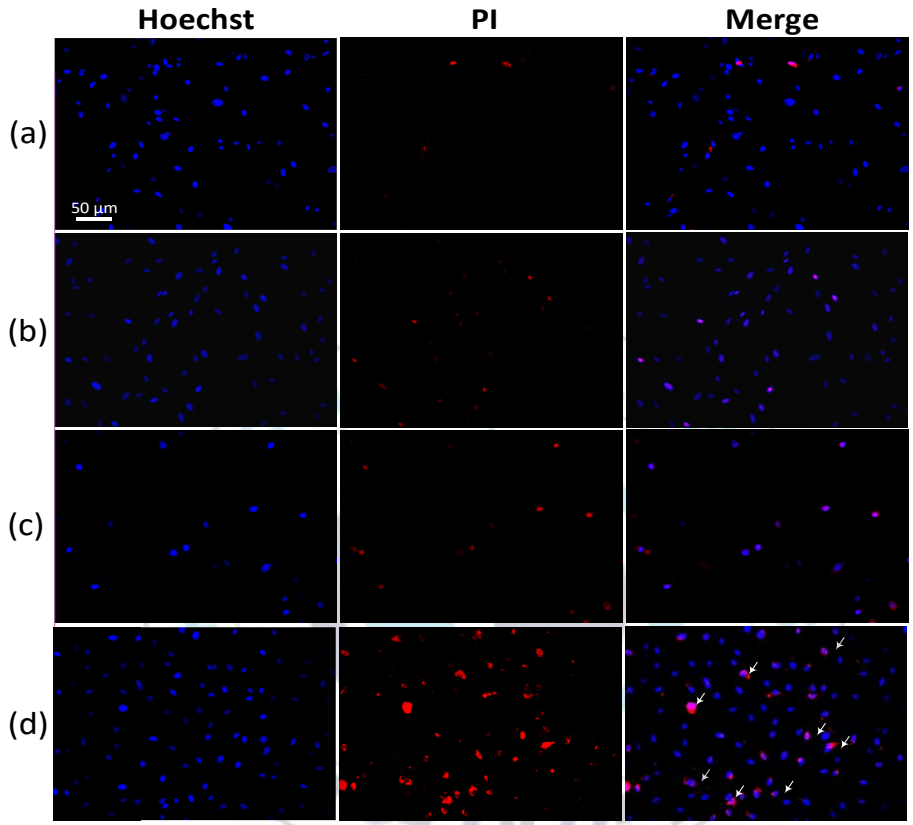

Figure 10. Double staining with Hoechst 33342 and PI on VX2 cells: (a) control, (b) cells irradiated with laser only (0.11 W/cm^2), (c) cells treated with Dox-Fu@AuNPs at 200 μg/ml, and (d) cell treated with Dox-Fu@AuNPs at 200 μg/ml followed by laser irradiation (0.11 W/cm^2 for 2 min). Nuclei were stained with Hoechst 33342 (blue). The dead cells were represented by red staining with PI (20x; bar = 50 μm).

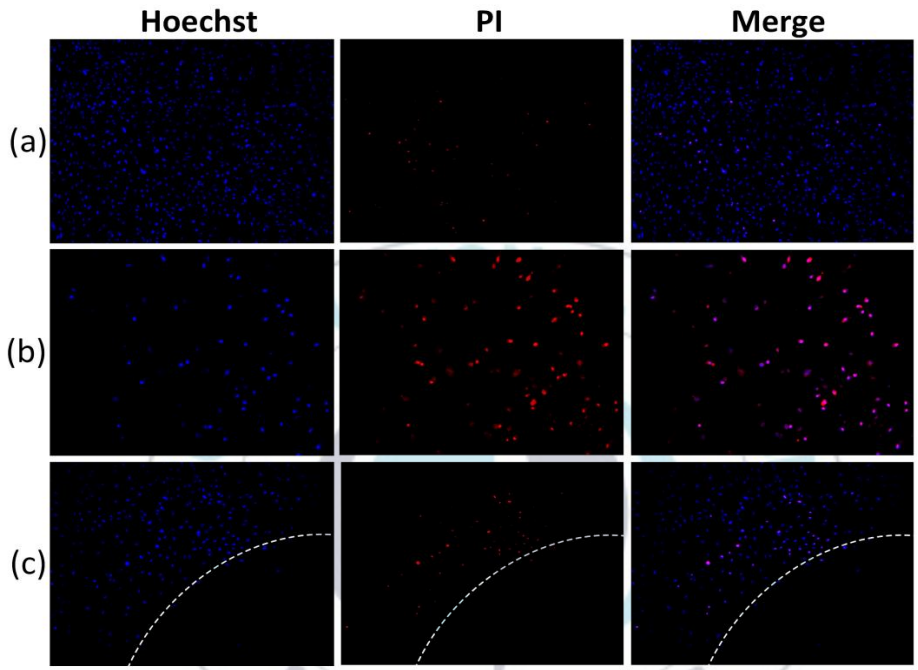

Figure 11. Fluorescence microscope images of VX2 cells stained with Hoechst and PI after laser irradiation at different positions and staining. The fluorescence and bright field images of the cells were located: (a) outside, (b) inside, and (c) on the edge near the treated field (20x; bar = 50 μm) border, implicating selective antitumor effects as a result of dual-chemo- and photothermal treatments.

border, implicating selective antitumor effects as a result of dual-chemo-and photothermal treatment.

2.3.5. *In vivo* testing

Dual-treatment efficacy of Dox-Fu@AuNPs was assessed with VX2 tumor-bearing rabbits (Figure 12). Figure 12(a) presents a series of IR thermal images of the tumor region at various times for two groups: laser only (left column) and laser with Dox-Fu@AuNPs (right column). During the laser irradiation, all the groups exhibited a temperature increase in terms of color variations. The thermal lesion had a round shape with a diameter of approximately 10 mm, which was large enough to cover the entire tumor for hyperthermia. Apparently, the laser with Dox-Fu@AuNPs group yielded a 32% higher increase than the laser only group did (i.e., 56.7 °C for laser only vs. 75.0 °C for laser with Dox-Fu@AuNPs for 2-min irradiation). Temporal elevation of the temperature in the tumors was also monitored in Fig. 12(c). Overall, both the groups demonstrated that the tumor temperature increased with the irradiation time but became almost saturated around 30 s after the onset of the irradiation. After 2-min irradiation, the laser with Dox-Fu@AuNPs group entailed the temperature of 75.0 ± 2.9 °C, which is 30% higher than that of the laser only (56.7 ± 2.3 °C; $p < 0.001$). It was noted that the induced temperature due strong light absorption was high enough to cause the irreversible thermal damage to the tumors.

The size of each tumor after various treatments was monitored for 14 days to

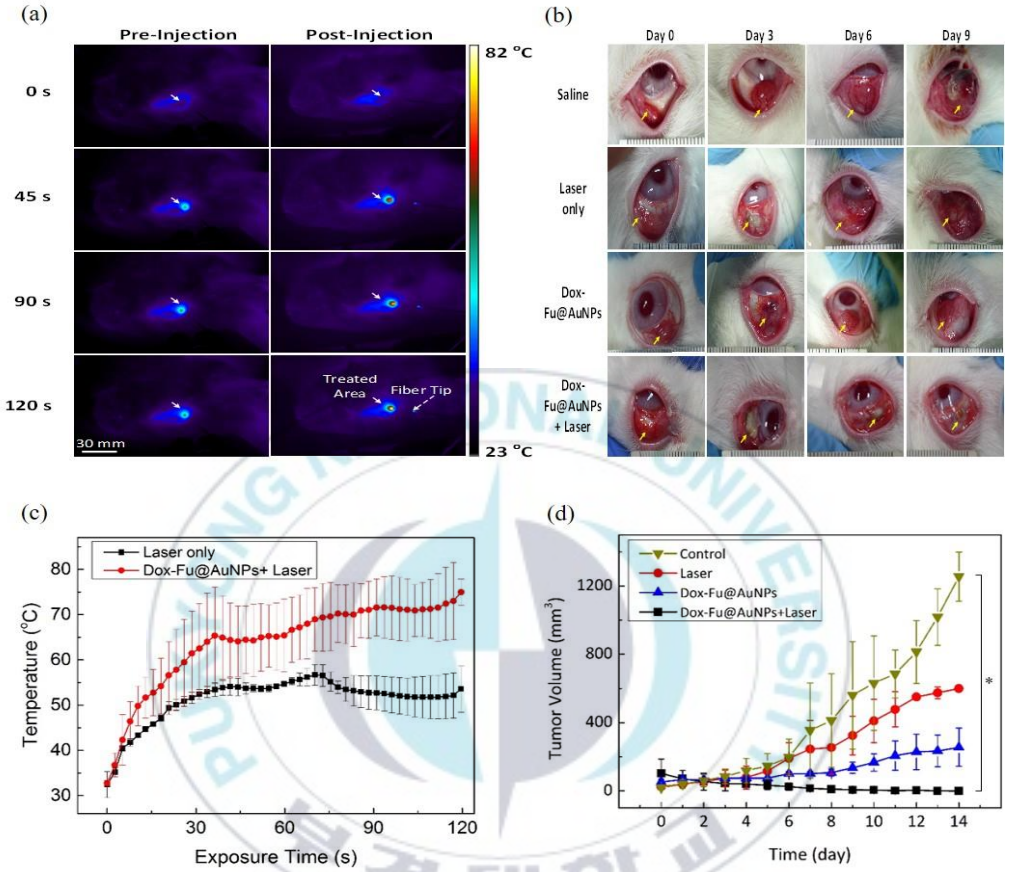

Figure 12. Chemo-photothermal effects of Dox-Fu@AuNPs in rabbit eye tumor model. (a) *In vivo* infrared thermographic maps of eye tumors before and after injection with Dox-Fu@AuNPs were shown at various times after laser irradiation. (b) Representative photographs of the rabbit eye tumors under various conditions (saline as control, laser only, Dox-Fu@AuNPs only, and Dox-Fu@AuNPs with laser irradiation) were shown. (c) The graph indicates temporal development of temperature from the irradiated area in the tumor during the laser irradiation (laser only vs. Dox-Fu@AuNPs with laser irradiation: N = 20). (d) Tumor volume was estimated three times per day over a period of 14 days after each treatment. (*$p < 0.05$ compared with control).

evaluate the dual-treatment efficacy of Dox-Fu@AuNPs: control (saline), laser only, Dox-Fu@AuNPs only, and laser with Dox-Fu@AuNPs as shown in Figure 12(b). Yellow arrows indicate the position of the tumor before and after the treatments. The sizes of the tumor for control, laser only, and Dox-Fu@AuNPs only increased slowly for 6 days after the treatment and then gradually increased. In contrast, the tumor size for laser with Dox-Fu@AuNPs significantly decreased over time [Figure 12(b)], and the tumor began to disappear at day 9. Tumor volume was also quantified for 14 days to compare therapeutic effects of various conditions [Figure 12(b)]. The tumor sizes slightly increased from approximately 100 mm^3 to approximately 112 mm^3 over 5 days and then rapidly increased to approximately 1255, 600, and 256 mm^3 at day 14 for control, laser only, and Dox-Fu@AuNPs only, respectively. Conversely, the laser with Dox-Fu@AuNPs group demonstrated a significant decrease in tumor growth, and the tumor was completely eradicated within 6 days after the treatment. No tumor recurrence was also observed at day 14.

The feasible application of Dox-Fu@AuNPs as a PA contrast agent was examined in *in vivo* VX2 tumor-bearing rabbit models before and after a single injection of 100 µl Dox-Fu@AuNPs at 200 µg/µl (Figure 13(a)). White dashed rectangles represent the scanned areas whereas white dotted arrows indicate the position of the tumor. The tumor injected with Dox-Fu@AuNPs created higher PA signals, compared with the pre-injection that showed an unclear image due to the lack of intrinsic chromophores at 532 nm. The position of the tumor after the injection was

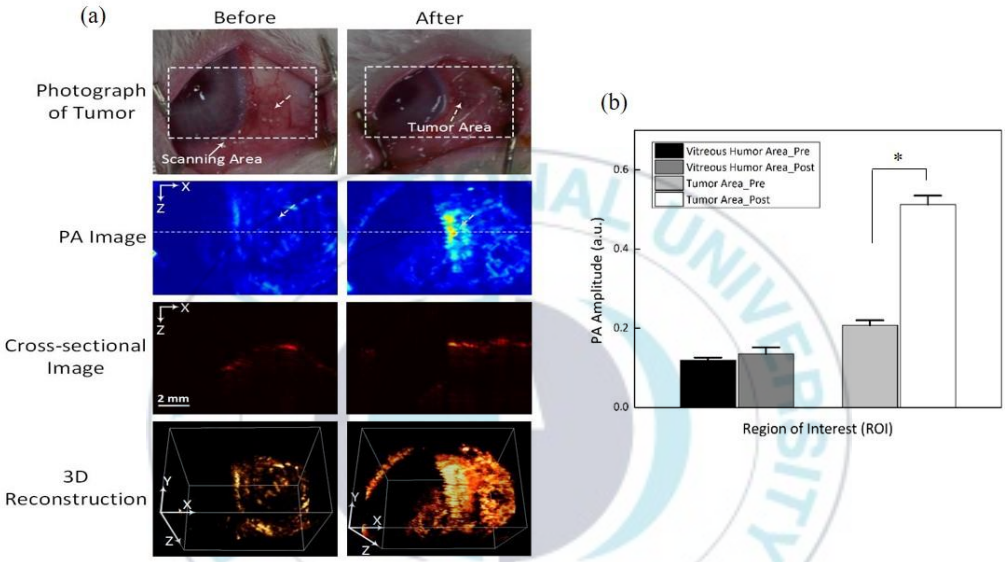

Figure 13. Photoacoustic imaging (PAI) of rabbit eye tumors injected with Dox-Fu@AuNPs. (a) Photographs of rabbit eye tumor were compared before and after Dox-Fu@AuNPs injection. (b) Photoacoustic signals from different positions in the rabbit eye tumor were compared before and after injection of Dox-Fu@AuNPs (*: $p < 0.05$ compared with pre-injection).

ostensibly visualized with high contrast due to strong light absorption from both the blood and the Dox-Fu@AuNPs. Cross-sectional images demonstrate the corresponding PA B-scan images acquired from the dotted lines to provide the axial penetration depth of the injected Dox-Fu@AuNPs. The post-injection PA image clearly shows the tumor filled with Dox-Fu@AuNPs whereas the cross-sectional image of the tumor before the injection is blurred and difficult to differentiate. The PA image of the tumor after the injection provides more than a 2-fold deeper image depth in the tissue, compared with the pre-injection (i.e., imaging depth = 2.8 ± 0.1 mm for post-injection vs. 1.4 ± 0.1 mm for pre-injection; $p < 0.001$). A 3D rendering PA image was reconstructed from a sequence of the B-scan cross-sectional images. The 3D image reconstruction was used to visualize the margins of the tumor and to evaluate the spatial distribution of the nanoparticles in the tumor. Obviously, the entire structure of the tumor volume was clearly visible upon the injection of Dox-Fu@AuNPs. In addition, the image after injection seemed larger, implicating the effective diffusion of Dox-Fu@AuNPs upon the injection. Quantitative measurements of the PA signals from regions of interest (ROIs) in Figure 13(b) were performed to differentiate the tumor areas from the surrounding vitreous humor [Figure 13(b)]. The PA image contrast of the post-injected tumor was approximately 2.6 times higher than that of the surrounding vitreous humor (i.e., PA amplitudes = 0.51 ± 0.02 for post-injection vs. 0.14 ± 0.02 for vitreous humor, $p < 0.001$). In contrast, the PA contrast of the pre-injection slightly increased, in comparison with that from of the surrounding area (i.e., PA amplitudes = 0.21 ± 0.01 for pre-injection vs. 0.12 ± 0.01 for vitreous humor; $p < 0.001$).

Histological analysis on the treated tumors at day 14 was also performed to investigate antitumor effects of Dox-Fu@AuNPs (Figure 14). Control images showed no evidence of anatomic disorganization of the tumor tissues. It was clearly observed that the morphology of cellular structures was unchanged and most nuclei were easily found, indicating that cancer cells were barely affected in the absence of Dox-Fu@AuNPs. In contrast, the samples treated with Dox-Fu@AuNPs only presented minute necrotic foci. The tissues treated with laser only and a combination of Dox-Fu@AuNPs and laser irradiation demonstrated distinct necrosis (Dox and thermal effects) in a superficial portion of the tumor and no or minimal damage to the peripheral tissues. The depth of the necrosis was estimated to be approximately 0.4 mm and 1.5 mm for the tissues treated with laser-only and with laser with Dox-Fu@AuNPs, respectively. Thus, the tissue necrosis induced by the combined treatment was approximately 4-fold thicker than that with laser only.

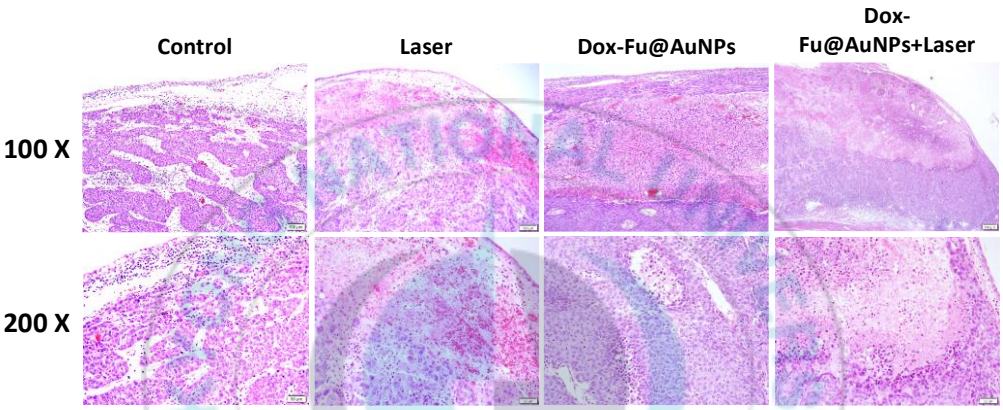

Figure 14. Histology images of tumor tissues obtained from four different groups 14 days after each treatment: rabbits treated with saline (control), laser only, Dox-Fu@AuNPs only, and Dox-Fu@AuNPs with laser irradiation.

2.4 Discussion and conclusion

AuNPs have been investigated as drug carriers, photosensitizer agents, and contrast agents for tumor targeting, imaging, and selective therapy [27]. As strong absorption of visible light by AuNPs can lead to heat generation, the unique plasmonic effect can be applied for PTT and PAI on solid tumors [29, 69]. The current study developed and synthesized AuNPs coated with Dox-loaded Fu for enhancing the synergistic effects of chemotherapy, the augmented heating for PTT, and the enhanced noninvasive photoacoustic image contrast for tumor margin identification and dual-treatment *in vivo*.

Recently, a number of inorganic nanoparticles have been widely investigated in imaging and treatment of tumors both *ex vivo* and *in vivo*, including gold nanoparticles (spheres, shells, rods, and cages) [70], carbon-based materials (SWNT, graphene, and carbon dot) [71, 72], magnetic nanoparticles [73], quantum dots, and ceramic nanoparticles [74]. However, the current nanoparticles are still limited by long-term toxicity, limited imaging resolution and penetration depth, and fast clearance by phagocytes (SPIO) [75]. Overcoming these challenges requires the development of an essential agent that reduces cytotoxicity, produces sufficient photoacoustic signals, and enhances photothermal efficiency. A great number of studies have reported the conjugation of AuNPs with different materials such as Prussian blue [29], polyelectrolyte [76], or thiolate chitosan as an alternative approach to reduce cytotoxicity. Other studies have focused on enhancing the biocompatibility and biodegradability of synthesized agents by loading them with organic dyes such in the

case of heparin-folic acid-IR-780 nanoparticles [77] or by loading hollow silica nanoparticles with hydrophobic phthalocyanine (Pc@HSNs) [78] or Zn(II)-phthalocyanine [79] or coating them with polyethylene glycol (PEG), including PEGylated WS2 nanosheets [80]. Most of the available photosensitizers are hydrophobic in nature and easily aggregate in physiological saline. To overcome these limitations, biocompatible AuNPs were synthesized by using a natural Fu as a conjugating and stable carrier for effective PTT therapy and PAI. Fu is a natural polymer with antitumor activity, no toxicity, and excellent biocompatibility and stability for cancer treatment [81-83]. Therefore, Fu plays a key role as a surface coating and reducing agent for the AuNPs core formation and leads to reduction of the toxicity of AuNPs and to the enhanced anti-tumor effects. In addition, to achieve effective tumor removal, the anti-cancer agent, Dox was integrated into Fu-coated AuNPs with over 90% loading efficacy, which was validated by a previous study [56]. The current study demonstrated a comparable cytotoxic effect of Dox over 200 μg/ml [Figure 8(a)]. In fact, the saturation concentration of Dox for conjugation within nucleus was reported to be 340 μM (i.e., 184.8 μg/ml) [84]. If the loading efficacy of Dox on Fu@AuNPs is considered over 90% [56], the cytotoxic effect could become comparable over 200 μg/ml of Dox-Fu@AuNPs (i.e., 180 μg/ml of Dox).

PTT on Dox-Fu@AuNPs caused cell death by damaging intracellular biomolecules and disturbing the membranes of intracellular organelles. The cell death was characterized as cell shrinkage, nuclear pyknosis (chromatin condensation), karyorrhexis (nuclear fragmentation), nuclei cleavage, and autophagic and

nonlysosomal disintegration by microscopic observations (Figure 10). Markovic *et al.* reported that the mechanism of photothermal killing of cancer cells involved oxidative stress and mitochondrial membrane depolarization, resulting in apoptotic and necrotic cell death characterized by caspase activation, DNA fragmentation, and cell membrane damage [85]. Thus, PTT increased apoptosis and necrosis through mitochondrial membrane depolarization. The loss of mitochondrial membrane potential, DNA fragmentation, and phosphatidylserine exposure were observed in the PTT-treated cells, which led to morphological and biochemical changes in the dying cells. However, the proposed particles were still associated with a relatively wide distribution in size. Thus, the controlled conjugation of Dox to Fu@AuNPs is currently under investigation to attain a uniform size of Dox-Fu@AuNPs. Although various studies have conducted PI fluorescence staining for detection of cellular death and cell cycle [56, 86, 87], the fluorescent emissions between PI and Dox are still undistinguishable. Therefore, flow cytometry or western blot will further be performed to define the cellular death and to confirm the current findings.

During 532-nm irradiation, Dox-Fu@AuNPs yielded no considerable heating effect at 0.06 W/cm^2, irrespective of concentration. However, the photothermal response was greatly enhanced as both irradiance and concentration were increased to 0.11 W/cm^2 and 200 μg/ml, respectively [Figure 7(a)]. Thus, small (~101 nm) Dox-Fu@AuNPs responded well to laser irradiation, and the temperature increase varied in an irradiance- and concentration-dependent manner. This result confirmed that only the highest concentration of 300 μg/ml reached tumor denaturation temperature. Yuan *et*

al. showed that a laser irradiance of approximately 433 W/cm^2 was required to reach the threshold temperature for tumor tissue denaturation (> 55 °C) [88]. However, the application of high intensity laser light for cancer treatment is always associated with thermal injury to the surrounding healthy tissues. In contrast, the proposed method used a relatively lower light intensity to photothermally treat small-sized eye tumors and to minimize the thermal injury to the peripheral tissues. To reach the threshold temperature for the tumor denaturation, the laser only treatment would require the irradiance of 0.55 W/cm^2, based upon the linear regression line [i.e., $y = 24.5 + 60.1 \times x$, where x = laser irradiance and y = peak temperature; Figure 7(b)]. On the other hand, the application of Dox-Fu@AuNPs was able to reduce the irradiance down to 0.11 W/cm^2 (i.e., 4.5 times lower) due to efficient optical energy coupling. Therefore, the proposed nanoparticles could be the potential photothermal agent to treat the eye tumors with minimal thermal injury to the adjacent tissue.

In vivo experiments presented that the combination of the laser irradiation and the nanoparticles induced temperature elevation up to 42.2 °C in less than 1 min, which is approximately 1.7 times high as that with laser only. The temperature rise can be attributed to the concurrent absorption of laser light by hemoglobin in the tumor and by Dox-Fu@AuNPs, leading to reduction of the treatment time, whereas no temperature increase was observed from the cells under laser irradiation without nanoparticles (laser only) due to weak absorption of the clear cells [89-91]. Unlike other conditions, the laser with Dox-Fu@AuNPs removed the tumors within six days without noticeable toxicity to the animals and recurrence over 14 days. This finding confirmed

that the both chemo- and photothermal effects successfully inhibited tumor growth without any adverse effects. It was also observed that Dox-Fu@AuNPs with or without laser irradiation was much greater than that of laser only due to anti-tumor effect of Dox. Importantly, all the treatments that used a single dose of the nanoparticles demonstrated a nonspecific effect to the surrounding tissues [77]. It is worth mentioning that chemotherapy-combined PTT can significantly improve treatment efficacy on eye tumors [92]. In addition, the current histological analysis merely presented the resultant necrosis 14 days after the treatment. Thus, TUNEL assay will further be conducted to detect apoptosis after the combined treatment. Furthermore, the acquired PA images (Figure 13) demonstrated that Dox-Fu@AuNPs obviously increased the image contrast in the tumor regions by 2.5-fold. The augmented contrast could result from strong absorption of 532 nm light by both blood and Dox-Fu@AuNPs in the tumor, which corresponds to the peak absorption wavelength of hemoglobin and Dox-Fu@AuNPs, as shown in Figure 6(h) and also reported by Prahl *et al*. [93]. This result implies that Dox-Fu@AuNPs could serve as effective contrast agents to enhance non-invasive PA imaging for cancer diagnosis. However, more effort is still required to systematically examine the potential long-term toxicity of the synthesized nanoparticles and the feasibility of the dual-theranostic agent at various doses in the animal models. In addition, the current histological analysis merely presented the resultant necrosis 14 days after the treatment. Thus, TUNEL assay will further be conducted to detect apoptosis after the combined treatment. Since solid tumors have wider and looser blood vessels (i.e., leaky vasculature; 200 nm ~ 1.2 μm in size

depending on tumor type) than normal tissue does (<10 nm in size) [94, 95], the current nanoparticles (116.7 ± 40.6 nm) may readily be transferred to and accumulated into the tumor due to enhanced permeability and retention (EPR) effect [96]. Intraperitoneal or intravenous injection of Dox-Fu@AuNPs will thereby be performed to identify the feasible detection of the tumor margin with PAI. Furthermore, synthesis of antibody with Dox-Fu@AuNPs will be conducted to enhance selective tumor targeting for the effective dual-treatment [97].

The current study investigated the feasible application of Dox-Fu@AuNPs for dual-treatment (chemo- and photothermal-) on eye tumor in vitro and in vivo. The fabricated Dox-Fu@AuNPs presented good stability in physiological environments and were non-cytotoxic to normal cells at the tested concentrations. On account of strong laser light absorption and high thermal conversion efficiency even at low doses, Dox-Fu@AuNPs generated both chemo and photothermal effects to completely remove the tumors. Both high photostability and molecular extinction coefficient enabled Dox-Fu@AuNPs to augment photoacoustic image contrast for the feasible identification of the tumor margins for the treatment. Therefore, Dox-Fu@AuNPs can be effective and safe nano-theranostic agents for imaging0guided dual-treatments for eye tumor.

Chapter 3. Newly-developed organic dye for effective photothermal cancer treatment

3.1. Introduction

In worldwide, cancer has become a major problematic health issue. Despite existence of conventional cancer treatment such as surgery, radio- and chemotherapy, complete cancer treatment still remains challengeable due to high recurrence rate and drug resistance [12]. Recently, photothermal therapy (PTT) has been shown attractive attention as a non- or minimally invasive treatment. Basically, PTT utilizes photoabsorbing agents to locally generate volumetric heat in tumor tissue upon light absorption, leading to thermal necrosis [13]. However, as PTT own several side effects such as phototoxicity and limited efficacy, nanotechnology-based applications have been widely investigated for effective PTT treatment [26]. For example, functionalized gold nanoparticles and carbon nanomaterials can induce the desired photothermal effects on cancer without systemic toxicity [28, 29]. In addition, multifunctional nanomaterials for dual treatment have been reported for synergistic therapeutic efficacy compared to single treatment [98].

To date, Development of inorganic photothermal agents has been widely investigated to achieve excellent photothermal performance. Nevertheless, due to several long-term safety concerns of inorganic materials, organic photothermal agents such as conjugated polymer and small molecules are utilized with better

biocompatibility [31-33]. For instance, IR-780 dye exhibited superior photothermal efficacy and feasible imaging modality on breast cancer cell [77]. However, several conventional organic photoabsorbing agents presented some shortcomings such as low photostability and hydrophobicity [16, 99, 100]. Especially, complicated reaction processes such as introduction of hetero atoms and long alkyl and/or bulky chains could affect stability in physiological conditions and toxic degradation and aggregation problems, implicating disadvantage for further commercialization [101, 102]. Therefore, simple design toward small organic agents have been desired with effective PTT performance.

The current study aims to develop a novel organic PTT application through simple one step reaction with twisted structure with strong D-A force and various intramolecular vibrators and rotators, and evaluate the preclinical feasibility in *in vitro* and *in vivo*. We hypothesized that the proposed organic dye led to enhanced cancer cell destruction due to excellent photothermal conversion under laser irradiation. In this study, photothermal effects of NI2 NPs were evaluated under 691 nm laser irradiation and the anti-cancer effects of NI2 NPs were confirmed on CT26 murine colon cancer cells and tumor tissues to ensure treatment efficacy.

3.2 Materials and methods

3.2.1 Preparation of photothermal agents

NI2 NPs were synthesized and prepared as photoabsorbing agents for photothermal therapy. In brief, 1 ml of NI2 solution in THF (2.5 mM) was slowly added dropwise to 10 ml distilled water. The blue obtained solution was kept blowing air overnight in order to complete evaporation of THF. The final NI2 NPs were filtrated by a 200 nm syringe filter.

3.2.2 Photothermal effect of NI2 NPs

Photothermal performance of PA2 was evaluated by using a 691 nm laser system with a 600-μm multimode end-firing flat fiber. A photodiode sensor (PD-300-3W, Ophir, Jerusalem, Israel) in conjunction with a power meter (Nova II, Ophir, Jerusalem, Israel) validated the output power from the fiber before each test to warrant the identical irradiance conditions. To identify the optimal concentration for in vitro and in vivo testing, we initially tested five different concentrations of PA2 mixed with distilled water (0 of distilled water, 25, 50, 75, and 100 μM) in 96-well cell culture plates under irradiation at 1 and 1.5 W/cm^2 for 150 s. The 690 nm laser light was widely illuminated to cover the entire surface area of each well in the 96-well plates and irradiated perpendicularly onto the surface of the solution. An infrared (IR) camera (A325, FLIR, Wilsonville, Oregon, USA) was used to monitor the temperature changes in the PA2 aqueous solution in real time. Each test was repeated four times (N = 4). To assess

photothermal stability (PS) of PA2, four cycles of the 690 nm laser irradiation were performed. 100 μM of PA2 solution was initially irradiated at 1 and 1.5 W/cm^2 for 150 s (ON time; corresponding fluence rate = 150 and 225 J/cm^2, respectively). Then, the laser irradiation was discontinued for another 450 s (OFF time). The ON/OFF cycles were repeated four times, and the IR camera recorded the entire cycles to evaluate PS of PA2.

3.2.3 *In vitro* cytotoxicity test

In present study, CT26, murine colon cancer cells were used for in vitro and in vivo study. CT26 cells were procured from Korean Cell line bank and cultured in Dulbecco's modified Eagle's medium (DMEM, Corning, NY) containing with 10 % Fetal Bovine Serum (FBS, Corning, NY) and 1 % antiobiotic-antimycotic (Gibco, Grand Island, NY). The cells were maintained in a humidified incubator with 5 % CO_2 at 37 ℃ and were passaged via trypsinization.

CT26 cells were seeded in a 96-well microplate at a density of 2 x 10^4 cells/well in culture medium and incubated for 24 h to allow 80 % confluence to grow. The cultured cells were then washed with PBS and incubated with NI2 NPs solution with various concentrations (0, 25, 50, 75, and 100 μM/ml) for 24 h. The cells without NI2 NPs solution were considered as a control. Then, the standard cell viability assay using 2-(4,5-dimethylthiazol-2-yl)-2,5-diphenyltetrazolium bromide (MTT) was performed to evaluate cytotoxicity of NI2 NPs. In brief, MTT solution at 1 mg/ml

concentration was added to each well plate and kept for 4 h at 37 ℃. Then, 100 µl of dimethyl sulfoxide (DMSO) was added to dissolve the formed formazan for another 20 min. the absorbance was determined at 540 nm by a microplate spectrophotometer (Multiskan Go, Thermo Fisher, Waltham, MA). The cell viability was expressed as the relative percentage by normalizing to control group.

3.2.4 Photothermal therapy on CT26 cells

CT26 cells were seeded and divided into four different groups to examine PTT effect against cancer cells: control (CTRL), laser only (Laser), NI2 NPs only (NI2 NPs), NI2 NPs-assisted PTT (Laser+NI2 NPs). After 24 h incubation, Cells were washed with PBS and treated with 100 µM of NI2 NPs solution or medium alone and irradiated by 691 nm laser at 1.5 W/cm^2 for 150 s or no laser. Thereafter, MTT assay was conducted to confirm cellular viability after each treatment. Additionally, Live and dead cell staining was performed to verify photothermal effect on cancer cells by using both the fluorescein diacetate (FDA) and propodeum iodide (PI). 5 mg of FDA in 1 ml acetone and 2 mg of PI in 1ml PBS were prepared and mixed with 5 ml of serum free media, 8 µl of FDA solution, and 50 ul of PI solution. All groups of cells were incubated with the staining solution for 5 min at 37 ℃. The cells were then washed with PBS and observed under a fluorescence microscope (CKX53, Olympus, Tokyo, Japan). The relative fluorescence intensities of green and red colors were quantified by using image

J (National Institute of the Health, Bethesda, MD, USA). The green and red colors represent viable and non-viable cells, relatively.

3.2.5 *In vivo* validation of PA2

16 nude mice (5 weeks old, female) were purchased from Hana biotech (Suwon, Republic of Korea) and utilized for establishing subcutaneous colon cancer models. Suspension of CT26 cells (1.5 x 10^6 cells/ml) were subcutaneously injected into the back of each mouse and the mice were housed in the pathogen-free cage. After one week, the mice were randomly divided into four groups: CTRL, Laser, NI2 NPs, Laser+NI2 NPs. Prior to experiments, the mice were anesthetized with 3% isoflurane (Terell^{TM} isoflurane, Piramal Critical Care, Bethlehem, PA, USA) with oxygen (0.6 L/min). Then, CT26 tumors were intratumorally with saline or 100 μM of NI2 NPs solution and illuminated by 691 nm laser (1.5 W/cm^2 for 150 s). During laser irradiation, a real-time IR thermal camera was used to monitor temperature increasing in the tumor site. A single treatment was applied to all the animals, and a beam size from an optical fiber was adjusted to cover the entire tumor area. All the groups of mice were monitored and photographed by using a digital camera (D5100, Nikon, Tokyo, Japan) at four different time points: 0 (D 0), 3 (D 3), 7 (D 7), and 10 days (D 10) after each treatment. The tumor volume of each mouse was calculated by using the formula (tumor volume = length x width^2). During in vivo tests, all the animals were maintained at an animal research facility under standard conditions and all procedures followed the guidelines

of the Korean National Institutes of Health (KNIH) on the care and use of laboratory animals. The procedure was approved by the Institutional Animal Care and Use Committee at Pukyong National University (Permit Number: PKNUIACUC-2021-04).

3.2.6 Histological analysis

To evaluate treatment efficacy of NI2 NPs-assisted PTT, all CT26 tumor bearing mice were euthanized with overdose of CO_2 gas ten days after treatments. The harvested tumor tissues were fixed in a 10% neutral formalin solution (Sigma Aldrich, St. Louis, MO, USA) for three days. After the fixation, the acquired samples were processed into paraffine and sectioned at 5 μm. Thereafter, the sectioned slides were stained with hematoxylin and eosin (HE) to identify the extent of damage in the tumor tissue after NI2 NPs-assisted PTT. All slides were scanned and confirmed under optical microscopy (Motic easyscan, Motic, Kowloon, Hong Kong).

3.2.7 Statistical analysis

All experiments were repeated four times, and all the data were expressed as mean ± standard deviation. For non-parametric statistical analysis, the Mann-Whitney U test with Bonferroni correction (MU) were performed by using SPSS software 22 (SPSS Inc., Chicago, IL, USA), and $p < 0.05$ was considered statistically significant.

3.3 Results

3.3.1 Characteristics of PA2

NI2 NPs were conveniently synthesized from commercial agents and simple one-step-reaction and one-step-reprecipitation (Fig. 15). Through reprecipitation method, the size of NI2 NPs was estimated with hydrodynamic diameters of 75.2 nm. Nanosized of NI2 NPs can be employed as a promising anti-cancer application owing to the passively tumor target via enhanced permeation and retention (EPR) effect. The zeta potential of NI2 NPs were measured to be -41.7 mV, indicating stable colloids formation. As shown in Fig. 16, the absorption spectrum was measured to confirm that the peak absorption occurred at 690 nm in organic solvents. However, non-fluorescence emission was detected due to nonradiative decay for thermal deactivation. These results suggested that the proposed NI2 NPs could be a highly potential photoabsorbing agents for photothermal cancer treatment.

3.3.2 Photothermal evaluations

Photothermal behaviors of NI2 NPs were examined at various concentrations and irradiation times under 691 nm laser at 1 and 1.5 W/cm^2 (Figure 17). Regardless of laser irradiance, temperature was increased linearly with the concentration of NI2 NPs for 150 s irradiation. An insignificant temperature change was observed when distilled water was exposed to laser light (from 1 to 1.5 W/cm^2). As shown in Figure 17, the maximum temperature changes at 100 μM of the NI2 NPs solution were confirmed

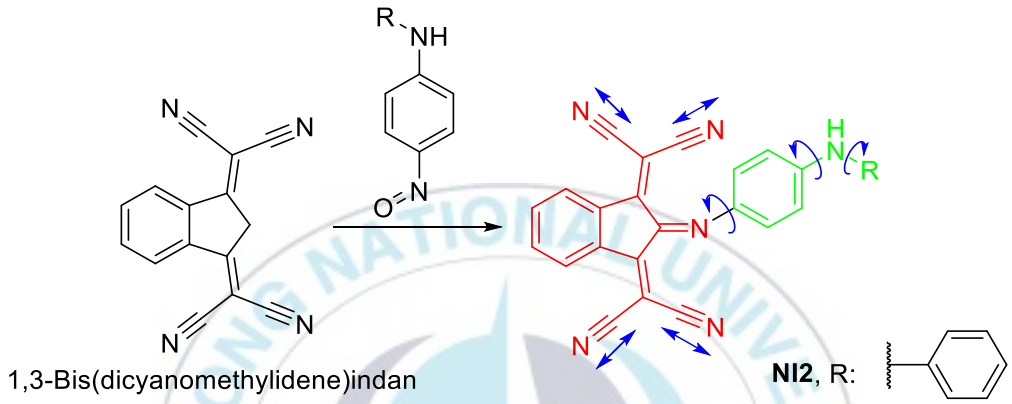

Figure 15. Synthesis of NI2 NPs**.**

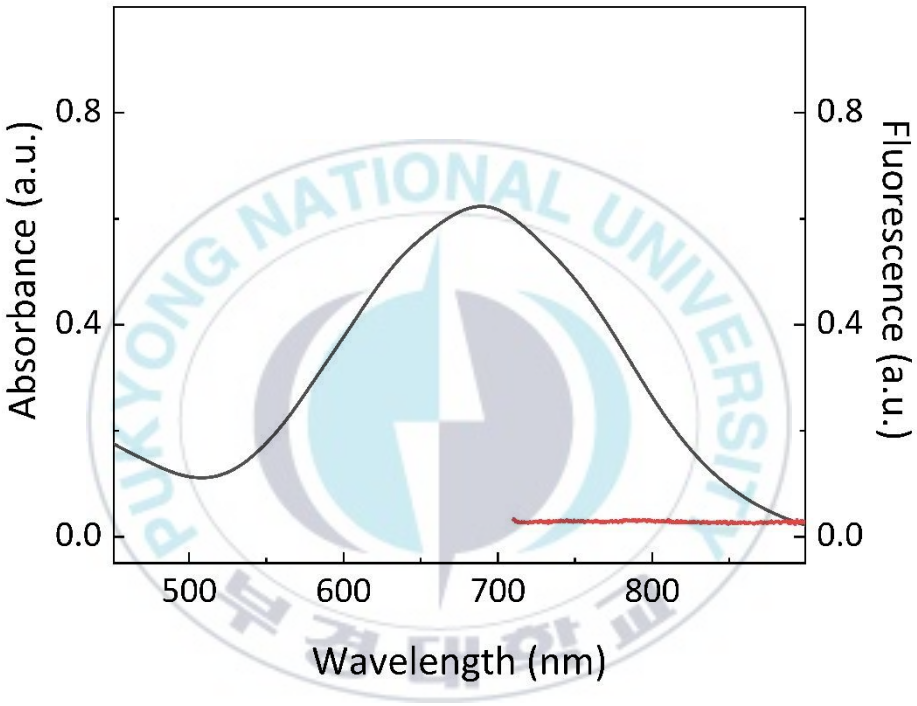

Figure 16. Absorption (black line) and Fluorescence emission (red line) spectra of NI2 NPs in DMSO

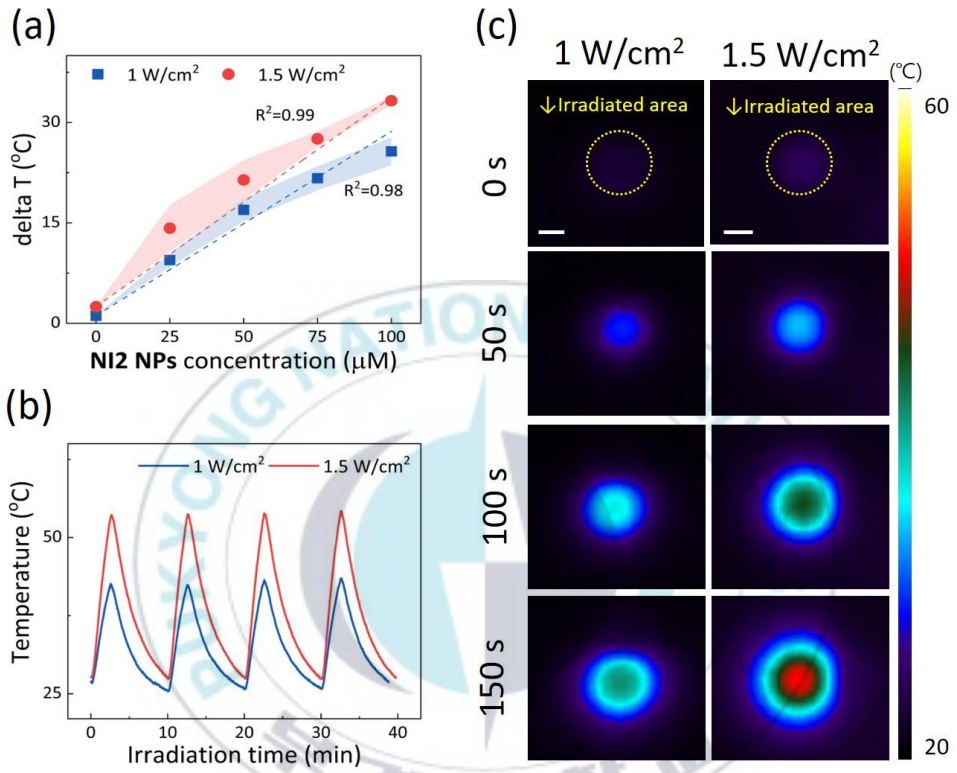

Figure 17. Thermal responses of NI2 NPs to 691 nm laser irradiation at 1 and 1.5 W/cm^2: (a) temperature elevations measured from NI2 NPs aqueous solutions with various concentrations (0 for distilled water, 25, 50, 75, and 100 μM) after 150 s irradiation, (b) photothermal stability (PS) of NI2 NPs solution (100 μM) under four ON/OFF cycles of laser irradiation (ON/OFF time = 150 s/450 s; duty cycle = 25%), and (c) infrared thermal images of NI2 NPs solution (100 μM) captured at various irradiation times (scale bar = 5 mm).

(42.8 and 54.4 ℃ for 1 and 1.5 W/cm^2, respectively). Figure 17(b) shows the temperature variations in the NI2 NPs under four cycles of 690 nm irradiation for photothermal stability evaluation. The thermal profiles of NI2 NPs were unchanged for both the irradiances under four ON/OFF cycles of laser irradiation. The maximum temperature was consistently maintained at 42 and 53 ℃ for 1 and 1.5 W/cm^2, respectively. Fig. 17(c) presents infrared thermal images of NI2 NPs captured at various irradiation times. The maximum temperature occurred at the center of the irradiated spot, and the temperature gradually decreased with radial distance from the center because of a Gaussian beam profile. These results indicate that NI2 NPs could effectively convert optical energy to thermal energy with excellent PS in water. Since over 50 ℃ could induced irreversible thermal damage to tissues [18], the irradiation condition of 1.5 W/cm^2 for 15- s was selected for further in vitro and in vivo experiments.

3.3.3 *In vitro* cytotoxicity and PTT

MTT assay was used to evaluate the cytotoxicity of NI2 NPs and photo-cytotoxicity effect of NI2 NPs-assisted PTT on CT26 cells. As shown in Fig. 18(a), the cell viability of CT26 cells slightly changed even at the highest concentration of 100 μM without laser irradiation. Therefore, 100 μM of NI2 NPs was selected for further in vitro and in vivo studies. However, once 691 nm laser light irradiated on NI2 NPs-treated cells, the photo-cytotoxicity dramatically increased, implicating that NI2-

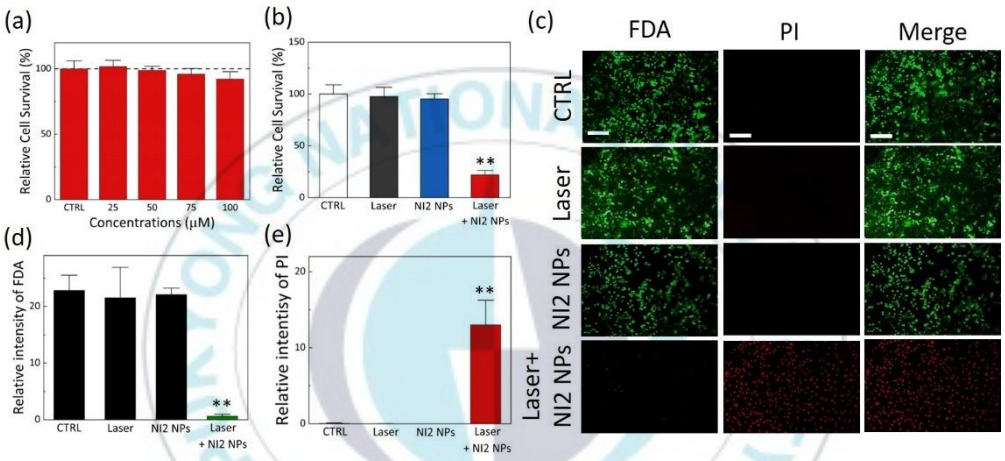

Figure 18. In vitro photothermal effects with NI2 NPs on CT26 cells: (a) Relative cell survival rate of CT26 cells treated with different concentrations of NI2 NPs (0, 25, 50, 75, and 100 μM), (b) relative cell viability treated with laser (1.5 W/cm^2) only, NI2 NPs (100 μM) only, and laser+NI2 NPs (laser at 1.5 W/cm^2 + 100 μM of NI2 NPs), and (c) fluorescein diacetate/propidium iodide (FDA/PI) staining. Green and red colors represented viable and dead cells, respectively (scale bar = 200 μm). Relative (d) FDA and (e) PI intensities were quantified for various treatment groups (N = 4; **MU $p <$ 0.005 vs. CTRL)

NPs-assisted PTT promoted an efficient killing of CT26 cells (Fig. 18(b)). In live and dead cell staining (Fig. 18(c)), NI2 NPs-assisted PTT group showed strong red fluorescence, representing a large number of non-viable cells after laser irradiation (Fig.18 (d)). On the other hand, green fluorescence was vividly observed in other groups (Control, Laser only, and NI2 NPs only), indicating viable cells (Fig. 18(e)). Therefore, the data suggested that NI2 NPs-assisted PTT effectively induced the CT26 cell death.

3.3.4 *In vivo* PTT

To assess anti-tumor efficacy of NI2 NPs-assisted PTT against CT26 cells, CT26 cells were xenografted into nude mice. The anti-tumor efficacy was evaluated for four different groups: control, Laser only, NI2 NPs only, NI2 NPs-assisted PTT. During laser irradiation, temperature monitoring was conducted to confirm photothermal effects of NI2 NPs (Fig. 19). Compared to Laser only group, NI2 NPs-assisted PTT group presented a 1.5-fold higher maximum temperature (up to 61.3 ± 3.2 ℃), leading to irreversible thermal damage to tumor tissue (Fig. 19(a)). Whereas laser only group increased temperature in tumor due to absorption of tissue chromophores, the maximum temperature was insufficient to induce tumor cell necrosis (Fig.19(b)). As shown in Fig. 20(a) and (b), the tumor volume from NI2 NPs-assisted PTT almost completely removed on Day 10 after the laser irradiation, whereas the tumor masses from other groups gradually increased. It was noticed that thermal-induced necrosis was observed on the surface of tumor tissues after NI2 NPs-assisted PTT, whereas laser

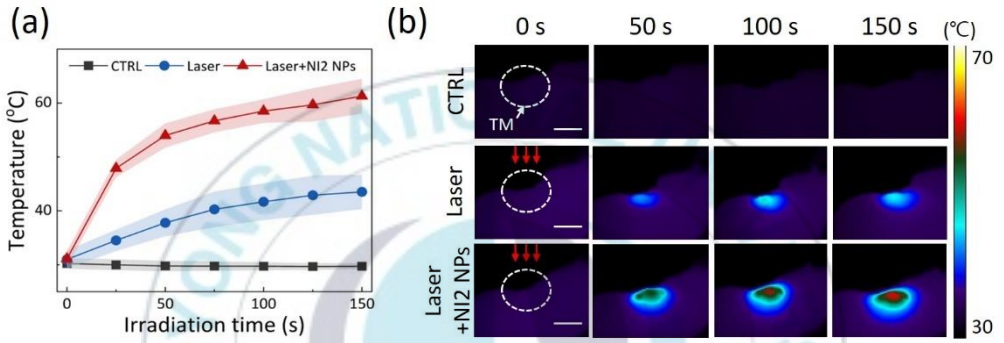

Figure 19. *In vivo* temperature measurement of NI2 NPs-assisted photothermal treatment (100 μM and 1.5 W/cm^2 for 150 s) on CT26 tumor mouse model: (a) temporal development of temperature for 150 s and (b) corresponding thermographic images captured at various time points (N = 4; CTRL = control; TM = tumor region; scale bar = 10 mm). Note that a white arrow in (b) indicates the direction of laser irradiation.

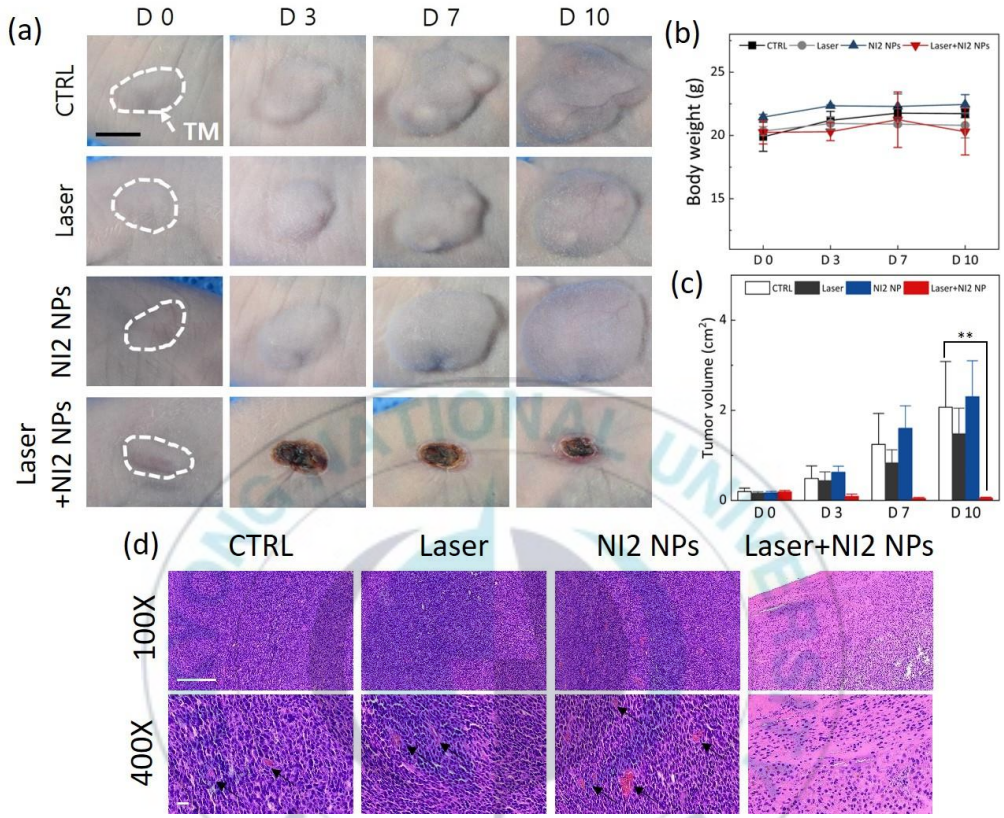

Figure 20. In vivo antitumor effect of NI2 NPs-assisted photothermal treatment: (a) compilation of top-view images captured at various time points after PTT (TM = tumor region; D = day; scale bar = 10 mm), changes in (b) body weight and (c) tumor volume of treated tumor, and (d) HE-stained imaged of harvested tumor tissues from four treatment groups at D 10 (top row = 100 X and scale bar = 100 μm; bottom row = 400 X and scale bar = 30 μm). Note that black arrows in (d) indicated the position of blood capillary. (N = 4 per group; **MU $p < 0.005$ vs. CTRL).

only accompanied with rapid tumor growth without any damage. The weights of mice had no variations for entire ten days (Fig. 20(c)).

Euthanized mice tissues after ten days were analyzed by using HE staining for histological analysis. In Fig. 20(d), the tumors treated with NI2 NPs-assisted PTT only exhibited necrosis in contrast to other groups. Furthermore, the tumors of other groups (control, laser only, NI2 NPs only) presented micro vessels and necrosis in deep portions of tumor, indicating that the hypoxic response to excessive proliferation of the tumor cells after the incomplete treatment.

3.4 Discussion and conclusion

Therapeutic approaches of PTT have been widely studied for effective cancer treatment on various tumors [58]. For clinical translation of PTT, the role of photoabsorbing agents is pivotal in extending the number of choices of treating cancers. A number of studies have evaluated the function of organic dyes as a powerful photoabsorbing agents in terms of in vitro treatment efficacy [31-33]. For example, D-A conjugated small molecules generated sufficient level of temperature that could induce breast cancer cell necrosis [32]. These results suggested that the organic dye-assisted PTT be a promising approach for treating various tumors.

No side-effects with NI2 NPs were identified during the current PTT testing at the therapeutic dosage, and the treatment can be relatively safe to administer. However, the current safety evaluations on NI2 NPs-assisted PTT are rather limited, and further assessments are necessary to ensure the safety of the proposed PTT for clinical translation on cancer. In addition, spatial distribution of the incident laser light can typically determine the degree of heat generation due to interactions between the light and photoabsorbing agents. As the shape of tumor is three-dimensional or elliptical, circumferentially deliver of laser light by an optical diffuser can enhance therapeutic outcomes in comparison with flat fibers. Therefore, further light distribution study will be conducted to compare therapeutic outcomes between flat and optical diffuser.

Recently, multimodal approaches have been widely studied with PTT in conjunction with other therapeutic and diagnostic modalities or combined therapy [32]. For example, Tian et al. examined photothermally enhanced photodynamic therapy by using nanosized graphene oxide and chlorin e6 conjugation on nasopharyngeal epidermal carcinoma cell [30]. The synthesized GO-PEG-Ce6 showed synergistic therapeutic effects in cancer cell compared to individual photothermal or photodynamic therapy. Furthermore, designed cooper-based nanoparticles have promising theranostic potential for cancer treatment due to biocompatibility, high photothermal conversion efficacy, and CT imaging capability [103]. In accordance with a large number of researches, the combined treatment strategy has shown promising results. Additionally, specific targeting to cancer cells has been considered as a main limitation for photothermal agents to prevent normal tissue damage [97]. Therefore, further investigations will develop and modify the proposed organic dye by conjugating cancer-specific antibody or surface modification.

Chapter 4. Micro-lens array (MLA)-assisted photothermal effects for enhanced fractional cancer treatment

4.1. Introduction

Colorectal cancer (CRC) is the fourth most common cancer in women and the fifth most common cancer in men due to poor diet, smoking, excessive drinking, and obesity [104]. CRC is also the third leading cause of cancer-related death in United States. Most CRCs start to develop from polyps in the colon, which is easy to remove and if left untreated, can change into malignant cancer with time [105]. Despite conventional treatments, such as radiotherapy and chemotherapy, CRC is still associated with high mortality and recurrence as a result of incomplete treatment on the tumor region [106, 107]. Therefore, development of a new therapeutic modality for CRC is pivotal in advancing clinical outcomes and warranting treatment safety.

Photothermal therapy (PTT) has been widely studied as a non- or minimally-invasive and effective cancer treatment. The primary purpose of applying PTT is to locally deposit volumetric heat in tumor tissue upon light absorption, leading to irreversible thermal injury and cell apoptosis as well as necrosis [17]. Photothermal agents are often used to selectively absorb the incident light and to confine the induced thermal effects specifically to the targeted tissue. A number of research studies have reported various nanomaterials to enhance photothermal effects during the tumor

treatment. For instance, application of gold nanoparticles can induce a temperature increase in the tissue in terms of exclusive surface modifications and high light absorption at the wavelength of 532 nm [98, 108, 109]. Functionalized carbon nanomaterials have widely been investigated for drug delivery vehicles, biomedicine, and photothermal agents [110-112]. A bare-cut flat fiber (Flat) is typically employed to deliver laser light to tumor tissue for PTT. However, due to a Gaussian beam profile, the tumor with a three-dimensional irregular shape often experiences non-uniform distributions of light and laser-induced temperature during the Flat-based irradiation [37]. As a result, development of the inhomogeneous temperature in the tumor weakens therapeutic effects and eventually leads to the incomplete treatment of the target cancer cells. As a result, the remaining cancer cells can regrow, the tumor recurrence ensues, and the survival rate goes down.

Laser treatments in dermatology often employ multi-lens arrays (MLA) for delivery of fractional laser light in order to uniformly distribute micro-beams on skin tissue. The fractional laser treatment with MLA is a minimally invasive treatment method that can entail microscopic thermal lesions without minimal thermal injury [113]. MLA delivers multiple micro-beams at high fluences whereas Flat transmits a single macro-beam at low fluences [114]. Thus, unlike Flat-based irradiation, MLA-assisted irradiation can accompany wide and uniform distributions of temperature in the tissue upon light absorption. In fact, the fractional skin treatment with the micro-beams can accelerate skin rejuvenation and the recovery of the treated skin by

preserving healthy surrounding tissue, compared to the flat-beam skin treatment [115].

The aim of the present study was to demonstrate a therapeutic capacity of MLA-assisted fractional laser treatment on tumor, in comparison with Flat-based laser treatment. We hypothesized that the MLA-assisted irradiation could induce spatially wide and uniform temperature profiles in the tumor and effectively eradicate cancer cells with generation of microscopic thermal lesions in the tissue. Continuous laser irradiation in conjunction with a photothermal agent was employed to augment coupling efficiency and conversion of optical energy into thermal energy during PTT [116]. The proposed treatment method was validated theoretically and experimentally to confirm laser-induced thermal responses of *in vivo* tumor models to the MLA-assisted irradiation. Histological analysis was examined to assess the degree of thermal damage to warrant treatment efficacy and safety of the proposed MLA-assisted PTT.

4.2 Materials and methods

4.2.1 Light source

The current study employed a 1064 nm laser system (FC-W-1064B-30W, CNI, Changchun, China) to induce photothermal effects. A 600-μm multimode end-firing flat fiber (Flat; multimode optical fibers; 600 μm core diameter, Thorlabs Inc., Newton, New Jersey, USA) and multi-lens arrays (MLA; fused silica; focal length = 40 mm; 145 micro-beams; micro-beam diameter = 350 μm; macro-beam diameter = 8 mm; Bluecore company, Busan, Republic of Korea) were used to deliver laser light (Fig. 21(a)). For direct comparison, the identical beam diameter of 8 mm was applied for both Flat-based and MLA-assisted irradiations. The applied power ranged from 0.5 to 1.5 W (irradiance =1 ~ 3 W/cm^2), and the irradiation time was 180 s. A power detector (PD-300-3W, Ophir, Jerusalem, Israel) in conjunction with a power meter (Nova II, Ophir, Jerusalem, Israel) measured laser power from Flat and MLA before and after each test to replicate the identical experimental conditions.

4.2.2 Numerical simulation for temperature assessments

We initially performed numerical simulations on photothermal responses of gelatin phantoms to compare effects of Flat and MLA on spatial distributions of temperature and experimentally validated the simulation results. IR 1061 dye was used as a chromophore to absorb 1064 nm laser light for thermal assessment.

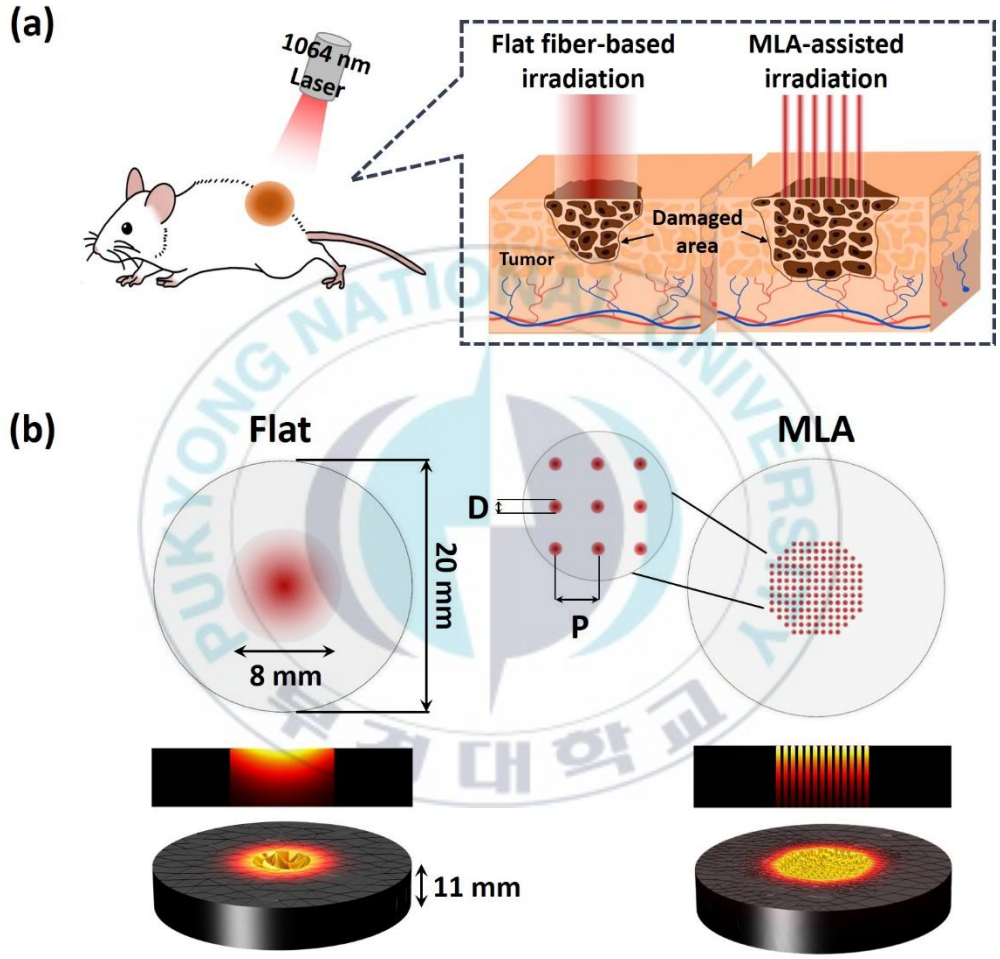

Figure 21. Schematic representations of (a) laser irradiation with flat fiber (Flat) and micro-lens arrays (MLA) on *in vivo* tumor model and (b) geometry of gelatin phantom (20 mm in diameter and 11 mm in thickness) for numerical simulation of laser irradiation with Flat and MLA (D = micro-beam diameter of 350 μm; P = distance between two consecutive micro-beams of 500 μm)

Numerical simulations were conducted to predict instant thermal responses of gelatin phantoms mixed with IR 1061 dye to laser irradiations with Flat and MLA by using COMSOL software (5.3, COMSOL Multiphysics, COMSOL Inc., Burlington, MA, USA). Figure 21(b) displays a geometry of the phantom model (20 mm in diameter and 11 mm in thickness). 1-W 1064 nm laser light was perpendicularly irradiated on the top surface of the phantom for 15 s. Flat delivered a Gaussian beam distribution with a diameter of 8 mm in a single beam spot while MLA had 145 uniformly-distributed micro-beams in an 8-mm macro-beam spot (micro-beam diameter = 350 μm and distance between two consecutive micro-beams = 500 μm). The corresponding irradiance was 1 W/cm^2. Volumetric heat generation (Q, W/cm^3) induced by light absorption was described as follows [90]:

$$Q = \mu_a I(r, z) \quad (1)$$

where μ_a, I, r, and z are absorption coefficient (mm^{-1}), fluence rate (W/cm^2), radial distance (mm), and depth (mm). For the Flat irradiation, I(r,z) was described as follows:

$$I(r, z) = \frac{P}{\pi {r_0}^2} \exp(-\mu_a z) \quad (2)$$

where P and r_0 are laser power (W) and the irradiated beam radius (mm). For the MLA irradiation, I(r,z) reflected uniform distributions of multiple micro-beams on the phantom surface (xy-plane; Fig. 21(b)) as follows:

$$I(r, z) = \frac{P}{\pi {r_0}^2} \exp\left(-\frac{r^2}{{r_0}^2}\right) \exp(-\mu_a z) \quad (3)$$

The Pennes' bio-heat transfer equation was then used to describe temperature development in the phantom model [90]:

$$\rho C_p \frac{\partial T}{\partial t} + \rho C_p \vec{u} \cdot \nabla T = \nabla \cdot (k \nabla T) + Q \quad (4)$$

where ρ, C_p, T, t, $\vec{u}$, and k, are density of the phantom (kg/m^3), specific heat for the phantom (J/kg·K), temperature (K), time (s), normal vector for heat transfer, and thermal conductivity of the phantom (W/m·K). The initial temperature of the gelatin phantom was set at 5 °C. Convective heat transfer was applied on the top surface of the phantom by using the following equation [90]:

$$-\vec{\mathbf{n}} \cdot (-k\nabla T) = h(T - T_{air}) \quad (5)$$

where **n**, h, and T_{air} are normal vector of heat flux, convective coefficient (W/ m·K), and ambient air temperature (20 °C). The rest of the phantom surfaces was assumed to be insulated (**n**·k·▽T = 0 according to Neumann boundary condition). Table 3 summarizes all the physical properties used for the numerical simulations [117-119].

4.2.3. Phantom evaluations

Gelatin-based phantoms were fabricated and tested to validate numerical simulations on spatial distributions of temperature after Flat-based and MLA-assisted irradiations. 10% (w/v) gelatin power (Sigma Aldrich, St. Louis, MO, USA) was mixed with distilled water at 70 °C until the power completely melted. Then, 0.03% (w/v) IR 1061

Parameters	Value
Absorption coefficient (μ_a, mm^{-1})	1
Density (ρ, $kg \cdot mm^{-1}$)	1060
Thermal conductivity (k, $W/m \cdot K$)	0.303
Specific heat (C_p, $J/kg \cdot K$)	3600
Beam radius (r_0, mm)	6
Convective heat coefficient (h, $W/m^2 \cdot K$)	10
Air temperature (T_{air}, K)	393.15
Laser power (P, W)	1

Table 3. Summary of thermo-physical properties used for numerical simulation

dye (Sigma Aldrich, St. Louis, MO, USA) was added to the prepared mixture as a chromophore to absorb the incident 1064 nm laser light. The final mixture was poured into a 6-well culture plate, and the plate was stored at 4 ℃ overnight for sufficient solidification. The 1064 nm laser light was irradiated at 1 W/cm^2 for 15 s with Flat and MLA on the prepared phantoms (20 mm in diameter and 11 mm in thickness). Each test was repeated four times (N = 4). Both top-surface and cross-section of each treated phantom were photographed to assess the extent of gelatin removal as a result of Flat-based and MLA-assisted photothermal interactions. Image J (National Institute of Health, Bethesda, MD) was used to measure the physical dimensions of all the ablated craters and to estimate the corresponding ablation volume for quantitative comparison.

4.2.4 Aqueous solution experiments

To identify the appropriate treatment conditions for *in vivo* testing, we tested four different concentrations of IR 1061 dye in PBS (0, 100, 200, and 300 μg/ml in PBS) in 24-well cell culture plates with three different irradiances (1, 2, and 3 W/cm^2; irradiation time =180 s). The solutions were poured in 24-well cell culture plates (each volume of well: 500 μl). 1064 nm laser light was irradiated perpendicularly on the solution surface by means of using Flat and MLA. Each test was repeated four times (N = 4). A thermal imaging infrared (IR) camera (A325, FLIR, Wilsonville, Oregon, USA) was used to monitor spatio-temporal developments of the temperature on the solution surface during the laser irradiation. After 180-s irradiation, IR images were

captured from the two conditions. The temperatures at the central (T_C) and peripheral (T_P) regions were measured from the IR images for direct comparison. T_C represents the maximum temperature after the laser irradiation, and T_P indicates the temperature at the outmost boundary of the beam spot (r = 4 mm). Based on the dosimetry findings, *in vivo* experiments selected the following conditions: dye concentration = 300 μg/ml in PBS: laser irradiance = 2 W/cm^2; irradiation time = 180 s).

4.2.5 In vivo validations

CT26 murine colon cancer cells were used to fabricate *in vivo* tumor models for comparing two different irradiation modes. The CT26 cells were obtained from Korean Cell line bank and cultured in Dulbecco's modified Eagle's Medium (DMEM, Corning, NY) with 10% fetal bovine serum (FBS, Corning, NY) and 1% antibiotic-antimycotic (Gibco, Grand Island, NY). The prepared cancer cells were kept in a humidified incubator at 37 ℃ with 5% CO_2 atmosphere.

12 Balb/c female mice (age = 5 weeks; and weight = 20-25 g) were obtained from Hana Biotech (Suwon, Republic of Korea) to create tumor models. All the animals were individually housed in a pathogen-free cage at the Animal Research Centre facility under standard conditions. All the mice were acclimated for a week, and then, the prepared CT26 cancer cells ($3x10^5$ cells) were injected into the back of each mouse and incubated for a week to grow the tumors. Each mouse was randomly divided into three groups for comparison (N = 4 per group): control, Flat, and MLA. Before

experiments, all the mice were anesthetized in a chamber using a respiratory anesthesia system (Classic T3, SurgiVet, USA) with 3% isoflurane (Terrell^{TM} isoflurane, Piramal Critical Care, Bethlehem, PA, USA) in oxygen (0.6 L/min). A week after the injection of the cancer cells, diluted IR 1061 dye (concentration = 200 µg/ml in PBS) was administered into each animal intra-tumorally to selectively absorb the incident 1064 nm laser light for PTT. Two hours after the dye injection, the tumor-bearing models were irradiated with 1064-nm laser light at 2 W/cm^2 for 180 s (selected from solution experiments) using Flat and MLA. The current study applied a single treatment to all the animals. A thermal imaging IR camera was employed to monitor temperature elevations in the tumor during the laser irradiation. Then, all the treated tumors were monitored and photographed by using a digital camera (D5100, Nikon, Tokyo, Japan) at four different time points: 0 (D 0), 3 (D 3), 7 (D 7), and 14 (D 14) days after the laser treatment. Image J was used to estimate tumor size by measuring its length (l in mm) and width (w in mm). The tumor volume (V in mm^3) was calculated by using a formula of $V = (l \times w^2) / 2$ [29]. All the animal experimental procedures were implemented in accordance with a standard experimental setup following the Korean National Institutes of Health (KNIH) guidelines. The protocol was approved by the Institutional Animal Care and Use Committee at Pukyong National University (Permit Number: PKNUIACUC2019-30).

4.2.6 Histological analysis

To evaluate *in vivo* PTT efficacy, all the treated tumor-bearing mice were euthanized in a chamber with an overdose of CO_2 gas 14 days (D 14) after the laser irradiations with Flat and MLA. The tumor tissue samples were harvested aseptically and fixed in 10% neutral formalin solution (Sigma Aldrich, St. Louis, MO, USA) for three days. After the fixation, each sample was sectioned by 4-5 μm for slide preparation. The prepared sections were stained with standard Hematoxylin and eosin (HE) and TUNEL staining assay (TumorTACS In situ Apoptosis Detection Kit, R&D Systems Inc., MN, USA) to confirm the extent of irreversible thermal coagulation in the treated tumor tissue. All the histology slides were photographed under optical microscopy (20X for HE and 100X for TUNEL; Motic easyscan, Motic, Kowloon, Hong Kong). Then, a pathologist conducted gross examinations on the histology slides of three groups (control, Flat, and MLA; N = 4 per group) and scored the histological responses of the random spots in the slides semi-quantitatively [120, 121]: 1 (absent or minimal) represents no or minimal thermal damage in tumor tissue and negative response of TUNEL staining (blue-green color); 2 (moderate) represents mild cellular shrinkage resulting from the laser-induced injury and positive reaction of TUNEL staining (brown color); 3 (severe) represents serious thermal injury induced by the laser irradiation and positive reaction of TUNEL staining (brown color) in same area.

4.2.7 Statistical analysis

All the data were expressed as mean ± standard deviation for four independent experiments. Statistical analysis was performed using SPSS software 22 (SPSS Inc.,

Chicago, IL, USA). For nonparametric statistical analysis, the Kruskal-Wallis (KW) and Mann-Whitney U tests with Bonferroni correction (MU) were performed to compare multiple and two groups, respectively, and statistical significance was considered when $p < 0.05$.

4.3 Results

4.3.1 Temperature assessments

Numerical simulations and experimental validations were performed to estimate temperature distributions after 180-s laser irradiations with Flat and MLA (Fig. 22). Figure 22(a) presents cross-sectional temperature distributions in gelatin phantom models after 180-s irradiation with Flat (left) and MLA (right) from the simulations. Given the same irradiation condition, the Flat-based irradiation showed a narrower and shallower profile of the laser-induced temperature. On the contrary, the MLA-assisted laser irradiation entailed a deeper and wider distribution of the temperature in the simulation model. Radial distributions of the surface temperature (obtained from Fig. 22(a)) demonstrate that MLA induced a 7.1 ℃ higher peak temperature in a flatter top profile, compared to Flat (Fig. 22(b)). Axial temperature distributions (obtained from Fig. 22(a)) confirm that MLA induced a higher temperature distribution along z-axis with a higher surface temperature than Flat (Fig. 22(c)). The extent of thermal deformation in the gelatin phantom was also estimated by considering the melting point of the phantom at 35 ℃ (dashed line). According to Fig. 22(c), MLA produced 1.4-fold deeper deformation Flat (i.e, z_{Flat} = 0.8 mm vs. z_{MLA} = 1.1 mm where corresponds to 35 ℃). Figure 22(d) displays cross-sectional and top-view images of the gelatin phantoms irradiated with Flat and MLA. Compared to Flat, MLA created a deeper and wider ablation profile. The ablated phantom volumes were compared quantitatively between Flat and MLA (Fig. 22(e)). MLA ablated a five-fold larger ablation volume

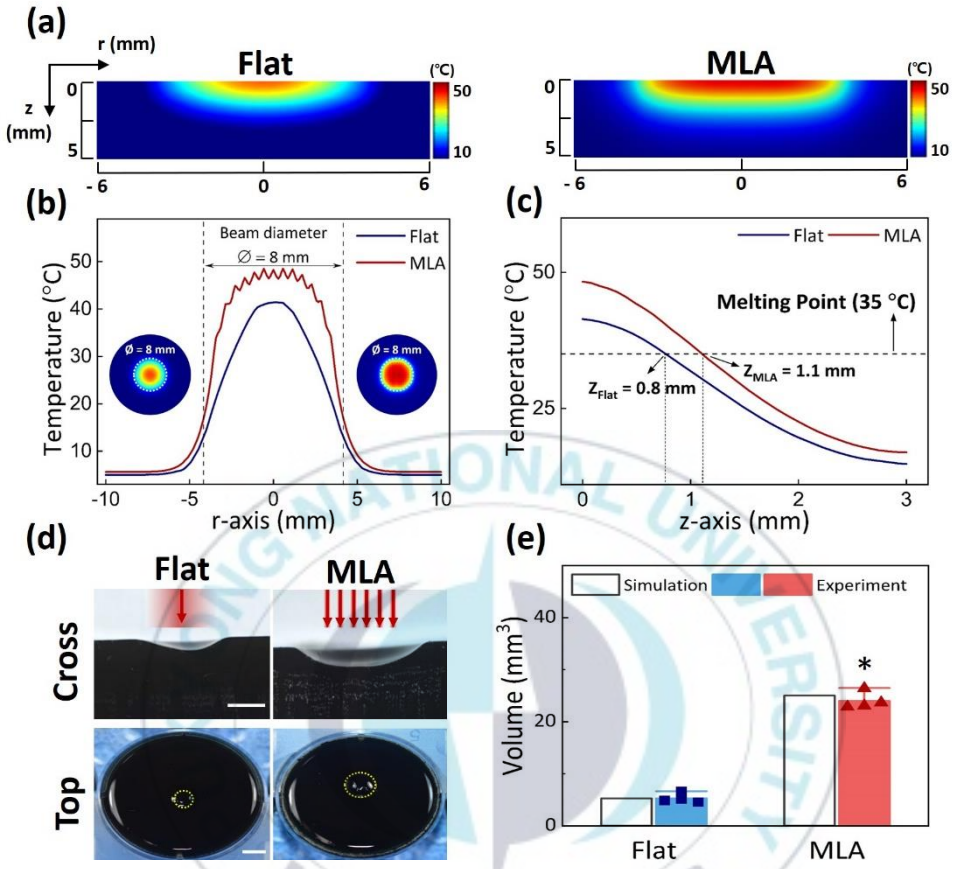

Figure 22. Comparative thermal evaluations on gelatin phantom models between flat fiber (Flat) and MLA: (a) cross-sectional (rz-plane) temperature distributions from numerical simulations, (b) temperature profiles at surface along r-axis (acquired from (a)), (c) axial temperature distributions along z-axis from center of irradiated area in (a) , (d) experimental validations in gelatin phantom models after irradiation of 1064 nm laser light with Flat and MLA (1 W/cm^2 for 15 s; 15 J/cm^2; yellow dotted lines = ablated area; scale bar = 5 mm in cross-sectional images and 2 mm in top-view images), and (e) quantitative comparison of ablated volume between Flat and MLA irradiations from simulations and experiments (N = 4; *MU $p < 0.005$ vs. Flat). Note that dashed lines in (c) represent the melting point (35 °C) of the gelatin phantom model.

than Flat (4.9 ± 1.1 mm^3 for Flat vs. 24.9 ± 2.5 mm^3 for MLA; $p < 0.05$). Both numerical simulations and experimental validations show a good agreement in the estimated volumes. deformation in the gelatin phantom was also estimated by considering the melting point of the phantom at 35 ℃ (dashed line). According to Fig. 22(c), MLA produced 1.4-fold deeper deformation Flat (i.e, z_{Flat} = 0.8 mm vs. z_{MLA} = 1.1 mm where corresponds to 35 ℃). Figure 2(d) displays cross-sectional and top-view images of the gelatin phantoms irradiated with Flat and MLA. Compared to Flat, MLA created a deeper and wider ablation profile. The ablated phantom volumes were compared quantitatively between Flat and MLA (Fig. 22(e)). MLA ablated a five-fold larger ablation volume than Flat (4.9 ± 1.1 mm^3 for Flat vs. 24.9 ± 2.5 mm^3 for MLA; $p <$ 0.05). Both numerical simulations and experimental validations show a good agreement in the estimated volumes.

4.3.2 Dosimetry tests

To identify the appropriate conditions for *in vivo* laser treatment, 1064 nm laser light with Flat and MLA was tested on IR 1061 aqueous solution at various laser irradiances and concentrations (Fig. 23). The maximum temperature increases are up to 38.5 ℃ for Flat and 44 ℃ for MLA at 3 W/cm^2 and 300 μg/ml. As the tissue temperature reaches 60 ℃, collagen and protein denaturation begin to occur, leading to irreversible thermal coagulation. Thus, considering the initial temperature of *in vivo* tissue (~37 ℃), we selected an irradiance of 2 W/cm^2 and a dye concentration of 300 μg/ml to warrant photothermal effects for the *in vivo* experiments. The temperatures at central (T_C) and

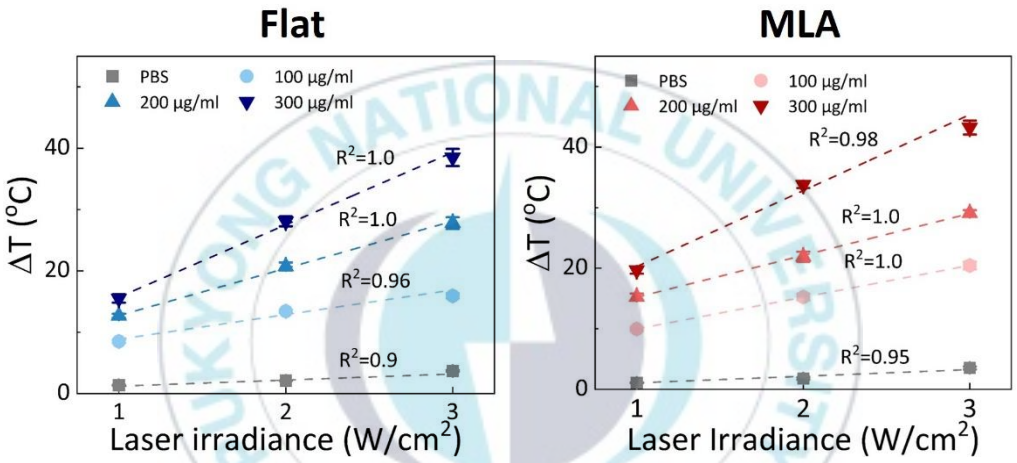

Figure 23. Comparison of temperature rises measured from PBS and IR 1061 aqueous solution with various concentrations (0 for PBS, 100, 200, and 300 µg/ml) after laser irradiation at three irradiances (1, 2, and 3 W/cm^2) for 180 s

peripheral (T_P) regions on the solution surface were measured and compared between Flat and MLA (Figs. 24(a) and (b)). Regardless of irradiation method, the temperatures (T_C and T_P) gradually increased with irradiation time, and T_C was higher than T_P due to spatial distributions of the incident laser beam. It was noted that the difference between T_C and T_P was evidently smaller in MLA (~8%) rather than in Flat (~16%) because of uniform distributions of micro-beams. At 180 s of irradiation time, MLA yielded higher T_C (56.9 ℃ for Flat vs. 62.9 ℃ for MLA) and T_P (49.4 ℃ for Flat vs. 57.9 ℃ for MLA) than Flat ($p < 0.005$; Fig. 24(c)). IR imaging confirmed rapid and wide developments of the surface temperatures during the MLA-assisted irradiation, compared to the Flat-based irradiation (Fig. 25). Figure 24(d) displays 3D temperature profiles acquired from the IR images after 180-s irradiation. MLA exhibited a relatively flat top temperature distribution than Flat with a Gaussian distribution. Similar to Fig. 21(b), radial distributions of the solution temperature confirmed that MLA accompanied around 5.2 ℃ higher temperature increase along with a 29% wider distribution, compared to Flat (Fig. 24(e)).

4.3.3 In vivo treatment

Figure 26(a) presents IR images of tumor regions treated at various times from Flat (left) and MLA (right) groups (2 W/cm^2 for 180 s; 360 J/cm^2). All the groups showed a temperature increase in the tumor during laser irradiation. At 180 s, the MLA irradiation exhibited a higher maximum temperature in a wider thermal region than the Flat irradiation. Figure 26(b) compares temporal elevations of the peak temperature at the

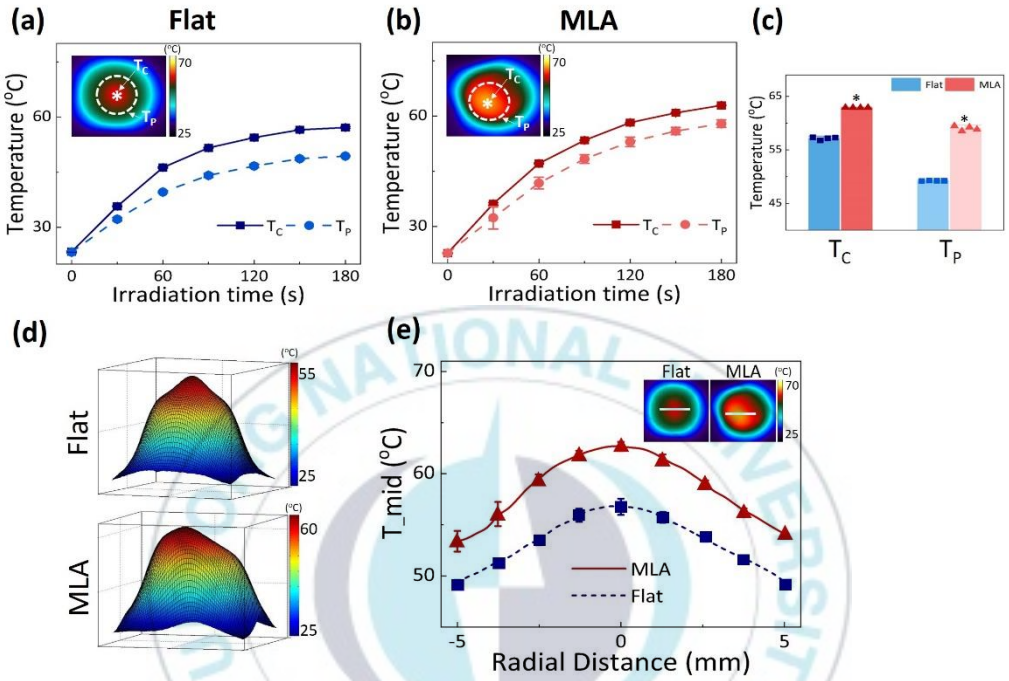

Figure 24. Comparison of photothermal effects between Flat-based and MLA-assisted irradiations at 2 W/cm^2 on IR 1601 aqueous solution (300 μg/ml in PBS): temporal developments of surface temperature at central (T_C; measured at r = 0 mm; white asterisk) and peripheral (T_P; measured at r = 4 mm; white dashed line) regions obtained from (a) Flat and (b) MLA, (c) comparison of elevated temperatures at T_C and T_P after 180-s irradiation, (d) 3D images of temperature fields after 180-s irradiation (360 J/cm^2), and (e) comparison of radial temperature distributions along middle line ($T_{\_mid}$) of IR images after 180-s irradiation. Note that the inlets in (a), (b), and (e) represent the captured IR images after 180-s irradiation (N = 4; *MU $p < 0.005$ vs. Flat).

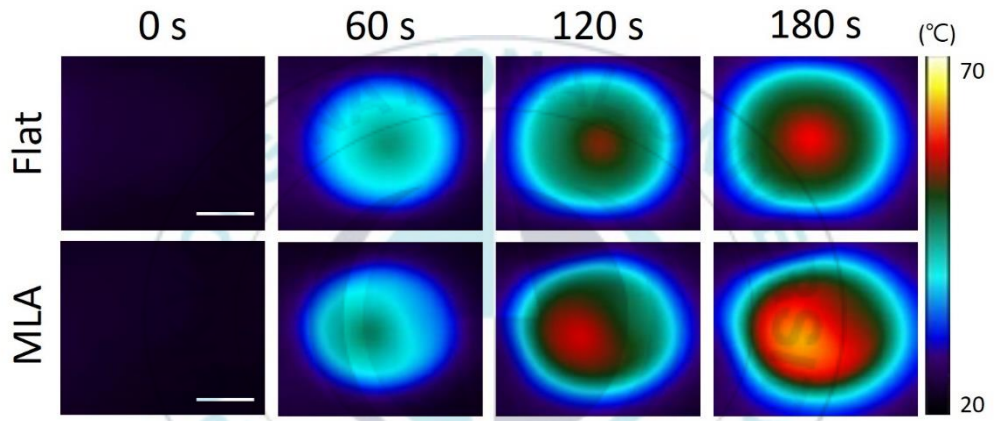

Figure 25. Infrared thermographic compilations of laser irradiation on IR 1061 solution with Flat and MLA for 180 s (scale bar = 3 mm)

tumor surface. Both Flat and MLA irradiations demonstrated that the tumor temperature initially increased with the irradiation time but became saturated around 60 s after the irradiation. At the end of the irradiation, MLA reached a higher maximum temperature than Flat (55.2 ℃ for Flat vs. 62.4 ℃ for MLA; $p < 0.005$). The treated regions with a temperature of 50 ℃ or higher were also compared between the two groups at various times (Fig. 26(c)). Regardless of irradiation time, MLA created around 1.5-fold larger regions than Flat, implicating a wider temperature distribution because of uniform delivery of micro-beams (i.e., 22.2±3.1 mm^2 for Flat vs. 33.1±2.2 mm^2 for MLA at 180 s; $p < 0.005$).

All treated tumors were monitored for 14 days to characterize treatment efficacy of Flat and MLA irradiations (Fig. 27). According to Fig. 27(a), tumor size from control (no treatment) slightly increased for three days after the treatment but showed a significant growth afterwards. The Flat group maintained the tumor size for seven days, but the tumor rapidly increased with scab on the treated surface. On the contrary, the MLA group accompanied a slightly larger treated lesion (D 0), and the tumor size noticeably decreased over time. Figure 27(b) compares the quantified tumor volumes at various times among the three groups. Evidently, the MLA group exhibited a continuous reduction in the tumor size with the healing time, unlike the control and Flat groups. At D 14, the tumor from the MLA group was almost eradicated ($p < 0.005$ vs. control and Flat; Fig. 27(c)). Figure 27(d) presents histological images of the treated tumor tissue at D 14 to validate antitumor effects of Flat and MLA. The control group showed no significant disorganization of the tumor tissues and no morphological

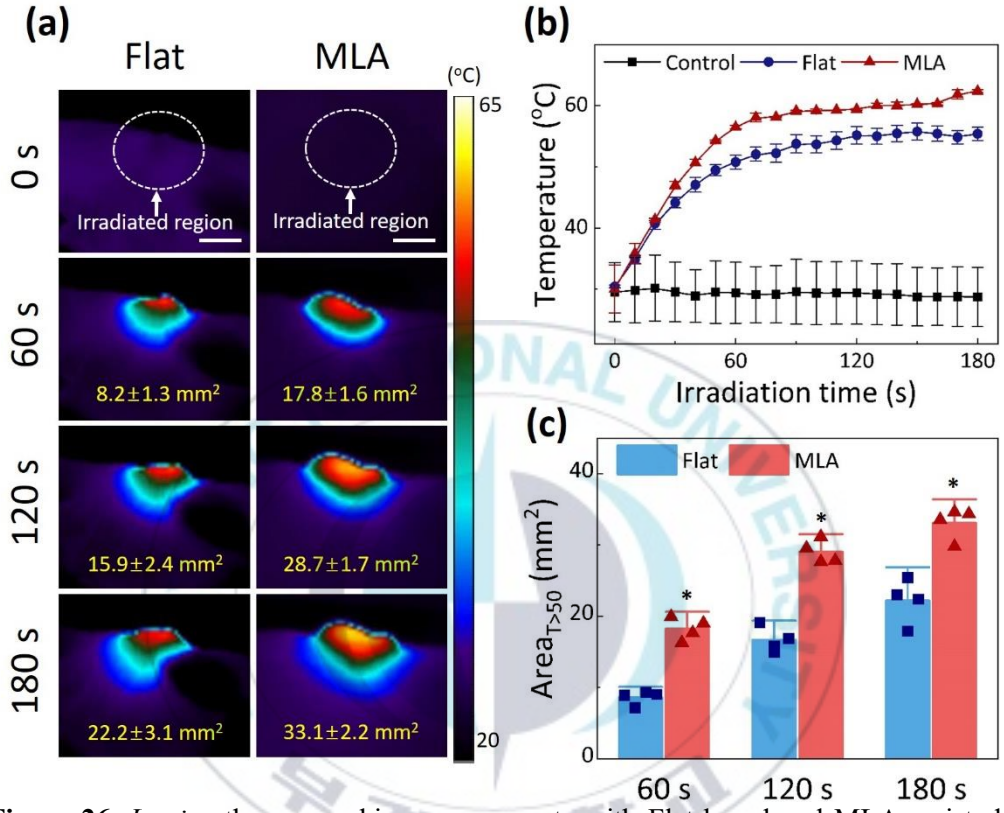

Figure 26. *In vivo* thermographic measurements with Flat-based and MLA-assisted irradiations at 2 W/cm^2 for 180 s (dye concentration = 300 μg/ml in PBS): (a) IR images of CT26 tumor-bearing mouse model captured at various irradiation times, (b) temporal developments of maximum temperature measured from irradiated area in tumor (white dashed lines in (a)), and (c) comparison of treatment areas with temperature of 50 °C or higher (T > 50) at three irradiation times (N = 4 per group; scale bar = 5 mm; *MU $p < 0.005$ vs. Flat).

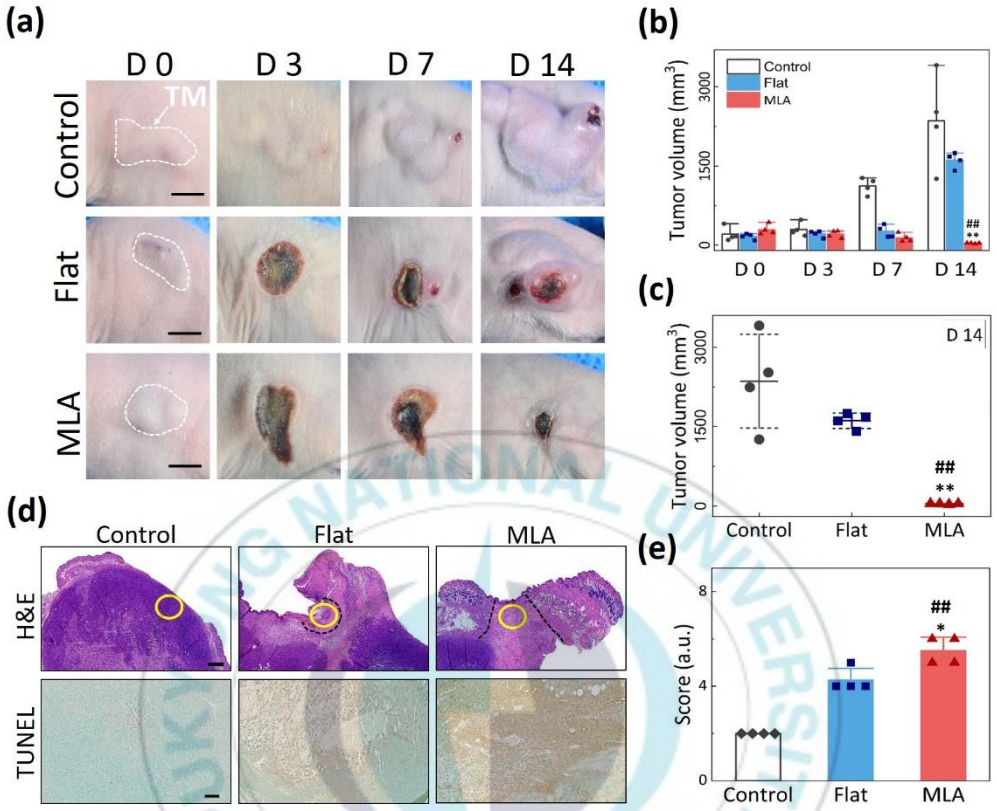

Figure 27. *In vivo* photothermal treatment of CT 26 tumor-bearing mouse models with Flat-based and MLA-assisted irradiations at 2 W/cm^2 for 180 s (dye concentration = 300 μg/ml in PBS): (a) compilation of images of tumor model at various time points after laser irradiation (TM = tumor region; scale bar = 5 mm), (b) comparison of tumor growth after laser treatment, (c) statistical comparison of tumor volumes at D 14, (d) HE-stained (top row; 20X; scale bar = 600 μm) and TUNEL-stained (bottom row; 100X; scale bar = 50 μm) images of treated tumor cross-sections at D 14, and (e) semi-quantitative evaluations of histopathological responses from treated tumor tissue. Note that black dashed and yellow solid lines in (d) represent the laser-treated area and the observed area for TUNEL analysis, respectively (N = 4 per group; KW $p < 0.01$; $^{\#\#}$MU $p < 0.005$ vs. control; **MU $p < 0.005$ and *MU $p < 0.05$ vs. Flat)

changes in the tumor cells. Conversely, the tumor tissues treated with Flat and MLA presented distinct cellular death in the irradiated regions as a result of photothermal effects (top row). According to TUNEL staining (bottom row), the Flat and MLA groups demonstrated apoptotic cell death in the treated lesions. However, it was noted that the Flat group was associated with smaller areas of irreversible thermal damage, leading to regeneration of the tumor tissue even in the treated area. As a result, the overgrowth of the tumor caused tumor hypoxia during the healing period (Fig. 27(a)). Based on the pathologic scoring, the MLA group entailed more significant histological responses (severe thermal injury and positive reaction of TUNEL staining) than the control ($p < 0.005$) and Flat groups ($p < 0.05$; Fig. 27(e)).

4.4 Discussion and conclusion

Ablative fractional laser (AFL) treatment has widely been studied for skin cancer treatment by removing the entire epidermis in the targeted area [122, 123]. A number of previous AFL studies reported the feasible inhibition of tumor growth at early stage of cancer or dysplasia [124, 125]. However, the AFL treatment is often limited to the mere removal of epidermis, which is unable to reach deeply or widely positioned tumor tissue [115]. Therefore, spatially-enhanced distributions of optical energy during laser treatment is pivotal in attaining complete tumor inhibition and suppression of tumor recurrence. The current study verified the feasibility of MLA-assisted PTT with collective microthermal effects on tumor numerically and experimentally, in comparison to Flat-based PTT. Given the same irradiation conditions, MLA produced a deeper and wider temperature development than Flat, indicating that MLA can develop high-irradiance micro-beams during the irradiation [114]. In fact, the applied irradiance of each MLA-induced micro-beam was 72 mW/mm^2 (72 mW/mm^2 = 2 W/ [145 micro-beams and 96-μm^2 micro-beam area]), whereas the irradiance of Flat-induced macro-beam was 20 mW/mm^2 (2 W/50.24 mm^2 macro-beam area). Thus, as applying the collective thermal effects from a higher density of the micro-beams during the treatment (Figs. 22 and 24), the MLA-assisted irradiation widely generated irreversible thermal damage in the entire tumor tissue (Fig. 27). On the other hand, on account of a Gaussian-shaped beam profile, distributions of Flat-induced temperature became centric, which resulted in non-uniform and narrow treatment in the tumor (Figs.

22 and 24; [36]). Therefore, the MLA-enhanced PTT can provide a therapeutic capacity of developing a more uniform and wider distribution of thermal energy after delivery of the micro-beams at high fluences for fractional cancer treatment.

Flat group demonstrated that seven days after PTT, tumor volume started to increase dramatically, and at D 14, tumor necrosis occurred evidently on the tumor surface (Flat) due to abnormal and uncontrollable regrowth (Fig. 27(c)). Incomplete tumor treatment with non-uniform beam distributions from Flat can be responsible for stimulation of tumor growth and generation of the eventual necrosis [36]. Recently, a number of studies have reported rapid cancer cell proliferation and tumor growth as a result of laser stimulation [126, 127]. Bamps et al. tested an 830-nm laser wavelength on head and neck squamous cell carcinoma and found the cell proliferation with upregulations of phosphor-protein kinase B (akt), phosphor-ERK, and Ki67 markers, evidencing the facilitated cancer aggressiveness [128]. Various studies also presented that photo-biomodulation with low laser light could proliferate cancer cells, including anaplastic thyroid cancer, oral carcinoma, and cervical cancer [129-131]. In addition, as the tumor grows excessively, tumor hypoxia can occur due to lack of oxygen and insufficient blood supply [132]. The abnormal and rapid proliferation of the tumor can easily outgrow from marginal vasculature, which drops an oxygen level to less than 2%; consequentially, the occurrence of the tumor hypoxia can lead to tumor necrosis [132, 133]. Therefore, the marginal cancer cells after laser treatment can undergo photo-biomodulative stimulations and eventually increase cell proliferation and cancer aggressiveness. Hence, to warrant treatment safety, adverse effects of PTT should be

validated with a wide range of laser parameters (irradiance, irradiation time, and beam spot size) in *in vivo* cancer models in terms of cell proliferation, extent of complete tumor removal, and correlation with tumor regrowth.

Although MLA yielded more uniform and wider distributions of temperature on tumor than Flat, the micro-beams emitted from MLA were still distributed in a Gaussian profile due to inherent optical nature (Fig. 24). In turn, the uneven distribution of different micro-beam energy levels may lead to incomplete eradication of peripheral regions particularly in a large sized tumor. In order to have a more flat-top beam distribution consisting of comparable micro-beam energy on the tumor surface, diffractive optical elements (DOE) can be employed as an alternative to MLA for effective PTT. Unlike MLA with the Gaussian profile, DOE can yield flat-top distributions of the micro-beams by means of a homogenization process that overlaps diffraction patterns [134]. Although energy loss (~20%) occurs during the homogenization process, DOE is hardly affected by fluctuations in the applied laser power and thus can deliver more uniformly stable micro-beams to the target than MLA. Therefore, further investigations will examine the feasibility of DOE-assisted PTT for effective cancer treatment in comparison to the current findings.

The current study used murine colon cancer cells (CT26) to perform preclinical validations of MLA-assisted PTT on tumor. Rapid growth and rich blood supply of the CT26 cells in an *in vivo* xenograft model can emulate pathological characteristics of human colon carcinoma [106, 135]. Further studies will examine various cancer cells, such as breast cancer, liver cancer, and pancreas cancer, to validate

a therapeutic capacity of the MLA-assisted PTT on metastatic cancer and to confirm acute and chronic responses of wound healing in the treated lesions. In addition, the current study selected a wavelength of 1064 nm and IR1061 dye to facilitate photothermal effects during laser irradiation. For clinical translations, treatment conditions for MLA-assisted laser irradiation should be further optimized with various laser wavelengths (ultraviolet, visible, and infrared) and photothermal agents (IR 788 dye, chlorin e6, and gold nanoparticle) to warrant the efficacy and safety of the MLA-assisted PTT on tumor [17]. Additionally, the present study merely used IR1061 dye as an absorbing agent for tissue phantom. Therefore, a tissue-mimicking phantom mixed with both absorbing and scattering agents should be tested to elucidate the distribution of optical fluence [136].

The current study demonstrates the feasibility of MLA-assisted PTT on effective treatment of colon cancer *in vivo*. Collective photothermal effects from MLA-induced micro-beams account for a spatial enhancement of thermal damage in the irradiated tumor as well as complete tumor treatment without recurrence. Future studies are expected to investigate the proposed therapeutic capacity with various wavelengths and photothermal agents to further warrant efficacy and safety of MLA-assisted PTT on cancer for clinical translations.

Chapter 5. Gold nanorods-assisted photothermal therapy on cancer with temporal power modulation

5.1. Introduction

Photothermal therapy (PTT) has drawn a great attention as a minimally-invasive or non-invasive method that involves the physical interactions between laser light and natural/synthetic chromophores to destruct cancer cells through direct and selective thermal decomposition [18]. As a promising treatment modality in oncology, a great interest in designing the synthetic photo-absorbing agents has been arising to pursue successful PTT outcomes for potential clinical applications. For instance, gold nanoparticles (GNPs) has been widely employed as a novel photothermal agent because of its stability, good surface modification, and rapid heat conversion of light [137]. Gold nanorods (GNRs), which is one of the specific types of GNPs, have been applied to deeply-located tumors owing to the absorbance peaks of surface plasmon resonance (SPR) that can allow a deep energy penetration [138]. In addition, functionalized nanomaterials, such as carbon-based and organic nanoparticles, have been continuously investigated in terms of low toxicity and good solubility [30, 77]. Nonetheless, since cancer protects itself from hyperthermia, high temperature over 50 ℃ is essential for complete ablation to induce cell necrosis. Otherwise, low temperature (41-45 ℃) used for hyperthermia induces recoverable cell damage with help from heat shock proteins

as well as incomplete cancer cell destruction, leading to tumor recurrence [18]. Although GNPs-assisted PTT typically induces temperature of over 50 ℃ to completely ablate the whole tumor tissue, such temperature ablation often accompanies unfavorable thermal damage to the surrounding healthy tissue, eventually delaying wound healing and causing post-treatment complications [25]. Hence, the alternative treatment strategy with minimal injury is still needed to overcome the limitations of conventional PTT.

A number of studies have demonstrated several approaches to monitor temperature in real-time and to control the extent of thermal damage in a target tissue to compensate limitations of PTT. Van Nam Tran et al. reported a linear energy modulation model to reach and maintain the predetermined range temperature [139]. The energy modulation established a linear correlation between coagulation volume and irradiation time, which could allow the extent of thermal coagulation in tissue to be predictable. Norio Daikuzono et al. employed a temperature feedback system for laserthermia, which could control the temperature of local hyperthermia (e.g., 42 ℃) during a prolonged period of time (20-40 min) [140]. Kjell Ivarsson et al. regulated temperature (~50 ℃) by using power modulation with a feedback thermistor during irradiation of 805 nm laser light [141]. However, most temperature control techniques were applied to treat non-cancerous tissues merely with laser light.

The current study aims to improve the efficacy of selective PTT on CRC in *in vivo* tumor models by temporally modulating laser energy during GNR-assisted PTT on cancer. We hypothesized that temporal modulation of light energy during laser

irradiation could develop a constant photothermal temperature in tumor tissue for the complete tumor eradication as well as minimal thermal injury to the surrounding healthy tissue. GNRs were employed as a photothermal agent to absorb the modulated laser energy and to attain the photothermal temperature in the cancer cells. The proposed modulation method was evaluated in aqueous GNR solutions and *in vivo* models to confirm the feasibility of clinical translation. Histological analysis explored the extent of thermal damage in the tumor tissue to validate the efficacy and safety of the proposed treatment.

5.2 Materials and methods

5.2.1 Gold nanorods

PEGylated gold nanorods (PEG-GNRs; aspect ratio = 6.7; diameter = 10 nm; length = 67 nm; surface plasmon resonance peak = 1055 nm) were obtained from Nanopartz. A Zeta Potential value of GNRs in PBS was measured to be -35 mV. To characterize GNRs for qualitative and quantitative evaluations, transmission electron microscopy (TEM) images and UV-VIS-NIR absorption spectra were taken through JEM-2100F and spectrophotometer (V-670, JASCO), respectively.

5.2.2 Aqueous solution experiments

A 1064 nm laser system (FC-W-1064B-30W, CNI, Changchun, China) was employed for the current PTT testing because of its deep optical penetration (up to 10 mm). The laser light was delivered through a multimode end-firing flat fiber (core diameter = 600 μm; NA = 0.22; Thorlabs Inc., Newton, New Jersey, USA) to each sample. The beam spot size on the sample surface was 0.8 cm^2. Before and after each irradiation test, a photodiode sensor (PD-300-3W, Ophir, Jerusalem, Israel) in conjunction with a power meter (Nova II, Ophir, Jerusalem, Israel) was used to measure the output laser power in order to maintain the identical experiment conditions and to minimize any experimental errors. The output laser power ranged from 1.2 W to 2.4 W, and its corresponding irradiance ranged from 1.0 W/cm^2 to 3.0 W/cm^2.

To identify experimental conditions, the photothermal properties of GNRs were confirmed at various fixed power densities (1, 1.5, 2, 2.5, and 3 W/cm^2; irradiation time = 180 s) and modulated power densities. For the power modulation, 3 W/cm^2 was firstly irradiated for 60 s, followed by the irradiation of 1, 1.5, 2, and 2.5 W/cm^2 for 120 s, respectively. A constant concentration of GNRs in PBS (25 μg/ml) was put into a 96-well culture plate (volume of each well = 100 μl). Then, 1064 nm laser light was irradiated perpendicularly on each well. A real-time infrared (IR) camera (A325, FLIR, Wilsonville, Oregon, USA) was used to record a spatio-temporal temperature distribution on the solution surface during the laser irradiation. Each test was repeated three times (N = 3).

5.2.3 *In vivo* testing

CT26 murine colon cancer cells were purchased from Korean Cell Line Bank and cultured in Dulbecco's modified Eagle's Medium (DMEM, Corning, NY) supplemented with 10% fetal bovine serum (FBS, Corning, NY) and 1% antibiotic-antimycotic (Gibco, Grand Island, NY). The cultured cells were placed in a humidified incubator at 37 ℃ with 5% CO_2 atmosphere. A total of 16 balb/c female mice (five weeks old, 20-25 g weight) were procured from Hana Biotech (Suwon, Republic of Korea) to fabricate tumor models. All the mice were housed in a pathogen-free facility and acclimated for a week under standard conditions. Then, tumor-bearing mice were prepared by inoculating the suspension of CT26 cells (1.5X10^5 cells) into the back of

each mouse and allowing the cells to grow for a week. When the tumors reached a volume of 150 mm^3, each mouse was randomly divided into four groups and tested under four different irradiation conditions: control (no irradiation), 1.5 W/cm^2 for 180 s, 3 W/cm^2 for 90 s, and modulated (MD) irradiations (3 W/cm^2 for 60 s followed by 1.5 W/cm^2 for 60 s; N = 4 per group). The irradiation conditions were determined by dosimetry studies using GNR solutions aforementioned. The irradiation conditions delivered the same laser fluence (270 J/cm^2) to tumor tissue to achieve photothermal interaction for irreversible coagulation in the tissue. All the mice were intratumorally injected with diluted GNRs (100 µl, concentration = 25 µg/ml in PBS) through a 26-gauge needle. After two hours of incubation, 1064-nm laser light was irradiated on the tumor-bearing mice with each treatment condition. A real-time IR camera was used to record the temperature elevations in the tumor sites. All the animal experiments were performed under the complete anesthesia by using a respiratory anesthesia system (Classic T3, SurgiVet, USA) with 3% isoflurane (Terrell™ isoflurane, Piramal Care, Bethlehem, PA, USA) in oxygen (0.6 L/min). Each treated tumor was monitored and photographed by using a digital camera (D5100, Nikon, Tokyo, Japan) at four different time points: 0 (D 0), 3 (D 3), 7 (D 7), and 10 (D 10) days after PTT. Image J (National Institute of Health, Bethesda, MD) was used to measure the length (l) and the width (w) of each tumor. Tumor volume (v in mm^3) was then estimated by calculating the equation, $v = (l \times w^2)/2$ [29]. The animal experiments were approved by the Institutional Animal Care and Use Committee at Pukyong National University (Permit number: PKNUIACUC-2021-04) in compliance with the regulations concerning experimental

animals.

5.2.4 Histological analysis

Ten days after GNR-assisted PTT, all the tested tumor samples were extracted from animals and fixed in 10% neutral formalin solution for further histological analysis. The fixed tissues were processed into paraffin and sectioned by 4-5 μm. Hematoxylin and eosin (HE) staining was carried out to evaluate photothermal effects on the tumor sites. All the stained slides were scanned under optical microscopy (Motic Easyscan, Motic, Kowloon, Hong Kong) and evaluated by a pathologist.

5.2.5 Statistical analysis

The data were presented as mean ± standard deviation, and each value represented the mean of the results of at least four independent experiments in each group. As non-parametric statistical analysis, the Kruskal-Wallis (KW) and Mann-Whitney U tests with Bonferroni correction (MU) were conducted by using SPSS software 22 (SPSS Inc., Chicago, IL, USA) to assess the statistical significance of the difference between multiple and two groups, respectively. $p < 0.05$ was considered as statistical significance.

5.3 Results

5.3.1 Photothermal effects of PEG-GNRs

Figure 28 characterizes PEG-GNRs in terms of physical dimension and absorption spectrum. A TEM image confirms that PEG-GNRs were uniformly elongated (~100 nm long; Fig. 28(a)). Figure 28(b) demonstrates the absorbance spectra of PEG-GNRs at various concentrations in aqueous solutions. Regardless of concentration, strong light absorption occurred at around 990 nm, confirming that the application of the current wavelength (1064 nm) is appropriate for PTT. To assess photothermal capacity, 1064 nm laser light was irradiated on the aqueous dispersions with various concentrations at 1.5 W/cm^2 for 180 s (Fig. 28(c)). The concentration of 20 μg/ml merely induced a temperature increase of only 5.5 ℃. In contrast, the concentration of 30 μg/ml yielded the maximum temperature rise of up to 8.4 ℃. As the target photothermal temperature is around 45 ℃, the temperature increase in the aqueous dispersion should be around 7 ℃. Thus, the concentration of 25 μg/ml was selected for the rest of testing because of the temperature increase of 6.4 ℃.

5.3.2 Dosimetry tests of PEG-GNRs

To determine the proper conditions of *in vivo* PTT, 1064 nm laser was irradiated on the aqueous PEG-GNR solution (concentration = 25 μg/ml in PBS) at various irradiation conditions (Figure 29). In consideration of the initial temperature in *in vivo* models

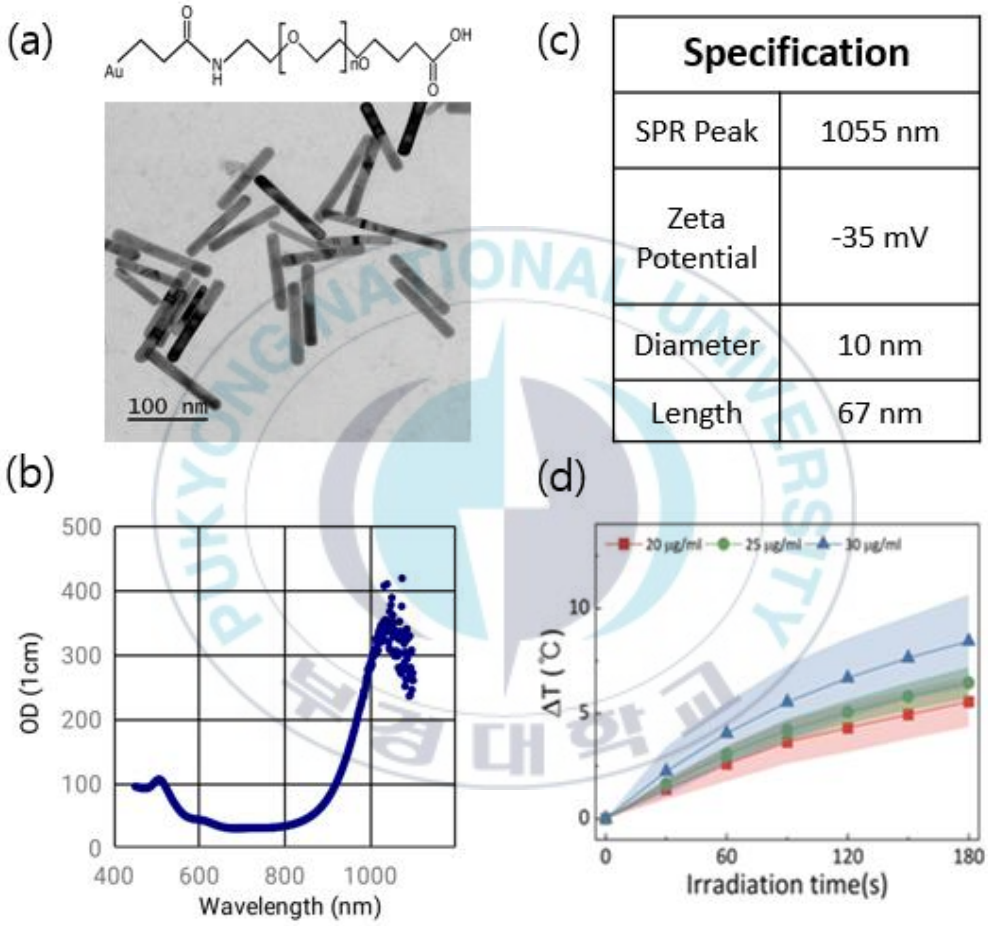

Figure 28. Characteristics of PEG-GNR: (a) TEM image and chemical structure, (b) absorption spectrum, (c) specification of PEG-GNR, and (d) temperature elevation of PEG-GNRs at various concentrations (20, 25, 30 μg/ml)

(body temperature = 37 °C), a temperature elevation of 15 °C can be sufficient to induce photothermal effects in tumor tissue. Regardless of fixed power density, the temperature elevation increased with irradiation time (Fig. 29(a)). The highest power density (3 W/cm^2) entailed the maximum temperature elevation of 23 °C. It was noted that the power densities of 2.5 and 3 W/cm^2 reached the temperature elevation of 15 °C in 120 s and 60 s, respectively. Figure 29(b) presents the effect of modulated (MD) irradiations on the temperature elevations in the PEG-GNRs solution. For the MD irradiations, the power density of 3 W/cm^2 was initially irradiated for 60 s to reach the temperature elevation of 15 °C. Then, various power densities (1, 1.5, 2, and 2.5 W/cm^2) were irradiated for 120 s, respectively. Except 1 W/cm^2, the secondary power densities maintained the temperature elevation of 15 °C (Fig. 29(b)). Based on the results in Fig. 29(b), the MD conditions was selected as 3 W/cm^2 for 60 s followed by 1.5 W/cm^2 for 120 s in order to entail photothermal effects on tumor tissue. Figure 29(c) presents a compilation of the IR images of the temperature developments with various irradiation conditions (1.5 W/cm^2, 3 W/cm^2, and MD for 180 s, respectively) in the PEG-GNRs aqueous solution captured at four different times. Regardless of irradiation condition, the temperature increased with irradiation time. 3 W/cm^2 continuously increased the temperature and yielded the maximum temperature of 54 °C at 180 s. On the other hand, MD reached the temperature of 45 °C in 60 s and maintained the temperature along with a uniform temperature distribution for another 120 s. Figure 29(d) demonstrates the temperature elevations of three irradiation conditions as a function of irradiation

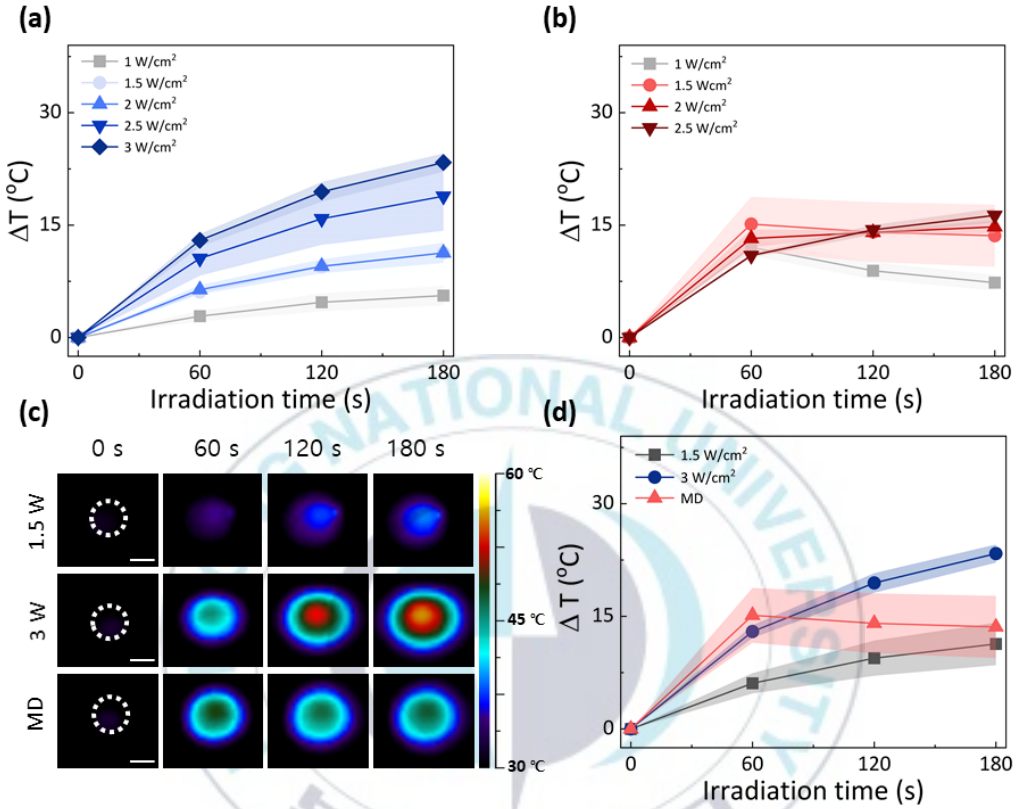

Figure 29. Photothermal profile of PEG-GNRs in aqueous solution (concentration = 25 μg/ml in PBS) under 1064 nm laser irradiation: temperature elevations (ΔT in ℃) as function of (a) fixed power density (1, 1.5, 2, 2.5 and 3 W/cm^2) and (b) modulated power density (3 W/cm^2 for 60 s followed by 1, 1.5, 2 and 2.5 W/cm^2 for 120 s, respectively), (c) IR thermal images of temperature developments in PEG-GNRs aqueous solution at four different time points (white dotted line = irradiated area; scale bar = 4 mm; N = 4) and (d) comparison of temperature elevations between fixed (1.5 W/cm^2 and 3 W/cm^2 for 180 s, respectively) and modulated irradiations (MD; 3 W/cm^2 for 60 s followed by 1.5 W/cm^2 for 120 s). Note that the colored areas in (a), (b) and (d) represent standard deviations.

time. Similar to Fig. 29(c). the power density of 3 W/cm^2 continuously increased the temperature elevation (up to 23 ℃) whereas MD reached the temperature elevation of 15 ℃ in 60 s and almost maintained the same temperature elevation for 120 s with a deviation of 92 %.

5.3.3 *In vivo* PTT with power modulation

Figure 30(a) presents IR images of temperature developments of PEG-GNRs-injected tumor tissue in *in vivo* models with three different irradiation conditions (1.5 W/cm^2, 3 W/cm^2, and MD). All the groups received the same laser fluence (270 J/cm^2) as the irradiation times were adjusted (i.e., 1.5 W/cm^2 for 180 s, 3 W/cm^2 for 90 s, and MD for 120 s). For MD, 3 W/cm^2 was initially irradiated for 60 s and then, the lower power density of 1.5 W/cm^2 was irradiated for 60 s. The irradiation of 3 W/cm^2 demonstrated that the surface tissue temperature increased with the irradiation time and the temperature distribution was expanded with the time. On the other hand, the MD irradiation presented that the surface tissue temperature and its distribution were consistently maintained for 40 s after the irradiation started. Figure 30(b) shows the temporal developments of the surface tissue temperature for the three irradiation conditions. 1.5 W/cm^2 slowly increased the surface temperature with the irradiation time and reached 49 ℃ at 180 s. 3 W/cm^2 rapidly and continuously increased the tissue temperature up to 59 ℃ in 90 s. On the other hand, MD initially entailed the temperature of 54 ℃ in 60 s, and the surface temperature slowly decreased down to

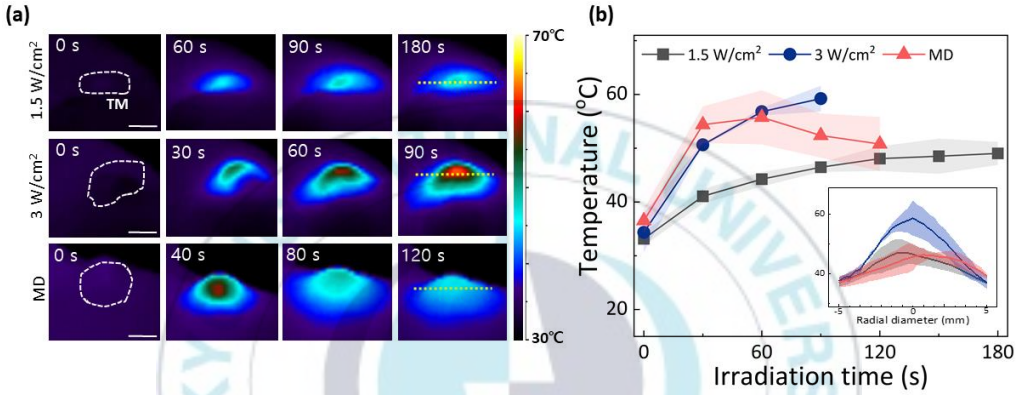

Figure 30. Temperature development of PEG-GNRs-injected mice with different irradiation methods: (a) IR thermal images of irradiated tumors at four different time points (TM = tumor region; N = 4; scale bar = 6 mm) and, (b) comparison of temperature elevations between continuous (1.5 W/cm^2 and 3 W/cm^2) and modulated irradiations (MD; 3 W/cm^2 for 60 s and 1.5 W/cm^2 for 60 s). An inlet in (b) shows the radial profiles of the temperature acquired from the yellow botted lines in (a). Note that the colored areas in (b) represent a standard deviation.

52 ℃ for 60 s. The inlet in Fig. 30(b) demonstrates the cross-sectional temperature profiles acquired from Fig. 30(a) (yellow dotted lines at 180 s). 3 W/cm^2 exhibited a Gaussian temperature profile (47.6 ± 7.4 ℃) with the maximum temperature in the middle whereas MD created a uniform temperature distribution (42.5 ± 2.9 ℃) over the entire tumor region.

After PTT, all the tested tumor tissues were monitored for ten days to compare treatment efficacy (Figure 31). According to Fig. 31(a), the tumor volumes from control and 1.5 W/cm^2 increased noticeably with time. In the case of 3 W/cm^2, the tumor volume was initially maintained for three days but started to increase afterwards. On the other hand, the tumor volume from MD was maintained for seven days, and a slight increase in the tumor volume was observed. It was noted that the largest necrotic lesion was found at D 3 in the middle of the tumor from MD. However, the lesion became reduced gradually with time (bottom; Fig. 31(a)). Figure 31(b) confirms no variations in the body weights of all the groups for the ten days. Figure 31(c) compares the relative tumor growth at various times post-PTT. The control group showed considerable increases in the relative tumor growth with time (up to 20-fold at D 10). On the other hand, the MD group exhibited slight changes in the relative tumor growth ($p < 0.05$ vs. control at D 10). To validate a therapeutic capacity of power-modulated PTT against tumor tissue, histological analysis was conducted (Fig. 32). Figure 32(a) presents HE-stained images of the tumor tissues at D 10. The right columns (200X) were magnified from yellow boxes in the left column images (15X). The control group showed no morphological changes in the tumor tissue. In contrast, all the laser-treated groups

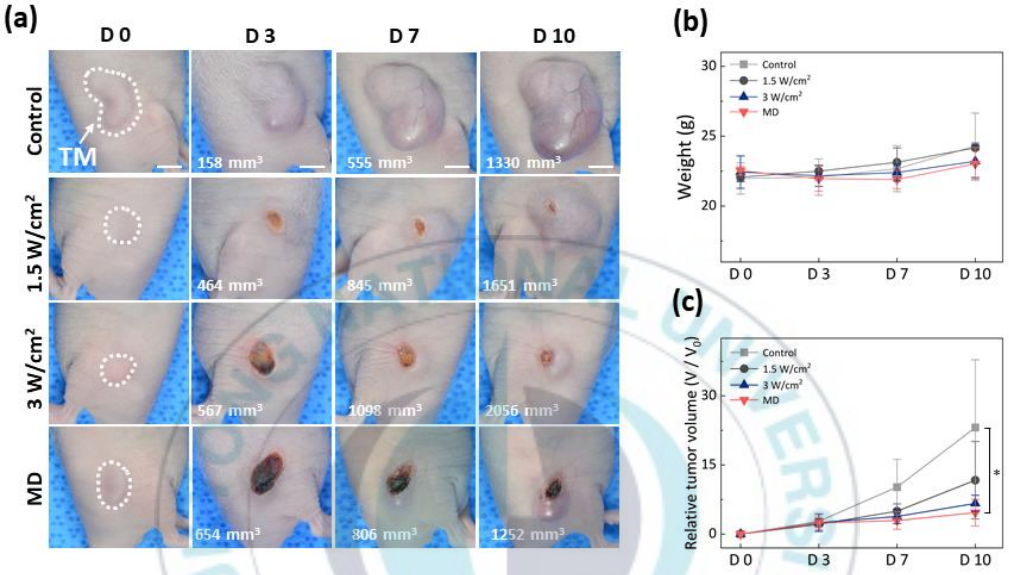

Figure 31. *In vivo* photothermal therapy of CT26-tumor-bearing mice models after laser treatment under various conditions. (a) representative photographs of CT26-tumor-bearing mice after laser treatment. (TM = tumor region; scale bar = 5 mm; N = 3) and (b) body weight variations, and (c) relative tumor growth (N=4; KW $p < 0.05$; * MU $p < 0.05$ vs. control). Note that the numbers in (a) represent the volume of cancer.

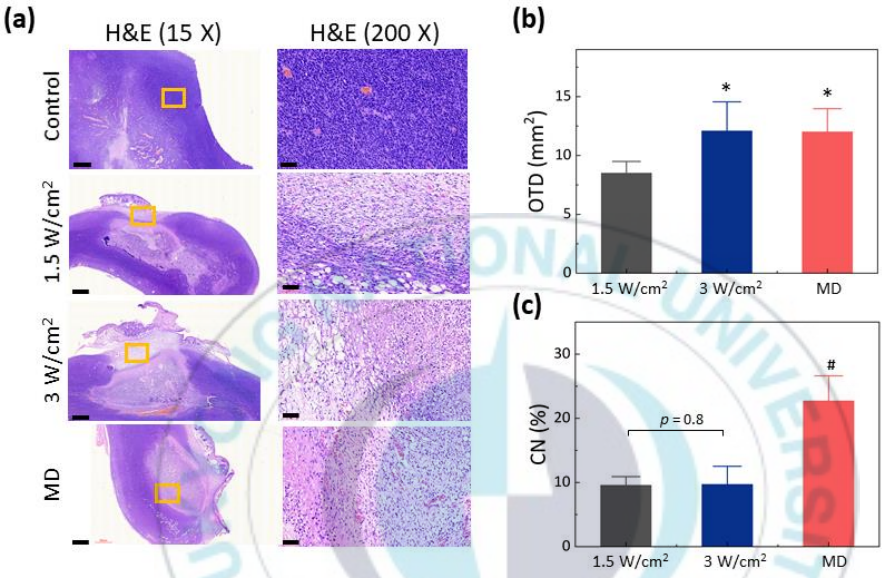

Figure 32. Comparison of photothermal treatment effects on *in vivo* models after irradiations with various conditions: (a) HE-stained images of tumor regions (15 X and 200 X; scale bar = 800 μm and 60 μm, respectively), (b) area of overall thermal damage (OTD; KW $p < 0.05$; * MU $p < 0.05$ vs. 1.5 W/cm^2), and (c) ration of coagulative necrosis (CN) area to OTD (N=4; KW $p < 0.05$ $^{\#}$ MU $p < 0.05$ vs 3 W/cm^2). Note that the yellow boxes in (a) are magnified on the right side (200 X).

exhibited the regions of cellular damage in the tissue, including cell pyknosis, unclear pyknosis with heavy staining, and endothelial disruption [142]. Figure 32(b) compares the area of overall thermal damage (OTD in mm^2) in the tumor tissues. Both 3 W/cm^2 and MD yielded around 50% larger OTD than 1.5 W/cm^2 (MD = 12 mm^2 vs. 1.5 W/cm^2 = 8 mm^2; $p < 0.05$). The ratio of coagulative necrosis area (CN) to OTD was estimated by dividing CN by OTD (Fig. 32(c)). The MD group was associated with the largest CN (up to 23%), compared to 1.5 W/cm^2 (up to 10%) and 3 W/cm^2 (up to 10%; $p < 0.05$), indicating that the power modulation enhanced tumor necrosis. Compared overall thermal damage with continuous power density, modulation showed almost same area with 3 W/cm^2, however modulation induced extremely high coagulative necrosis which is involved to demonstrate ablation of cancer through photothermal heating. As a result, Figure 32 verified the therapeutic effect of the power modulation by quantifying coagulation necrosis region of tumor which compared with continuous power density (1.5 W/cm^2 and 3 W/cm^2).

5.4 Discussion and conclusion

A number of studies have reported feedback techniques to control tissue temperature during laser irradiation. Van Nam Tran et al. maintained the high tissue temperature (70 °C) to ensure effective thermal coagulation by using high output power with short irradiation time [139]. At result, coagulative necrosis derived about more twice at regulation temperature group compared with control group which continuously increase temperature. To effective thermal coagulation, Duc Tri Phan et al. us artificial neural network for automated system to maintain the high temperature (80 °C) at tissue [143]. While short irradiation time, high intensity induced severe carbonization in tissue at continuous increased temperature. On the other hand, moderate temperature regulation has no severe thermal carbonization of heat damage with stable therapeutic effects. Therefore, the current study experimentally confirmed the therapeutic effect of PTT with the power modulation on CRC, compared to the conventional PTT with the constant power application. The gradual power modulation with respect to time could maintain a constant temperature in the tissue (50~55 °C), eventually maximizing CN and minimizing thermal injury. Although the current study demonstrated the power modulation method to regulate tissue temperature for effective PTT, several limitations still remain prior to clinical applications.

Basically, the end-firing flat fiber is usually utilized for conventional PTT to deliver laser light on tumor tissue. Owing to a Gaussian beam profile, homogeneous irradiation on entire tumor surface is hardly employed, implicating partial removal of

tumor tissues [37]. Therefore, the several methods have been suggested to convert such a Gaussian beam to uniform intensity distribution. Jahan et al. suggested using only central core of optically expanded beam spot of the gaussian distribution [144]. Nevertheless, this method was unsuitable for using clinical application due to wasted power of the input beam by demanding high input power. Application of optical elements such as diffractive optical elements (DOE) and multi-lens arrays (MLA) can be an efficient alternative option for uniformly distributed PTT [114, 145]. Previous study employed MLA to deliver multiple micro-beams with comparable energy densities on the tumor and to generate a uniform heat distribution in the irregular tumor surface for expanding thermal necrosis [145]. Furthermore, Kwon et al used DOE to reduced side-effect such as changes in pigmentation, scarring for skin resurfacing by dividing the beam a grid of focused, induced microinjury zone with demonstrates better clinical outcomes in the treatment [146]. For further study, the feasibility of DOE- and MLA-assisted PTT will be tested for even distribution of laser beam and uniform necrosis during laser irradiation with power modulation.

In the range around 50 °C, the necrosis is commonly occurred by devastating the integrity of cell membrane and releases intracellular inflammatory factors [ref, ref]. In previous researches, Inflammatory responses on tumor tissues have been reported on cancer stimulant effect, leading to tumor regeneration and resistance to therapeutic effect [147]. When tumor necrosis factor (TNF-α), one of the inflammatory factors, induced the vascular endothelial growth factor (VEGF) is stimulated which caused angiogenesis and endothelial cell proliferation associated with lymphatic metastases in

CRCs to metastatic spread [148-151]. Therefore, the residual tumor trigger stimulation for tumor proliferation effect due to TNF-α, which is product of necrosis reactant. Therefore, further study will be investigated to identification of molecular mechanism for stimulation effect.

To verify therapeutic effect, this current study used only HE staining for histology analysis for quantitatively evaluation of CN area and OTD area. Further TUNEL assay will examine the quantity of apoptosis and necrosis rate after modulated PTT to identify the tissue effect of modulation [95]. Moreover, the current study tested small xenograft mouse model bearing CT26-based colon tumor to confirm the feasible treatment efficacy. Thus, CT26 tumor bearing large animal models are essential for clinical translation. Further studies using various tumor types, such as breast cancer, prostate cancer and lung cancer are significant to validate therapeutic effect for expanding application of power modulated PTT. In addition, validation of modulation effect using various photothermal agents (porphyrin-based photosensitizer, carbon nanoparticles, IR 780 and SN38) along with miscellaneous wavelength lasers should be conducted for clinical translation.

Chapter 6. Stimulatory effects of laser wavelengths on proliferation and angiogenesis of cancer

6.1. Introduction

Over the decades, laser treatment on cancer have been considered as promising therapeutic modalities. The primary purpose of applying laser treatment is to locally induce irreversible damage from heat or reactive oxygen species in tumor tissues [18, 107]. Although the underlying mechanisms of laser treatment have been well established for effective clinical outcomes, aggressive cancer regrowth on the laser-irradiated tumor has often been observed in clinical studies [127, 152-155]. Due to maldistribution of optical energy and the ambiguous boundary between normal and tumor tissues, laser treatment can stimulate residual or marginal cancer cells, leading to cancer regrowth [36]. A number of research studies have reported rapid proliferation and regrowth of cancer cells under the laser stimulation [127, 128, 130]. Nevertheless, the stimulant effects by the laser irradiation still remain controversial due to contradictory treatment results and various parameters to control, such as wavelength, power dose, and cancer types. Therefore, as the clinical needs for the laser treatment is steadily increasing, the identification of the photo-stimulated mechanisms on cancer cells is necessary to establish the safety guidelines for clinical laser treatment.

Photobiomodulation (PBM or low-level laser therapy) has been widely

introduced in clinic as a potential therapeutic modality [156-158]. PBM is a minimally- or non-invasive treatment option that commonly utilizes a wavelength of 600 to 1000 nm and a power of 5 to 500 mW [159]. Unlike high power laser treatment, PBM delivers sufficient energy to tissue in order to stimulate biological responses with no or minimal thermal damage to the surrounding tissue. Normally, PBM has been reported to be efficacious for tissue regeneration, rapid wound healing, suppression of inflammatory responses, and pain reduction. For instance, Farouk *et al.* demonstrated the acceleration of wound healing on diabetic rats by using 532, 633, 810, and 980 nm diode lasers with different treatment doses (5, 10, 20, and 30 J/cm^2) [157]. In addition, endothelial cells and monocytes have been examined with PBM for proliferation and photo-stimulated protein expressions [160]. Moreover, several clinical studies have reported that PBM with 655 nm and 670 nm is effective in pain relief and hair loss [156, 158]. Additionally, a number of clinical studies on PBM have been conducted to treat the postoperative complications of cancer as an effective treatment option in patients [161, 162]. As one of the adjuvant treatments in the management of cancer-related side effects, stimulant mechanisms of PBM on cancer cells have been investigated to explore and prevent adverse consequences, such as cancer recurrence [163]. Although PBM could induce distinctive stimulation on cancer cells, tumor suppression effect of PBM was also found in cancer cells [164]. As a result, the resultant effects of PBM against the cancer cells could be dependent upon tumor types and treatment parameters. Since PBM can entail a wide range of cellular responses on both normal and tumor cells, in-depth comprehension of photo-stimulated mechanisms against cancer cells

still remains necessary to establish the safety margin of PBM against the cancer cells.

The current study aims to elucidate stimulant effects of PBM with various wavelengths (405, 635, and 808 nm) against tumor for establishing the safety margin of laser treatment. We hypothesized that PBM could elevate cancer cell proliferation and angiogenesis in terms of overexpression of biological factors, including epidermal growth factor receptor (EGFR), hypoxia inducible factor-1α (HIF-1α), vascular endothelial growth factor (VEGF), and matrix metalloproteinase-9 (MMP-9). Continuous laser irradiations with the three wavelengths were employed for the PBM application, and the stimulant effects of PBM were characterized *in vitro* and *in vivo*. Western blot and histological analysis were performed to explore the alterations of cancer cell-related markers to ensure the safety margin for PBM against tumor.

6.2 Materials and Methods

6.2.1 Light source

To verify the optimal PBM dosage, the current study employed three continuous laser systems: 405 nm (BL; FC-W-405-5W, CNI, Changchun, China), 635 nm (VIS; SD-635-HS-1W, CNI, Changchun, China), and 808 nm (NIR; FC-W-808A-30W, CNI, Changchun, China). A multimode end-firing flat fiber (core diameter = 600 μm; NA = 0.22; Thorlabs, Inc., Newton, New Jersey, USA) was used to transmit each laser light onto the sample surface (beam size = 1.9 cm^2). A photodiode detector (PD-300-3W, Ophir, Jerusalem, Israel) in conjunction with a power meter (Nova II, Ophir, Jerusalem, Israel) was used to monitor the output power from the optical fiber in order to avoid any experimental errors due to power fluctuation or fiber degradation. The distal end of the fiber was re-polished if the measured transmission was below 85%. The applied irradiance was 200 mW/cm^2, and the four irradiation times were tested: 0, 50, 150, and 250 s. The corresponding laser fluences were 0 (control), 10, 30, and 50 J/cm^2, respectively. According the previous studies, the selected irradiation parameters were reported in clinic [163].

6.2.2 *In vitro* PBM

CT26 murine colon cancer cells were obtained from Korean Cell Line Bank. The CT26 cells were cultured in Dulbecco's modified Eagle's Medium (DMEM, Corning, NY)

supplemented with 10% fetal bovine serum (FBS, Corning, NY) and 1% antibiotic-antimycotic (Gibco, Grand Island, NY). The cells were incubated in a humidified incubator with 5% CO_2 at 37 ℃.

After cell confluence, all the cells were trypsinized and seeded into a 24-well plate (3 x 10^5 cells/well). The seeded cells were kept for 24 h and then illuminated with either BL, VIS, or NIR and 10, 30, and 50 J/cm^2, or remained unstimulated. After 24-h laser irradiation, the standard 2-(4,5-dimethylthiazol-2-yl)-2,5-diphenyltetrazolium bromid (MTT) assay was performed to determine cell viability. 1 mg/ml of MTT solution was added into each well and kept for 4 h in a dark environment. Then, injected MTT solution was eliminated and replaced with dimethyl sulfoxide (DMSO) to dissolve the formed formazan for another 20 min. Thereafter, the absorbance was measured at 540 nm by using a microplate spectrophotometer (Multiskan Go, Thermo Fisher Scientific, Waltham, MA, USA).

6.2.3 *In vitro* western blot

In vitro western blot was performed to confirm the protein expression levels of ERK in CT26 cells after PBM treatment. The cells treated with each PBM condition was harvested and lysed with Radio-Immunoprecipitation Assay (RIPA) buffer (50 mM Tris-HCl; pH 8.0; 2 mM EDTA; 1% Triton X-100; 150 mM NaCl; 1% Sodium deoxycholate and 0.1% SDS) containing protease and phosphatase inhibitors (Sigma-Aldrich, St. Louis, MO, USA). The lysates were collected by centrifugation at 12,000

rpm for 15 mins at 4 ℃. Then, protein concentrations were quantified by using the Pierce™ BCA protein assay kit (Thermo Fisher Scientific, Waltham, MA, USA), following the manufacturer's protocol. The lysate containing 30 μg of protein was loaded on sodium dodecylsulfate-polyacrylamide (SDS-PAGE) gel and transferred to nitrocellulose (NC) membrane. Both electrophoresis and blotting were implemented by using protein gel electrophoresis chamber system (Thermo Fisher Scientific, Waltham, MA, USA). Then, the membranes were blocked in 5% BSA and incubated overnight at 4 ℃ with the diluted primary antibodies for phospho-ERK (sc7383, 1:1000) and ERK1/2 (sc514302, 1:1000). After the membranes were washed three times with TBST buffer [20 mM Tris (pH 7.4), 150 mM NaCl, 0.1% Tween-20], the membranes were kept for 1 h at room temperature with diluted HRP-anti-mouse (1:5000, Invitrogen, Thermo Fisher Scientific, Waltham, MA, USA). The bound antibody was detected by using an imaging system (iBright FL1000, Thermo Fisher Scientific, Waltham, MA, USA) with the enhanced chemiluminescence (ECL; Amersham ECL Western blotting detection reagents; GE Healthcare, Pittsburgh, PA, USA). Image J (National Institute of Health, Bethesda, MD, USA) was used to quantify the protein expression levels by using the gel analysis plugin [165]. The protein levels were corrected to their unphosphorylated forms.

6.2.4 *In vivo* PBM

16 female nude mice (age: 5 weeks; weight: 19-22 g) were obtained from Hana biotech

(Suwon, Republic of Korea) for establishment of in vivo xenograft tumor models. After one week of acclimation, the suspension of CT26 cells (1.5 x 10^6 cells/ml) was subcutaneously injected into the back of each mouse by using 1 ml sterile syringe. When the tumor size reached approximately 100 mm^3, the mice were randomly divided into four groups: unstimulated group as control (CTRL), BL, VIS, and NIR (n = per group). Before the in vivo test, all the mice were anesthetized in a chamber by using a respiratory anesthesia system (Classic T3, Surgivet, USA) with 3% isoflurane (Terrell™ isoflurane, Piramal Critical Care, Bethlehem, PA, USA) in oxygen (0.6 L/min). Then, 30 J/cm^2 of each laser wavelength was exposed onto the tumor surface. The exposed mice were observed and photographed by using a digital camera (D5100, Nikon, Tokyo, Japan) at four different time points: 0 (D 0), 3 (D 3), 7 (D 7), and 10 (D 10) days after the PBM treatment. The tumor volume of each tumor was calculated by using by using a formula of $V = (l \times w^2) / 2$ [29] when l and w represent the tumor length (mm) and tumor width (mm), respectively. All the animal care and experimental procedures used in the current study followed the Korean National Institutes of Health (KNIH) guidelines. The current animal test was approved by the Institutional Animal Care and Use Committee of Pukyong National University (Permit number: PKNUIACUC-2021-04).

6.2.5 *In vivo* immunohistochemistry (IHC) staining

Ten days after PBM treatment, all tumor tissues were extracted from mice and fixed in

4 % paraformaldehyde for two days. The samples were embedded in paraffine blocks and sectioned to 6 μm thickness. After deparaffinization and rehydration, endogenous peroxidase of each slide was inactivated by 3% hydrogen peroxide in methanol and washed. Thereafter, each slide was incubated with the diluted primary antibodies at room temperature for 90 mins in a humidified chamber. The primary antibodies included VEGF (5364R, 1:1000), EGFR (MA5-13070, 1:1000), HIF-1α (sc-13515, 1:1000), and MMP-9 (sc-13520, 1:1000). Then, the slides were incubated with the diluted biotinylated secondary antibodies for 30 min and detected with DAB substrate. The sections were counterstained with hematoxylin and observed under the optical microscopy (Motic easyscan, Motic, Kowloon, Hong Kong). For quantitative analysis, the intensity of staining was estimated by using the IHC image analysis tool in Image J.

6.2.6 *In vivo* western blot

In vivo tumor tissues were harvested 10 days after PBM treatment and lysed by RIPA buffer supplemented with 1% protease and phosphatase inhibitor cocktails. As described previously, 30 μg of proteins was resolved by 10% SDS-PAGE gel and transferred to NC membranes. After being blocked with 5% BSA, the membraned were probed overnight at 4 ℃ with the primary antibodies for VEGF (5364R, 1:1000), EGFR (MA5-13070, 1:1000), HIF-1α (sc-13515, 1:1000), and MMP-9 (sc-13520, 1:1000), followed by the appropriate secondary antibodies. The protein bands were detected by

using iBright an imaging system. Beta-actin was used for normalization.

6.2.7 *In vivo* quantitative real time polymerase chain reaction (qRT-PCR)

Total mRNA was isolated from the tumor tissue samples of each group by using mechanical homogenization in a TRIzol reagent (Invitrogen, Carlsbad, CA, USA) with the use of SpeedMill (Analytik Jena, Germany), and then, supernatant was collected. Then, chloroform was added to the supernatant and was severely vortexed to mix both TRIzol and chloroform. Next, the mixture was centrifuged at 13,000 RPM and 4 °C for 15 min. The top phase was carefully transferred to a new tube, and isopropanol was added for RNA precipitation. The isopropanol mixture was slowly inverted and incubated in the ice for 20 min. Then, the incubated mixture was centrifuged at 13,000 RPM and 4 °C for 10 min and then, the supernatant was discarded to obtain RNA. 75% ethanol was added to the precipitated RNA and vortexed, and then centrifuged at 13,000 RPM and 4 °C for 10 min. After the centrifugation, the supernatant was carefully removed, and the added ethanol was dried in room temperature. The precipitate was dissolved in diethyl pyrocarbonate (DEPC) containing water.

For gene expression analysis, the total RNA was calculated based on the absorbance at 260 nm and was converted to cDNA, followed by the manufacturer's instruction (Maxime RT PreMix kit, iNtRON Biotechnology, Seongnam South Korea). After reverse transcription reaction, the individual validation of mRNA expression was determined by using the real-time PCR. The real-time PCR was performed in the 25-ul

volume that included SYBR Green qPCR Master Mix (Applied Biosystems, CA, USA) containing each of specific forward and reverse primer and cDNA as a template. The list of all the primers used for the current study is provided in Table 4. The real-time PCR was carried out in QuantStudio1 (Applied Biosystems, CA, USA), and the PCR condition was programmed as follows: 95 °C for 10 min (denaturation); 50 cycles of 95 °C for 15 s followed by 62 °C for 30 s; 72 °C for 30 s (annealing and extension). The fold change expression was evaluated by using the ΔΔCT method. All the experiments were in triplicate independently, and the average CT value was quantified by fold change analysis.

6.2.8 Statistical analysis

All the data were represented as mean ± standard deviation for four independent experiments. For nonparametric statistical analysis, the Mann-Whitney U tests with Bonferroni correction (MU) were performed to compare two groups and statistical significance was considered when $p < 0.05$. The statistical analysis was performed by using SPSS software 22 (SPSS Inc., Chicago, IL, USA).

Gene	Forward primer sequence (5'-3')	Reverse primer sequence (5'-3')
VEGF	TGAGACCCTGGTGGACATCT	CACTCCAGGGCTTCATCGTT
MMP-9	CGACTTTTGTGGTCTTCCCCA	ACTGCTTCTCTCCCATCATCTG

Table 4. qRT-PCR primer sequences

6.3 Results

6.3.1 Photo-stimulated responses in CT26 cells

Stimulant effects of PBM using various laser wavelengths (BL, VIS, and NIR) and fluences (10, 30, and 50 J/cm^2) were evaluated with CT26 cells to determine the optimal irradiation conditions for *in vivo* experiments (Fig. 33). Figure 33(a) shows that regardless of wavelength and fluence, cell viability insignificantly varied, indicating non-toxicity of PBM on the CT26 cells. The expression level of p-ERK was assessed with the CT26 cells to evaluate intracellular stimulation (Fig. 33(b)). According to western blot analysis (top image), the BL irradiation yielded the most evident p-ERK protein expression ($p < 0.05$ vs. CTRL). Compared to CTRL, both VIS and NIR irradiations exhibited slight decreases in the expression levels of p-ERK. Due to no dependence of the PBM effect on fluence, PBM at 30 J/cm^2 was selected for further *in vivo* experiments.

6.3.2 PBM effects in *in vivo* tumor

To investigate stimulant PBM effects of various laser wavelengths on *in vivo* tumors, all PBM-treated mice were monitored for ten days (Fig. 34). As shown in Fig. 34(a), the tumor volume of all the groups increased over time, compared to D 0. At D 10, BL irradiation created the largest tumor whereas CTRL developed the smallest tumor. As the initial tumor volumes were different for all the groups, the relative tumor volume

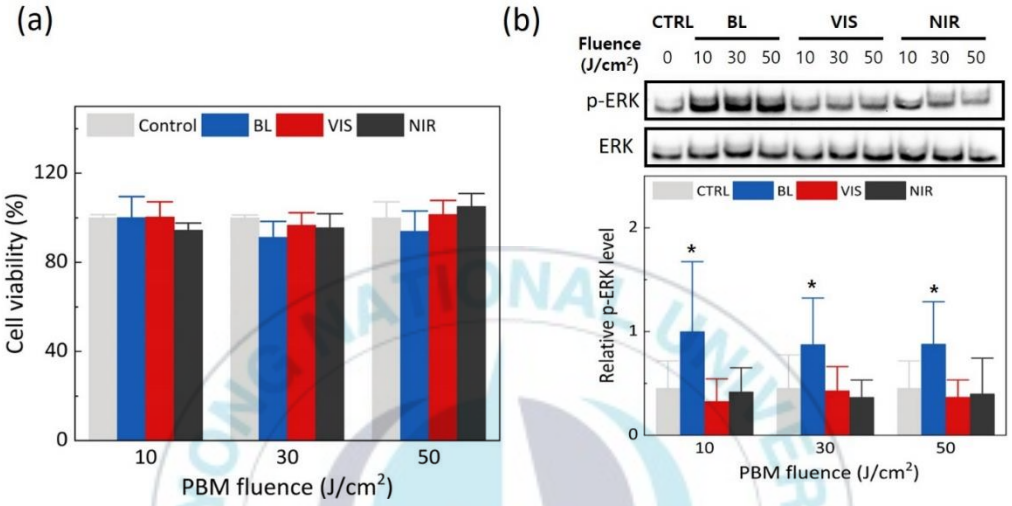

Figure 33. Effect of cytotoxicity and proliferation on CT26 cells: (a) Cell viability after 24 h irradiation with either 405 nm (BL), 635 nm (VIS), or 808 nm (NIR) at 10, 30, and 50 J/cm^2, or remained unstimulated (control), and (b) immunoblotting and relative expression level of p-ERK after treatment with indicated densities and wavelengths in CT26 cells. (N = 3 per group; CTRL = control group; *MU $p < 0.05$ vs. CTRL)

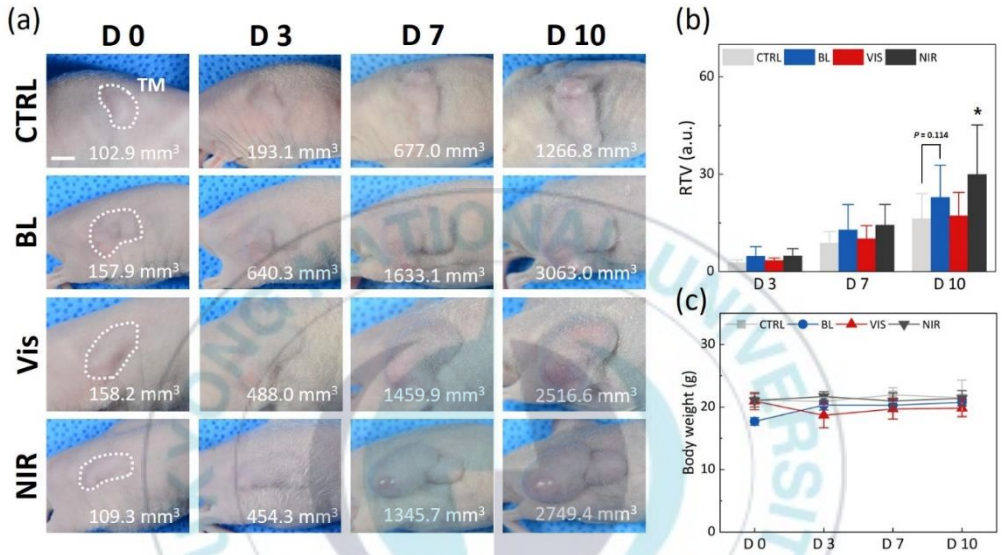

Figure 34. *In vivo* photobiomodulation (PBM) on CT26 tumor-bearing mice: (a) temporal development of tumor at four different time points after irradiation with either BL, VIS, or NIR at 30 J/cm^2, (b) relative tumor volume normalized by initial tumor size (white dot line in (a)), and (c) the body weight changes of tumor-bearing mice for ten days. (N = 4 per groups; scale bar = 5 mm; *MU $p < 0.05$ vs. CTRL)

(RTV in arbitrary unit) was estimated by normalizing the tumor volume at D 10 by one at D 0. According to Fig. 34(b), NIR irradiation showed the maximum RTV at D 10 ($p < 0.05$ vs. CTRL). In spite of the largest tumor size, the BL irradiation yielded a slight increase in the RTV at D 10, compared to CTRL ($p = 0.11$ vs. CTRL). VIS irradiation presented no significant increase in the RTV ($p = 0.48$ vs. CTRL). All the groups confirmed no significant variations in the body weight for the ten days (Fig. 34(c)).

6.3.3 Immunohistochemistry (IHC) analysis

Further IHC staining for EGFR, HIF-1α, VEGF, and MMP-9 was conducted to determine the expression of the protein factors qualitatively. Figure 35(a) shows the representative images of the IHC staining for all the protein factors in CT26 tumors. In Fig. 35(a), the positive cells of all the protein factors ten days after PBM were prominently observed in both BL and NIR groups, compared to CTRL. On the other hand, the cells in VIS group were faintly noticed in all the protein factors. Figures 35(b)-35(e) compare each immunoreactive area percentage in tumor tissues. Both BL and NIR irradiations significantly induced all the protein expressions in the tumor tissues ($p < 0.05$ vs. CTRL). However, no statistically significant difference was found between VIS and CTRL. Collectively, PBM with BL and NIR upregulated the expressions of proliferation- and angiogenesis-related factors, implicating that both BL and NIR irradiations could stimulate the aggressive growth of the cancer cells.

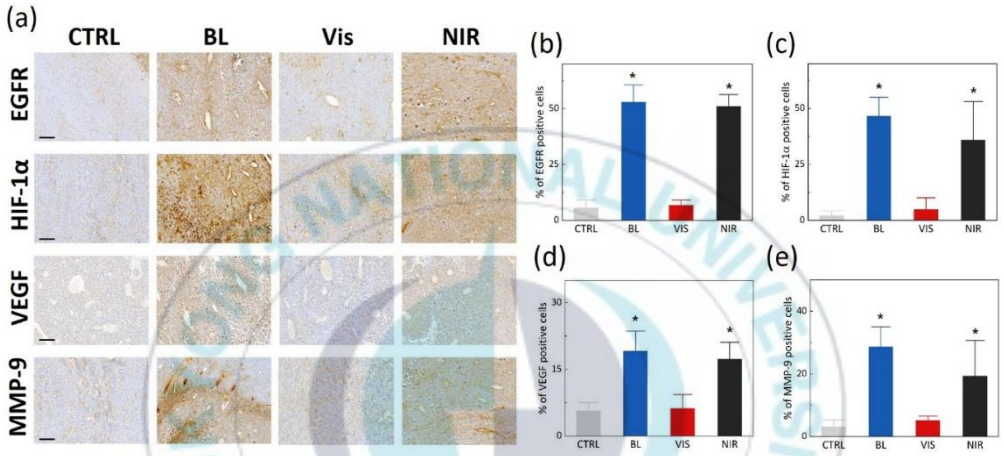

Figure 35. CT26 tumor sections underwent immunohistochemistry (IHC) staining: (a) Representative capture images of the IHC staining for all the protein factors after various PBM treatment at 30 J/cm^2, and immunoreactive area percentages of (b) EGFR, (c) HIF-1α, (d) VEGF, and (e) MMP-9 in tumor tissues. (N = 4 per group; *MU $p <$ 0.05 vs. CTRL)

6.3.4 *In vivo* western blot analysis

Figure 36 demonstrates the protein expression levels of EGFR, HIF-1α, VEGF, and MMP-9 to assess proliferation and angiogenesis pathways in tumor tissue after PBM at 30 J/cm^2. According to Fig. 36(a), BL irradiation upregulated all the protein expression levels. On the other hand, NIR irradiation showed selective upregulation in VEGF and MMP-9, and VIS irradiation resulted in slight changes in the protein expression levels. The relative expression level of each protein was quantified in Figs. 36(b)-(e). Evidently, the BL irradiation increased all the protein expression levels ($p < 0.05$ vs. CTRL). In the case of the NIR irradiation, both EFGR and HIF-1a increased relatively ($p = 0.057$ vs. CTRL), but both VEGF and MMP-9 were significantly upregulated ($p < 0.05$ vs. CTRL). These results suggested that PBM with BL could accelerate tumor progression and aggressive growth due to overexpression of EGFR and HIF-1α. The higher expression of VEGF and MMP-9 implicates that both BL and NIR irradiations could yield strong stimulant effects on angiogenesis and metastasis.

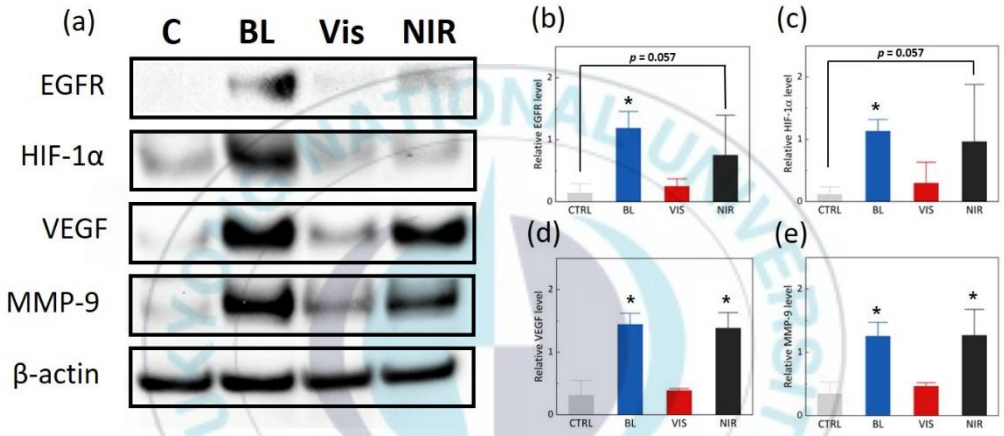

Figure 36. The influence of PBM on CT26 tumor-bearing mouse models: (a) Western blotting of CT26 tumor tissues after various PBM treatment at 30J/cm^2, and quantified relative expression levels of (b) EGFR, (c) HIF-1α, (d) VEGF, and (e) MMP-9 normalized with β-actin, respectively. (N = 4 per group; *MU $p < 0.05$ vs. CTRL)

6.4 Discussion and conclusion

Although the underlying mechanisms of PBM on cancer cells are poorly elucidated, PBM has been widely applied for clinical evaluations on the postoperative complications of cancer treatment. For instance, PBM is frequently applied for head and neck cancer patients to treat and prevent oropharyngeal mucositis, which is one of head and neck cancer complications [161, 162]. In addition, PBM has been suggested as a promising treatment option for the secondary lymphedema on breast cancer treatment [166]. However, various studies reported that PBM undesirably modified the expression of proteins related to progression and invasion in cancer cells by activating PI3K and RTK/PKCs signaling pathways [128, 162]. Therefore, identification of bioactive mechanisms on PBM is pivotal to pave the way for establishment of safety guidelines on the use of laser treatment. The present study verified the effect of various wavelengths on PBM against cancer in vitro and in vivo. Given the same fluence conditions, both BL and NIR could aggravate the behavior of the cancer cells by increasing the expressions of EGFR, HIF-1α, VEGF, and MMP-9. Although the current study selected only three wavelengths (BL, VIS, and NIR) to compare the cellular responses from cancer cells, further studies should test other wavelengths (individual and combined) to elucidate the molecular mechanisms of PBM for potential clinical applications. Currently, NIR laser treatment has been widely conducted in medical fields because of deeper optical penetration into tumor tissue [167]. Both treatment doses as well as wavelengths should be examined to establish the safety guidelines for

clinical laser treatment because intracellular reactions of PBM are dose- and wavelength-dependent.

Both BL and NIR groups demonstrated that at D 10 after PBM, the expressions of EGFR, HIF-1α, VEGF, and MMP-9 were dramatically upregulated, compared to CTRL (Figs. 35 and 36). These factors are frequently reported for aggressive proliferation and angiogenesis in cancer cells. As one of the biomarkers in cancer, the overexpression of EGFR and MMP-9 are strongly linked to advanced tumor progression and invasion, leading to high risk of recurrence and metastasis [168, 169]. EGFR plays a key role in a PI3K signaling pathway, which eventually induces MMP-9 expression [169]. MMP-9 is involved in tumor cell invasion in terms of degradation of extracellular matrix and induction of local angiogenesis due to its ability to cleave VEGF [170]. Furthermore, HIF-1α and VEGF are closely correlated with angiogenesis that occurs in the microenvironment of tumor tissue. In fact, hypoxia easily exists in the tumor entities due to the aggressive proliferation of tumor cells, indicating excessive oxygen consumption [132]. HIF-1α, a transcriptional complex activated by hypoxic stress, regulates the transcriptional regulation of VEGF [171]. As both HIF-1α and VEGF play critical roles in stimulating the formation of the new blood vessels to deliver adequate oxygen, tumor aggressiveness can be increased in solid tumors. Since the cellular activities in tumor tissue can be promoted in response to a broad range of stimuli, the proposed evaluation remains poorly understood. Therefore, in-depth investigation of oncogenic pathways is necessary to determine the exact mechanism of cellular responses after PBM for warranting the safe laser treatment against cancer.

Recent studies proved that PBM stimulates cellular ATP levels by absorption in intracellular chromophores, such as cytochrome c oxidase [172]. As ATP can stimulate the activation of a PI3K signaling pathway, it is necessary to confirm the signal transduction pathways to further explain the mechanism from ATP [159]. Additionally, as PBM can generate reactive oxygen species (ROS), leading to Akt activation [135], further ROS-related signaling pathways should be analyzed to demonstrate the molecular interaction of PBM on cancer cells.

As shown in Fig. 37, mRNA of VEGF and MMP-9 were preliminarily investigated in CT26 tumor tissues. The relative expression levels of mRNA on VEGF and MMP-9 were consistent with the current results from IHC staining and western blot analysis (Figs. 35 and 36). However, in Fig. 37, VEGF mRNA expression in NIR group was hardly detected. Although VEGF protein generation in the NIR group were confirmed by both IHC staining and Western blot analysis, the VEGF mRNA expression may not always correspond to VEGF protein regulation possibly due to lability of VEGF under the normal oxygen tension and translational regulation [173]. In fact, EGFR and HIF-1α could stimulate MMP-9 and VEGF protein expressions in cancer cells according to PI3K/Akt/mTOR pathways [168, 171]. Therefore, further PCR evaluations for EGFR and HIF-1α mRNA expression will be proceeded to identify the relationship between cancer-related proteins and mRNA expression.

In the current study, murine colon cancer cells (CT26) were used to demonstrate the stimulant effects of PBM on tumor. The CT26 cell lines have been utilized for in vivo tumor models because of rapid growth and abundant blood supply

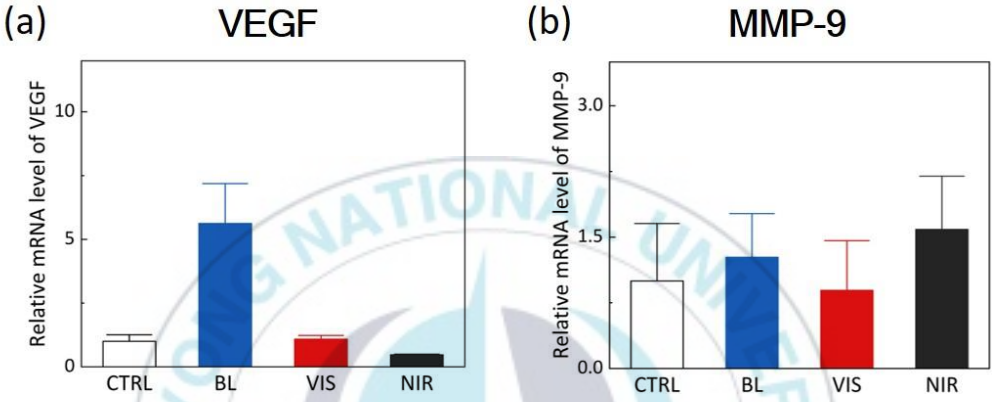

Figure 37. Relative mRNA levels of (a) VEGF and (b) MMP-9 after various PBM treatments at 30 J/cm^2

that are similar to pathological characteristics of human colon cancer [106, 135]. As the tumor tissue has a complex relationship between normal (e.g., epithelial cells) and cancer cells, the stimulatory responses of the normal cells to PBM may differ from that of the cancer cells [163]. In addition, under the same wavelengths, the cellular responses to PBM can be dose-dependent. A wide range of intracellular molecular mechanisms can be produced by various laser fluences. Therefore, the comparison between normal and cancer cells in a dose-dependent manner is essential for clarification of diverse stimulant effects. As most studies has been performed on in vivo mouse models, further evaluations with large animals are required to bridge experimental findings to clinical applications with the use of PBM in oncology. In addition, a photo-induced cancer regrowth model is vital to clarify the stimulant mechanisms after laser treatment by emulating actual clinical environment. Therefore, further in vivo studies will test and quantify the induced cellular responses in the tumour microenvironment for establishment of safety margin after laser treatment.

Chapter 7. Discussion and conclusion

7.1. Summary of current Findings

In this dissertation, the promising photothermal applications have been demonstrated to enhance the treatment efficacy on cancer cells. Furthermore, potential stimulatory effects on cancer cells under laser irradiation have been proved for providing safety margin of clinical laser applications.

Apparently, suggested photothermal agents showed high levels of photothermal conversion efficiency and photostability with biocompatibility and minimal dark toxicity. As a novel photosensitizer agent, gold nanoparticles encapsulated doxorubicin conjugated with marine-derived material fucoidan (Dox-Fu@AuNPs) was investigated as a chemo- and photothermal combined therapy for effective eye cancer treatment. The results indicated that Dox-Fu@AuNPs can had not only minimal toxicity in both cancer and normal cells without laser irradiation but also sufficient photothermal effects due to high photothermal efficacy. It is also observed in in vitro study that the addition of Dox-Fu@AuNPs under laser irradiation (0.11 W/cm^2 for 2 min) promoted enhanced cancer cell death due to significant temperature increment (up to 18 ℃). The in vivo chemo-photothermal therapy assisted with Dox-Fu@AuNPs showed enhanced anti-cancer effects compared to laser treatment only and photoacoustic (PA) signal due to strong light absorption at 532 nm wavelength in both Dox-Fu@AuNPs and abundant blood contents in tumors. Therefore, these in vitro and

in vivo results suggested that the proposed Dox-Fu@AuNPs could serve as not only a potential chemo-photothermal agents but also an effective contrast agent of clinical PA imaging for imaging-guided dual-treatments on eye cancer.

The suggested synthesized organic photothermal agents (NI2 NPs) with twisted structures with strong D-A force and various intramolecular vibrators and rotators showed a significant enhancement of photothermal conversion efficiency and biocompatibility. As synthesized NI2 NPs presented enhanced photothermal conversion efficacy (92. 5%) under 691 nm laser irradiation, the temperature increases of NI2 NPs was 54.4 ± 0.5 ℃ at 100 μM for 1.5 W/cm^2, which could irreversibly damage to cancer cells. In additions, NI2 NPs showed no significant changes in cell viability until 100 μM of concentration without laser irradiation. When 691 nm laser light irradiated to NI2 NPs in tumor cells, irreversible damage was induced, whereas the other treatment groups had no significant changes in tumor. These results indicated that proposed NI2 NPs could inhibit the tumor cell growth without toxicity.

In addition, the development of irradiation method could enhance the therapeutic effects using conventional photothermal agents. In the present study, the fractional laser treatment assisted with multi-lens arrays (MLA) was demonstrated for therapeutic capacity in the tissue upon light absorption, compared to flat fiber-based laser treatment, MLA-assisted irradiation exhibited a higher maximum temperature in a wider thermal region due to uniform delivery of micro-beams. Furthermore, evident tumor volume reduction was confirmed under MLA-assisted irradiation, unlike the

control and flat fiber-based treatment groups. Although MLA were still distributed in a Gaussian profile due to inherent optical nature, MLA can be employed as an alternative therapeutic modality for effective PTT.

In an easy way, modulation of laser irradiation could be one of candidates for effective PTT modalities. As PTT applying constant high irradiance of laser often induce severe thermal injury to the surrounding tissues, moderate power applying is needed to minimize irreversible damage in healthy tissues. Compared to constant power irradiation at higher intensity, the modulated power achieved enhanced tumor necrosis, implicating ablation of cancer through photothermal heating. The current study experimentally confirmed that the proposed power modulation can be a feasible application for effective PTT on colorectal tumors.

Although numerous studies have been conducted to improve therapeutic effects of PTT, several clinical limitations still remain. As described in previous chapters, PTT normally uses photothermal agents to locally convert light energy into heat by minimizing surrounding tissue damages. Thus, in many researches, the toxicity and treatment efficacy of photothermal agents have been regarded as one of major considerations. However, PTT with maldistribution of photothermal agents could induce non-selective cell death due to randomly accumulated agents in tumor tissue [23]. Even though the development of photothermal agents meet clinical requirements such as high photothermal conversion efficiency and low systemic toxicity, the specific

tumor-targeting ability is still needed to develop for prevention of incomplete tumor ablation.

For conventional PTT, a bare-cut flat fiber (Flat) is typically used to delivery laser light to target tissue. However, laser light transmitted by Flat presents Gaussian beam profile, leading to non-uniform distributions. Furthermore, the tumor has three-dimensional irregular shape, implicating non-homogeneous irradiation on entire tumor surface. As a result, the inhomogeneous light and temperature distribution in the tumor tissue could weaken therapeutic effects, leading to incomplete cancer removal. Moreover, the responses of the irradiated residual cancer cells cannot be ignored due to ambiguous laser stimulatory effects. In previous in vivo studies, rapid and aggressive cancer growth was confirmed in laser-irradiated tumor compared to non-treated tumor [145, 174]. In other words, incomplete removal of cancer cells after laser treatment could stimulate cancer cell growth, leading to cancer aggressiveness and regrowth. In fact, these phenomena were occurred in clinical studies related to laser treatment on cancer such as melanoma [154]. These outcomes suggested that laser irradiation may induce cancer cells reaction, leading to aggressive proliferation or invasiveness.

Therefore, development of photoabsorbing agents and optical devices is essential to increase the therapeutic efficiency of PTT, but establishment of safety guidelines for laser treatment are also necessary to prevent cancer stimulatory effects.

7.2 Further directions

Further investigation will focus on applying of suggested PTT on clinical studies. More efforts are still required to establish optimal conditions and safety guidelines for clinical translation on cancer treatment.

The current studies used small mouse tumor model to evaluate pre-clinical treatment effects of suggested methods. As the tumor mass of patients is considerably different from one of fabricated mouse model, the experimental dose used in present studies is not suitable for clinical applications. Normally, in case of newly-developed medicine for cancer, the dosage is determined through a large animal experiment for clinical translation [175, 176]. For clinical use, applied dosage is depending on cancer types, sizes, and the health condition of the patients. Since these conditions are individually different, it is necessary to secure safety of proposed methods by using large animals such as pigs before conducting clinical trials.

As mentioned earlier, laser light follows the Gaussian beam distribution, leading to inhomogeneous irradiation to three-dimensional shape of tumors [36]. Therefore, the development of irradiation method is pivotal to cover entire tumor tissue for complete cancer treatment. For further investigation, diffusing applicator will be employed to uniformly distribute laser light to tumor tissue. Diffusing applicator have been introduced to provide circumferential light distribution along the fiber tip with a wide range of power and wavelengths [37]. Compared to flat fiber, the diffusing applicator could deliver low irradiance of laser light at a large surface area of the tissue

to irradiate tubular tissue structure [37]. Through the pre-test conducted earlier, diffusing applicator could transfer light energy wider and more uniformly than flat fiber, resulting in a wider thermal necrosis (Fig. 38). Since this study is still in its infancy, there are many things to consider. For example, irradiated region from diffusing applicator should cover the entire tumor tissue for complete tissue removal. In addition, photoabsorbing agents should be homogeneously distributed for uniform thermal damage on cancer. Therefore, through this development of an optical transmittance device, the treatment efficacy of PTT will be improved.

Regarding previously described photostimulation effects, near-infrared wavelength of laser has been widely researched in clinic due to deep penetration depth [50, 88]. In order to ensure the safety of laser treatment, quantification of the photostimulation effects on clinical wavelength is crucial. These studies on cancer cells will be helpful for establishment of safety guidelines.

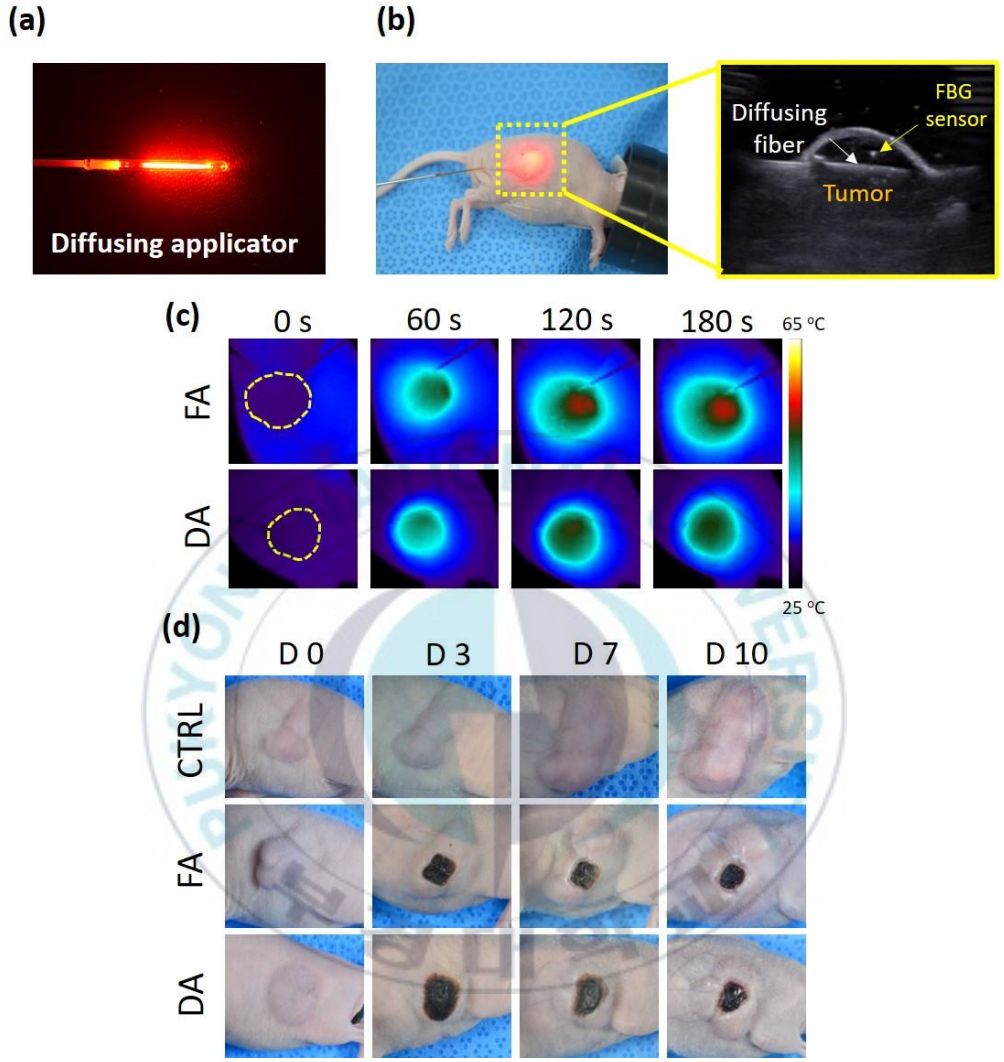

Figure 38. Diffusing applicator for photothermal cancer treatment: (a) image of diffusing applicator (DA) with circumferential light distribution, (b) in vivo photothermal treatment using DA, (c) in vivo thermographic measurement of DA-assisted photothermal therapy on tumor-bearing mice, and (d) compilation of images of tumor model at various time points after laser irradiation.

References

[1] F. Bray, M. Laversanne, E. Weiderpass, and I. Soerjomataram, "The ever-increasing importance of cancer as a leading cause of premature death worldwide," *Cancer*, 2021.

[2] H. Sung, J. Ferlay, R. L. Siegel, M. Laversanne, I. Soerjomataram, A. Jemal, *et al.*, "Global cancer statistics 2020: GLOBOCAN estimates of incidence and mortality worldwide for 36 cancers in 185 countries," *CA: a cancer journal for clinicians*, vol. 71, pp. 209-249, 2021.

[3] S. Preston-Martin, M. C. Pike, R. K. Ross, P. A. Jones, and B. E. Henderson, "Increased cell division as a cause of human cancer," *Cancer research*, vol. 50, pp. 7415-7421, 1990.

[4] H. Nelson, N. Petrelli, A. Carlin, J. Couture, J. Fleshman, J. Guillem, *et al.*, "Guidelines 2000 for colon and rectal cancer surgery," *Journal of the National Cancer Institute*, vol. 93, pp. 583-596, 2001.

[5] A. D. Cook, R. Single, and L. E. McCahill, "Surgical resection of primary tumors in patients who present with stage IV colorectal cancer: an analysis of surveillance, epidemiology, and end results data, 1988 to 2000," *Annals of surgical oncology*, vol. 12, pp. 637-645, 2005.

[6] E. S. Glazer, C. Zhu, K. L. Massey, C. S. Thompson, W. D. Kaluarachchi, A. N. Hamir, *et al.*, "Noninvasive radiofrequency field destruction of pancreatic adenocarcinoma xenografts treated with targeted gold nanoparticles," *Clinical Cancer Research*, vol. 16, pp. 5712-5721, 2010.

[7] P. Tartter, "Blood transfusion and infectious complications following colorectal cancer surgery," *Journal of British Surgery*, vol. 75, pp. 789-792, 1988.

[8] L. E. Mendez, "Iatrogenic injuries in gynecologic cancer surgery," *Surgical Clinics of North America*, vol. 81, pp. 897-923, 2001.

[9] G. Delaney, S. Jacob, C. Featherstone, and M. Barton, "The role of radiotherapy in cancer treatment: estimating optimal utilization from a review of evidence-based clinical guidelines," *Cancer: Interdisciplinary International Journal of the American Cancer Society*, vol. 104, pp. 1129-1137, 2005.

[10] B. A. Chabner and T. G. Roberts, "Chemotherapy and the war on cancer," *Nature Reviews Cancer*, vol. 5, pp. 65-72, 2005.

[11] M. Vanneman and G. Dranoff, "Combining immunotherapy and targeted therapies in cancer treatment," *Nature reviews cancer*, vol. 12, pp. 237-251, 2012.

[12] B. Mansoori, A. Mohammadi, S. Davudian, S. Shirjang, and B. Baradaran, "The different mechanisms of cancer drug resistance: a brief review," *Advanced pharmaceutical bulletin*, vol. 7, p. 339, 2017.

[13] H. S. Jung, P. Verwilst, A. Sharma, J. Shin, J. L. Sessler, and J. S. Kim, "Organic molecule-based photothermal agents: an expanding photothermal

therapy universe," *Chemical Society Reviews,* vol. 47, pp. 2280-2297, 2018.
[14] G. Eskiizmir, A. T. Ermertcan, and K. Yapici, "Nanomaterials: promising structures for the management of oral cancer," in *Nanostructures for oral medicine*, ed: Elsevier, 2017, pp. 511-544.
[15] H. S. Jung, J.-H. Lee, K. Kim, S. Koo, P. Verwilst, J. L. Sessler, *et al.*, "A mitochondria-targeted cryptocyanine-based photothermogenic photosensitizer," *Journal of the American Chemical Society,* vol. 139, pp. 9972-9978, 2017.
[16] X. Li, X.-H. Peng, B.-D. Zheng, J. Tang, Y. Zhao, B.-Y. Zheng, *et al.*, "New application of phthalocyanine molecules: from photodynamic therapy to photothermal therapy by means of structural regulation rather than formation of aggregates," *Chemical science,* vol. 9, pp. 2098-2104, 2018.
[17] M. I. Khot, H. Andrew, H. S. Svavarsdottir, G. Armstrong, A. J. Quyn, and D. G. Jayne, "A review on the scope of photothermal therapy–based nanomedicines in preclinical models of colorectal cancer," *Clinical colorectal cancer,* vol. 18, pp. e200-e209, 2019.
[18] D. Jaque, L. M. Maestro, B. Del Rosal, P. Haro-Gonzalez, A. Benayas, J. Plaza, *et al.*, "Nanoparticles for photothermal therapies," *nanoscale*, vol. 6, pp. 9494-9530, 2014.
[19] M. Johannsen, U. Gneveckow, L. Eckelt, A. Feussner, N. Waldöfner, R. Scholz, *et al.*, "Clinical hyperthermia of prostate cancer using magnetic nanoparticles: presentation of a new interstitial technique," *International journal of hyperthermia,* vol. 21, pp. 637-647, 2005.
[20] J. Mendecki, E. Friedenthal, C. Botstein, R. Paglione, and F. Sterzer, "Microwave applicators for localized hyperthermia treatment of cancer of the prostate," *International Journal of Radiation Oncology* Biology* Physics,* vol. 6, pp. 1583-1588, 1980.
[21] J. R. Lepock, K.-H. Cheng, H. Al-qysi, I. Sim, C. J. Koch, and J. Kruuv, "Hyperthermia-induced inhibition of respiration and mitochondrial protein denaturation in CHL cells," *International journal of hyperthermia,* vol. 3, pp. 123-132, 1987.
[22] J. R. Lepock, H. E. Frey, A. M. Rodahl, and J. Kruuv, "Thermal analysis of CHL V79 cells using differential scanning calorimetry: implications for hyperthermic cell killing and the heat shock response," *Journal of cellular physiology,* vol. 137, pp. 14-24, 1988.
[23] X. Zhang, J. Du, Z. Guo, J. Yu, Q. Gao, W. Yin, *et al.*, "Efficient near infrared light triggered nitric oxide release nanocomposites for sensitizing mild photothermal therapy," *Advanced Science,* vol. 6, p. 1801122, 2019.
[24] S. N. Goldberg, G. S. Gazelle, and P. R. Mueller, "Thermal ablation therapy for focal malignancy: a unified approach to underlying principles, techniques, and diagnostic imaging guidance," *American journal of roentgenology,* vol. 174, pp. 323-331, 2000.
[25] M. A. Ansari, M. Erfanzadeh, and E. Mohajerani, "Mechanisms of laser-tissue

interaction: II. Tissue thermal properties," *Journal of lasers in medical sciences*, vol. 4, p. 99, 2013.

[26] H. S. Han and K. Y. Choi, "Advances in Nanomaterial-Mediated Photothermal Cancer Therapies: Toward Clinical Applications," *Biomedicines*, vol. 9, p. 305, 2021.

[27] E. Boisselier and D. Astruc, "Gold nanoparticles in nanomedicine: preparations, imaging, diagnostics, therapies and toxicity," *Chemical society reviews*, vol. 38, pp. 1759-1782, 2009.

[28] S. Hwang, J. Nam, S. Jung, J. Song, H. Doh, and S. Kim, "Gold nanoparticle-mediated photothermal therapy: current status and future perspective," *Nanomedicine*, vol. 9, pp. 2003-2022, 2014.

[29] L. Jing, X. Liang, Z. Deng, S. Feng, X. Li, M. Huang, *et al.*, "Prussian blue coated gold nanoparticles for simultaneous photoacoustic/CT bimodal imaging and photothermal ablation of cancer," *Biomaterials*, vol. 35, pp. 5814-5821, 2014.

[30] B. Tian, C. Wang, S. Zhang, L. Feng, and Z. Liu, "Photothermally enhanced photodynamic therapy delivered by nano-graphene oxide," *ACS nano*, vol. 5, pp. 7000-7009, 2011.

[31] D. Wang, M. M. Lee, W. Xu, G. Shan, X. Zheng, R. T. Kwok, *et al.*, "Boosting non-radiative decay to do useful work: development of a multi-modality theranostic system from an AIEgen," *Angewandte Chemie*, vol. 131, pp. 5684-5688, 2019.

[32] S. Liu, X. Zhou, H. Zhang, H. Ou, J. W. Lam, Y. Liu, *et al.*, "Molecular motion in aggregates: manipulating TICT for boosting photothermal theranostics," *Journal of the American Chemical Society*, vol. 141, pp. 5359-5368, 2019.

[33] Q. Fan, K. Cheng, Z. Yang, R. Zhang, M. Yang, X. Hu, *et al.*, "Perylene-diimide-based nanoparticles as highly efficient photoacoustic agents for deep brain tumor imaging in living mice," *Advanced materials*, vol. 27, pp. 843-847, 2015.

[34] J. Han, D. Zhao, D. Li, X. Wang, Z. Jin, and K. Zhao, "Polymer-based nanomaterials and applications for vaccines and drugs," *Polymers*, vol. 10, p. 31, 2018.

[35] S. Ye, J. Rao, S. Qiu, J. Zhao, H. He, Z. Yan, *et al.*, "Rational design of conjugated photosensitizers with controllable photoconversion for dually cooperative phototherapy," *Advanced Materials*, vol. 30, p. 1801216, 2018.

[36] S. Wang, X. Ma, X. Hong, Y. Cheng, Y. Tian, S. Zhao, *et al.*, "Adjuvant photothermal therapy inhibits local recurrences after breast-conserving surgery with little skin damage," *ACS nano*, vol. 12, pp. 662-670, 2018.

[37] T. H. Nguyen, Y.-h. Rhee, J.-c. Ahn, and H. W. Kang, "Circumferential irradiation for interstitial coagulation of urethral stricture," *Optics express*, vol. 23, pp. 20829-20840, 2015.

[38] P. L. Triozzi, C. Eng, and A. D. Singh, "Targeted therapy for uveal melanoma," *Cancer treatment reviews*, vol. 34, pp. 247-258, 2008.

[39] M. W. Wilson and J. L. Hungerford, "Comparison of episcleral plaque and proton beam radiation therapy for the treatment of choroidal melanoma," *Ophthalmology,* vol. 106, pp. 1579-1587, 1999.
[40] J. A. Scott, "The computation of temperature rises in the human eye induced by infrared radiation," *Physics in Medicine & Biology,* vol. 33, p. 243, 1988.
[41] J. Lagendijk, "A mathematical model to calculate temperature distributions in human and rabbit eyes during hyperthermic treatment," *Physics in Medicine & Biology,* vol. 27, p. 1301, 1982.
[42] A. Emery, P. Kramar, A. Guy, and J. Lin, "Microwave induced temperature rises in rabbit eyes in cataract research," 1975.
[43] D. N. Krag, S. J. Meijer, D. L. Weaver, B. W. Loggie, S. P. Harlow, K. K. Tanabe, *et al.*, "Minimal-access surgery for staging of malignant melanoma," *Archives of Surgery,* vol. 130, pp. 654-658, 1995.
[44] P. T. Finger, "Radiation therapy for choroidal melanoma," *Survey of ophthalmology,* vol. 42, pp. 215-232, 1997.
[45] S. Nie, Y. Xing, G. J. Kim, and J. W. Simons, "Nanotechnology applications in cancer," *Annu. Rev. Biomed. Eng.,* vol. 9, pp. 257-288, 2007.
[46] X. Huang, I. H. El-Sayed, W. Qian, and M. A. El-Sayed, "Cancer cell imaging and photothermal therapy in the near-infrared region by using gold nanorods," *Journal of the American Chemical Society,* vol. 128, pp. 2115-2120, 2006.
[47] Y. Li, W. Lu, Q. Huang, C. Li, and W. Chen, "Copper sulfide nanoparticles for photothermal ablation of tumor cells," *Nanomedicine,* vol. 5, pp. 1161-1171, 2010.
[48] J.-W. Kim, E. I. Galanzha, E. V. Shashkov, H.-M. Moon, and V. P. Zharov, "Golden carbon nanotubes as multimodal photoacoustic and photothermal high-contrast molecular agents," *Nature nanotechnology,* vol. 4, pp. 688-694, 2009.
[49] K. Yang, S. Zhang, G. Zhang, X. Sun, S.-T. Lee, and Z. Liu, "Graphene in mice: ultrahigh in vivo tumor uptake and efficient photothermal therapy," *Nano letters,* vol. 10, pp. 3318-3323, 2010.
[50] D. P. O'Neal, L. R. Hirsch, N. J. Halas, J. D. Payne, and J. L. West, "Photo-thermal tumor ablation in mice using near infrared-absorbing nanoparticles," *Cancer letters,* vol. 209, pp. 171-176, 2004.
[51] L. Li, L. H. Rashidi, M. Yao, L. Ma, L. Chen, J. Zhang, *et al.*, "CuS nanoagents for photodynamic and photothermal therapies: Phenomena and possible mechanisms," *Photodiagnosis and photodynamic therapy,* vol. 19, pp. 5-14, 2017.
[52] S. B. Lakshmanan, X. Zou, M. Hossu, L. Ma, C. Yang, and W. Chen, "Local field enhanced Au/CuS nanocomposites as efficient photothermal transducer agents for cancer treatment," *Journal of biomedical nanotechnology,* vol. 8, pp. 883-890, 2012.
[53] F. Atashrazm, R. M. Lowenthal, G. M. Woods, A. F. Holloway, and J. L. Dickinson, "Fucoidan and cancer: a multifunctional molecule with anti-tumor

potential," *Marine drugs,* vol. 13, pp. 2327-2346, 2015.
[54] B. Li, F. Lu, X. Wei, and R. Zhao, "Fucoidan: structure and bioactivity," *Molecules,* vol. 13, pp. 1671-1695, 2008.
[55] K.-Y. Lu, R. Li, C.-H. Hsu, C.-W. Lin, S.-C. Chou, M.-L. Tsai, *et al.*, "Development of a new type of multifunctional fucoidan-based nanoparticles for anticancer drug delivery," *Carbohydrate polymers,* vol. 165, pp. 410-420, 2017.
[56] P. Manivasagan, S. Bharathiraja, N. Q. Bui, B. Jang, Y.-O. Oh, I. G. Lim, *et al.*, "Doxorubicin-loaded fucoidan capped gold nanoparticles for drug delivery and photoacoustic imaging," *International journal of biological macromolecules,* vol. 91, pp. 578-588, 2016.
[57] M. Tengdelius, D. Gurav, P. Konradsson, P. Påhlsson, M. Griffith, and O. P. Oommen, "Synthesis and anticancer properties of fucoidan-mimetic glycopolymer coated gold nanoparticles," *Chemical Communications,* vol. 51, pp. 8532-8535, 2015.
[58] L. Zou, H. Wang, B. He, L. Zeng, T. Tan, H. Cao, *et al.*, "Current approaches of photothermal therapy in treating cancer metastasis with nanotherapeutics," *Theranostics,* vol. 6, p. 762, 2016.
[59] Y. Tian, S. Li, J. Song, T. Ji, M. Zhu, G. J. Anderson, *et al.*, "A doxorubicin delivery platform using engineered natural membrane vesicle exosomes for targeted tumor therapy," *Biomaterials,* vol. 35, pp. 2383-2390, 2014.
[60] K. K. Upadhyay, A. N. Bhatt, A. K. Mishra, B. S. Dwarakanath, S. Jain, C. Schatz, *et al.*, "The intracellular drug delivery and anti tumor activity of doxorubicin loaded poly (γ-benzyl l-glutamate)-b-hyaluronan polymersomes," *Biomaterials,* vol. 31, pp. 2882-2892, 2010.
[61] R. Duncan, "Polymer conjugates as anticancer nanomedicines," *Nature reviews cancer,* vol. 6, pp. 688-701, 2006.
[62] A. I. Minchinton and I. F. Tannock, "Drug penetration in solid tumours," *Nature Reviews Cancer,* vol. 6, pp. 583-592, 2006.
[63] G. Pasut and F. Veronese, "Polymer–drug conjugation, recent achievements and general strategies," *Progress in polymer science,* vol. 32, pp. 933-961, 2007.
[64] S. J. Kang and H. E. Grossniklaus, "Rabbit model of retinoblastoma," *Journal of Biomedicine and Biotechnology,* vol. 2011, 2010.
[65] V. P. Nguyen, J. Oh, S. Park, and H. Wook Kang, "Feasibility of photoacoustic evaluations on dual-thermal treatment of ex vivo bladder tumors," *Journal of biophotonics,* vol. 10, pp. 577-588, 2017.
[66] O. Sokolov, N. Selivanov, V. Bogatyrev, O. Selivanova, Y. Velikorodnaya, A. Pocheptsov, *et al.*, "Synthesis and study on activity in vitro of the high purity human butyrylcholinesterase conjugated with gold nanoparticles," in *Doklady Biochemistry and Biophysics*, 2016, pp. 232-234.
[67] A. Zayed, K. Muffler, T. Hahn, S. Rupp, D. Finkelmeier, A. Burger-Kentischer, *et al.*, "Physicochemical and biological characterization of fucoidan from

Fucus vesiculosus purified by dye affinity chromatography," *Marine drugs*, vol. 14, p. 79, 2016.
[68] S. Thomsen, "Pathologic analysis of photothermal and photomechanical effects of laser–tissue interactions," *Photochemistry and photobiology*, vol. 53, pp. 825-835, 1991.
[69] G. P. Luke, D. Yeager, and S. Y. Emelianov, "Biomedical applications of photoacoustic imaging with exogenous contrast agents," *Annals of biomedical engineering*, vol. 40, pp. 422-437, 2012.
[70] P. K. Jain, K. S. Lee, I. H. El-Sayed, and M. A. El-Sayed, "Calculated absorption and scattering properties of gold nanoparticles of different size, shape, and composition: applications in biological imaging and biomedicine," *The journal of physical chemistry B*, vol. 110, pp. 7238-7248, 2006.
[71] A. De La Zerda, C. Zavaleta, S. Keren, S. Vaithilingam, S. Bodapati, Z. Liu, *et al.*, "Carbon nanotubes as photoacoustic molecular imaging agents in living mice," *Nature nanotechnology*, vol. 3, pp. 557-562, 2008.
[72] A. de la Zerda, S. Bodapati, R. Teed, S. Y. May, S. M. Tabakman, Z. Liu, *et al.*, "Family of enhanced photoacoustic imaging agents for high-sensitivity and multiplexing studies in living mice," *ACS nano*, vol. 6, pp. 4694-4701, 2012.
[73] K. Yang, L. Hu, X. Ma, S. Ye, L. Cheng, X. Shi, *et al.*, "Multimodal imaging guided photothermal therapy using functionalized graphene nanosheets anchored with magnetic nanoparticles," *Advanced materials*, vol. 24, pp. 1868-1872, 2012.
[74] M. Baker, "Nanotechnology imaging probes: smaller and more stable," *Nature methods*, vol. 7, pp. 957-962, 2010.
[75] X. Huang, S. Tang, X. Mu, Y. Dai, G. Chen, Z. Zhou, *et al.*, "Freestanding palladium nanosheets with plasmonic and catalytic properties," *Nature nanotechnology*, vol. 6, pp. 28-32, 2011.
[76] A. Dorris, S. Rucareanu, L. Reven, C. J. Barrett, and R. B. Lennox, "Preparation and characterization of polyelectrolyte-coated gold nanoparticles," *Langmuir*, vol. 24, pp. 2532-2538, 2008.
[77] C. Yue, P. Liu, M. Zheng, P. Zhao, Y. Wang, Y. Ma, *et al.*, "IR-780 dye loaded tumor targeting theranostic nanoparticles for NIR imaging and photothermal therapy," *Biomaterials*, vol. 34, pp. 6853-6861, 2013.
[78] J. Peng, L. Zhao, X. Zhu, Y. Sun, W. Feng, Y. Gao, *et al.*, "Hollow silica nanoparticles loaded with hydrophobic phthalocyanine for near-infrared photodynamic and photothermal combination therapy," *Biomaterials*, vol. 34, pp. 7905-7912, 2013.
[79] L. Xia, X. Kong, X. Liu, L. Tu, Y. Zhang, Y. Chang, *et al.*, "An upconversion nanoparticle–zinc phthalocyanine based nanophotosensitizer for photodynamic therapy," *Biomaterials*, vol. 35, pp. 4146-4156, 2014.
[80] L. Cheng, J. Liu, X. Gu, H. Gong, X. Shi, T. Liu, *et al.*, "PEGylated WS2 nanosheets as a multifunctional theranostic agent for in vivo dual-modal CT/photoacoustic imaging guided photothermal therapy," *Advanced materials*,

vol. 26, pp. 1886-1893, 2014.
[81] H. Lee, J.-S. Kim, and E. Kim, "Fucoidan from seaweed Fucus vesiculosus inhibits migration and invasion of human lung cancer cell via PI3K-Akt-mTOR pathways," *PloS one*, vol. 7, p. e50624, 2012.
[82] T.-S. Vo and S.-K. Kim, "Fucoidans as a natural bioactive ingredient for functional foods," *Journal of Functional foods*, vol. 5, pp. 16-27, 2013.
[83] S.-K. Kim, *Marine nutraceuticals: prospects and perspectives*: CRC Press, 2013.
[84] O. Tacar, P. Sriamornsak, and C. R. Dass, "Doxorubicin: an update on anticancer molecular action, toxicity and novel drug delivery systems," *Journal of pharmacy and pharmacology*, vol. 65, pp. 157-170, 2013.
[85] Z. M. Markovic, L. M. Harhaji-Trajkovic, B. M. Todorovic-Markovic, D. P. Kepić, K. M. Arsikin, S. P. Jovanović, *et al.*, "In vitro comparison of the photothermal anticancer activity of graphene nanoparticles and carbon nanotubes," *Biomaterials*, vol. 32, pp. 1121-1129, 2011.
[86] X. Zhao, Q. Chen, W. Liu, Y. Li, H. Tang, X. Liu, *et al.*, "Codelivery of doxorubicin and curcumin with lipid nanoparticles results in improved efficacy of chemotherapy in liver cancer," *International journal of nanomedicine*, vol. 10, p. 257, 2015.
[87] R. Lüpertz, W. Wätjen, R. Kahl, and Y. Chovolou, "Dose-and time-dependent effects of doxorubicin on cytotoxicity, cell cycle and apoptotic cell death in human colon cancer cells," *Toxicology*, vol. 271, pp. 115-121, 2010.
[88] A. Yuan, J. Wu, X. Tang, L. Zhao, F. Xu, and Y. Hu, "Application of near-infrared dyes for tumor imaging, photothermal, and photodynamic therapies," *Journal of pharmaceutical sciences*, vol. 102, pp. 6-28, 2013.
[89] J.-L. Li, L. Wang, X.-Y. Liu, Z.-P. Zhang, H.-C. Guo, W.-M. Liu, *et al.*, "In vitro cancer cell imaging and therapy using transferrin-conjugated gold nanoparticles," *Cancer letters*, vol. 274, pp. 319-326, 2009.
[90] A. J. Welch and M. J. Van Gemert, *Optical-thermal response of laser-irradiated tissue* vol. 2: Springer, 2011.
[91] J. Shao, R. J. Griffin, E. I. Galanzha, J.-W. Kim, N. Koonce, J. Webber, *et al.*, "Photothermal nanodrugs: potential of TNF-gold nanospheres for cancer theranostics," *Scientific reports*, vol. 3, pp. 1-9, 2013.
[92] R. Duan, Z. Zhou, G. Su, L. Liu, M. Guan, B. Du, *et al.*, "Chitosan-coated gold nanorods for cancer therapy combining chemical and photothermal effects," *Macromolecular bioscience*, vol. 14, pp. 1160-1169, 2014.
[93] P. SA., "A Compendium of tissue optical properties," 2012.
[94] E. P. Holowka and S. K. Bhatia, "Controlled-release systems," in *Drug delivery*, ed: Springer, 2014, pp. 7-62.
[95] A. D. Wong, M. Ye, M. B. Ulmschneider, and P. C. Searson, "Quantitative analysis of the enhanced permeation and retention (EPR) effect," *PloS one*, vol. 10, p. e0123461, 2015.
[96] H. Maeda, T. Sawa, and T. Konno, "Mechanism of tumor-targeted delivery of

macromolecular drugs, including the EPR effect in solid tumor and clinical overview of the prototype polymeric drug SMANCS," *Journal of controlled release*, vol. 74, pp. 47-61, 2001.

[97] P. Manivasagan, S. Bharathiraja, M. Santha Moorthy, Y.-O. Oh, K. Song, H. Seo, *et al.*, "Anti-EGFR antibody conjugation of fucoidan-coated gold nanorods as novel photothermal ablation agents for cancer therapy," *ACS applied materials & interfaces*, vol. 9, pp. 14633-14646, 2017.

[98] H. Kim, P. M. Van Phuc Nguyen, M. J. Jung, S. W. Kim, J. Oh, and H. W. Kang, "Doxorubicin-fucoidan-gold nanoparticles composite for dual-chemo-photothermal treatment on eye tumors," *Oncotarget*, vol. 8, p. 113719, 2017.

[99] R. Xia, X. Zheng, X. Hu, S. Liu, and Z. Xie, "Photothermal-controlled generation of alkyl radical from organic nanoparticles for tumor treatment," *ACS applied materials & interfaces*, vol. 11, pp. 5782-5790, 2019.

[100] J. F. Lovell, C. S. Jin, E. Huynh, H. Jin, C. Kim, J. L. Rubinstein, *et al.*, "Porphysome nanovesicles generated by porphyrin bilayers for use as multimodal biophotonic contrast agents," *Nature materials*, vol. 10, pp. 324-332, 2011.

[101] B. Guo, Z. Huang, Q. Shi, E. Middha, S. Xu, L. Li, *et al.*, "Organic small molecule based photothermal agents with molecular rotors for malignant breast cancer therapy," *Advanced Functional Materials*, vol. 30, p. 1907093, 2020.

[102] F. Wu, L. Chen, L. Yue, K. Wang, K. Cheng, J. Chen, *et al.*, "Small-molecule porphyrin-based organic nanoparticles with remarkable photothermal conversion efficiency for in vivo photoacoustic imaging and photothermal therapy," *ACS applied materials & interfaces*, vol. 11, pp. 21408-21416, 2019.

[103] B. Shrestha, L. Tang, and G. Romero, "Nanoparticles-mediated combination therapies for cancer treatment," *Advanced Therapeutics*, vol. 2, p. 1900076, 2019.

[104] R. L. Siegel, K. D. Miller, A. Goding Sauer, S. A. Fedewa, L. F. Butterly, J. C. Anderson, *et al.*, "Colorectal cancer statistics, 2020," *CA: a cancer journal for clinicians*, vol. 70, pp. 145-164, 2020.

[105] C. P. Wild, B. W. Stewart, and C. Wild, *World cancer report 2014*: World Health Organization Geneva, Switzerland, 2014.

[106] C. Chen, J. Neumann, F. Kühn, S. M. Lee, M. Drefs, J. Andrassy, *et al.*, "Establishment of an Endoscopy-Guided Minimally Invasive Orthotopic Mouse Model of Colorectal Cancer," *Cancers*, vol. 12, p. 3007, 2020.

[107] A. Kawczyk-Krupka, A. M. Bugaj, W. Latos, K. Zaremba, K. Wawrzyniec, and A. Sieroń, "Photodynamic therapy in colorectal cancer treatment: the state of the art in clinical trials," *Photodiagnosis and photodynamic therapy*, vol. 12, pp. 545-553, 2015.

[108] D. S. Salem, M. A. Sliem, M. El-Sesy, S. A. Shouman, and Y. Badr, "Improved chemo-photothermal therapy of hepatocellular carcinoma using chitosan-coated gold nanoparticles," *Journal of Photochemistry and Photobiology B: Biology*, vol. 182, pp. 92-99, 2018.

[109] M. Mirrahimi, Z. Abed, J. Beik, I. Shiri, A. S. Dezfuli, V. P. Mahabadi, *et al.*, "A thermo-responsive alginate nanogel platform co-loaded with gold nanoparticles and cisplatin for combined cancer chemo-photothermal therapy," *Pharmacological research*, vol. 143, pp. 178-185, 2019.

[110] Y.-J. Lu, C.-W. Lin, H.-W. Yang, K.-J. Lin, S.-P. Wey, C.-L. Sun, *et al.*, "Biodistribution of PEGylated graphene oxide nanoribbons and their application in cancer chemo-photothermal therapy," *Carbon*, vol. 74, pp. 83-95, 2014.

[111] G. Hong, S. Diao, A. L. Antaris, and H. Dai, "Carbon nanomaterials for biological imaging and nanomedicinal therapy," *Chemical reviews*, vol. 115, pp. 10816-10906, 2015.

[112] N. Fernandes, C. F. Rodrigues, A. F. Moreira, and I. J. Correia, "Overview of the application of inorganic nanomaterials in cancer photothermal therapy," *Biomaterials science*, vol. 8, pp. 2990-3020, 2020.

[113] H. C. Lee, J. Childs, H. J. Chung, J. Park, J. Hong, and S. B. Cho, "Pattern analysis of 532-and 1,064-nm picosecond-domain laser-induced immediate tissue reactions in ex vivo pigmented micropig skin," *Scientific reports*, vol. 9, pp. 1-10, 2019.

[114] H. Kim, J. K. Hwang, M. Jung, J. Choi, and H. W. Kang, "Laser-induced optical breakdown effects of micro-lens arrays and diffractive optical elements on ex vivo porcine skin after 1064 nm picosecond laser irradiation," *Biomedical Optics Express*, vol. 11, pp. 7286-7298, 2020.

[115] S. W. Yoo, H.-J. Park, G. Oh, S. Hwang, M. Yun, T. Wang, *et al.*, "Non-ablative fractional thulium laser irradiation suppresses early tumor growth," *Current Optics and Photonics*, vol. 1, pp. 51-59, 2017.

[116] S. M. Al-Jawad, A. A. Taha, M. M. Al-Halbosiy, and L. F. Al-Barram, "Synthesis and characterization of small-sized gold nanoparticles coated by bovine serum albumin (BSA) for cancer photothermal therapy," *Photodiagnosis and photodynamic therapy*, vol. 21, pp. 201-210, 2018.

[117] M. Kalmar, T. Hoffmann, J. Sauerhering, and F. Klink, "Manufacturing process for hydrogel vessel phantoms," *Current Directions in Biomedical Engineering*, vol. 5, pp. 537-540, 2019.

[118] S. C. Gnyawali, Y. Chen, F. Wu, K. E. Bartels, J. P. Wicksted, H. Liu, *et al.*, "Temperature measurement on tissue surface during laser irradiation," *Medical & biological engineering & computing*, vol. 46, pp. 159-168, 2008.

[119] S. Mahesh and S. C. Joshi, "Thermal conductivity variations with composition of gelatin-silica aerogel-sodium dodecyl sulfate with functionalized multi-walled carbon nanotube doping in their composites," *International Journal of Heat and Mass Transfer*, vol. 87, pp. 606-615, 2015.

[120] L. Mocan, F. A. Tabaran, T. Mocan, C. Bele, A. I. Orza, C. Lucan, *et al.*, "Selective ex-vivo photothermal ablation of human pancreatic cancer with albumin functionalized multiwalled carbon nanotubes," *International journal of nanomedicine*, vol. 6, p. 915, 2011.

[121] M. Takahashi, H. Yasui, A. Ogura, T. Asanuma, N. Kubota, M. Tsujitani, *et al.*, "X Irradiation Combined with TNF α-related Apoptosis-inducing Ligand (TRAIL) Reduces Hypoxic Regions of Human Gastric Adenocarcinoma Xenografts in SCID Mice," *Journal of radiation research*, vol. 49, pp. 153-161, 2008.

[122] J. Lipozenčić and Z. Bukvić Mokoš, "Dermatologic lasers in the treatment of aging skin," *Acta dermatovenerologica Croatica*, vol. 18, pp. 0-0, 2010.

[123] H. J. Laubach, Z. Tannous, R. R. Anderson, and D. Manstein, "Skin responses to fractional photothermolysis," *Lasers in Surgery and Medicine: The Official Journal of the American Society for Laser Medicine and Surgery*, vol. 38, pp. 142-149, 2006.

[124] R. R. Anderson, "Lasers for dermatology and skin biology," *J Invest Dermatol*, vol. 133, pp. E21-23, 2013.

[125] J. Gye, S. K. Ahn, J.-E. Kwon, and S.-P. Hong, "Use of fractional CO2 laser decreases the risk of skin cancer development during ultraviolet exposure in hairless mice," *Dermatologic Surgery*, vol. 41, pp. 378-386, 2015.

[126] C. Kara, H. Selamet, C. Gökmenoğlu, and N. Kara, "Low level laser therapy induces increased viability and proliferation in isolated cancer cells," *Cell proliferation*, vol. 51, p. e12417, 2018.

[127] E. Revazova, I. Bryzgalov, I. Sorokina, A. Ivanov, J. Sebastian, G. Keller, *et al.*, "Stimulation of the growth of human tumor by low-power laser irradiation," *Bulletin of experimental biology and medicine*, vol. 132, pp. 778-779, 2001.

[128] M. Bamps, R. Dok, and S. Nuyts, "Low-level laser therapy stimulates proliferation in head and neck squamous cell carcinoma cells," *Frontiers in oncology*, vol. 8, p. 343, 2018.

[129] J. L. F. De Castro, A. L. B. Pinheiro, C. E. Werneck, and C. P. Soares, "The effect of laser therapy on the proliferation of oral KB carcinoma cells: an in vitro study," *Photomedicine and laser surgery*, vol. 23, pp. 586-589, 2005.

[130] Y.-H. Rhee, J.-H. Moon, S.-H. Choi, and J.-C. Ahn, "Low-level laser therapy promoted aggressive proliferation and angiogenesis through decreasing of transforming growth factor-β1 and increasing of Akt/Hypoxia inducible factor-1α in anaplastic thyroid cancer," *Photomedicine and laser surgery*, vol. 34, pp. 229-235, 2016.

[131] J. Zhang, D. Xing, and X. Gao, "Low-power laser irradiation activates Src tyrosine kinase through reactive oxygen species-mediated signaling pathway," *Journal of cellular physiology*, vol. 217, pp. 518-528, 2008.

[132] X. Jing, F. Yang, C. Shao, K. Wei, M. Xie, H. Shen, *et al.*, "Role of hypoxia in cancer therapy by regulating the tumor microenvironment," *Molecular cancer*, vol. 18, pp. 1-15, 2019.

[133] G. Bredholt, M. Mannelqvist, I. M. Stefansson, E. Birkeland, T. H. Bø, A. M. Øyan, *et al.*, "Tumor necrosis is an important hallmark of aggressive endometrial cancer and associates with hypoxia, angiogenesis and

inflammation responses," *Oncotarget*, vol. 6, p. 39676, 2015.
[134] C. Kopp, L. Ravel, and P. Meyrueis, "Efficient beamshaper homogenizer design combining diffractive optical elements, microlens array and random phase plate," *Journal of Optics A: Pure and Applied Optics*, vol. 1, p. 398, 1999.
[135] M. Przybyszewska, J. Miłoszewska, A. Kotlarz, P. Swoboda, K. Pyśniak, W. Szczepek, *et al.*, "Imatinib inhibits the renewal and tumorigenicity of CT-26 colon cancer cells after cytoreductive treatment with doxorubicin," *Archivum immunologiae et therapiae experimentalis*, vol. 65, pp. 51-67, 2017.
[136] P. Lai, X. Xu, and L. V. Wang, "Dependence of optical scattering from Intralipid in gelatin-gel based tissue-mimicking phantoms on mixing temperature and time," *Journal of biomedical optics*, vol. 19, p. 035002, 2014.
[137] J. B. Vines, J.-H. Yoon, N.-E. Ryu, D.-J. Lim, and H. Park, "Gold nanoparticles for photothermal cancer therapy," *Frontiers in chemistry*, vol. 7, p. 167, 2019.
[138] C.-D. Chen, S.-F. Cheng, L.-K. Chau, and C. C. Wang, "Sensing capability of the localized surface plasmon resonance of gold nanorods," *Biosensors and Bioelectronics*, vol. 22, pp. 926-932, 2007.
[139] V. G. Truong, Y. W. Lee, and H. W. Kang, "Effect of optical energy modulation on the thermal response of biological tissue: computational and experimental validations," *Biomedical Optics Express*, vol. 11, pp. 6905-6919, 2020.
[140] G.-T. Huang, T.-H. Wang, J.-C. Sheu, N. Daikuzono, J.-L. Sung, M.-Z. Wu, *et al.*, "Low-power laserthermia for the treatment of small hepatocellular carcinoma," *European Journal of Cancer and Clinical Oncology*, vol. 27, pp. 1622-1627, 1991.
[141] K.-G. Tranberg, L. Myllymäki, P. Möller, K. Ivarsson, H. O. Sjögren, and U. Stenram, "Interstitial laser thermotherapy of a rat liver adenocarcinoma," *Journal of X-ray science and technology*, vol. 10, pp. 177-185, 2002.
[142] L. Guan and G. Xu, "Damage effect of high-intensity focused ultrasound on breast cancer tissues and their vascularities," *World journal of surgical oncology*, vol. 14, pp. 1-17, 2016.
[143] D. T. Phan, L. H. Tran, S. Park, J. Choi, H. W. Kang, and J. Oh, "Enhanced precision of real-time control photothermal therapy using cost-effective infrared sensor array and artificial neural network," *Computers in Biology and Medicine*, p. 104960, 2021.
[144] S. Jahan and M. Karim, "Refracting systems for Gaussian-to-uniform beam transformations," *Optics & Laser Technology*, vol. 21, pp. 27-30, 1989.
[145] H. Kim, H. Pyo, H. Kim, and H. W. Kang, "Multi-Lens Arrays (MLA)-Assisted Photothermal Effects for Enhanced Fractional Cancer Treatment: Computational and Experimental Validations," *Cancers*, vol. 13, p. 1146, 2021.
[146] H. Kwon, S. Yang, Y. Cho, E. Shin, M. Choi, Y. Bae, *et al.*, "Comparison of a 1064-nm neodymium-doped yttrium aluminum garnet picosecond laser using a diffractive optical element vs. a nonablative 1550-nm erbium-glass laser for the treatment of facial acne scarring in Asian patients: a 17-week prospective,

randomized, split-face, controlled trial," *Journal of the European Academy of Dermatology and Venereology,* vol. 34, pp. 2907-2913, 2020.
[147] A. Mantovani, P. Allavena, A. Sica, and F. Balkwill, "Cancer-related inflammation," *nature,* vol. 454, pp. 436-444, 2008.
[148] R. K. Kannadorai, G. G. Y. Chiew, K. Q. Luo, and Q. Liu, "Dual functions of gold nanorods as photothermal agent and autofluorescence enhancer to track cell death during plasmonic photothermal therapy," *Cancer letters,* vol. 357, pp. 152-159, 2015.
[149] B. Li, B. Wang, M. Chen, G. Li, M. Fang, and J. Zhai, "Expression and interaction of TNF-α and VEGF in chronic stress-induced depressive rats," *Experimental and therapeutic medicine,* vol. 10, pp. 863-868, 2015.
[150] H. Wajant, "The role of TNF in cancer," *Death Receptors and Cognate Ligands in Cancer,* pp. 1-15, 2009.
[151] L. Zhang, Y. Zhang, Y. Xue, Y. Wu, Q. Wang, L. Xue, *et al.*, "Transforming Weakness into Strength: Photothermal-Therapy-Induced Inflammation Enhanced Cytopharmaceutical Chemotherapy as a Combination Anticancer Treatment," *Advanced Materials,* vol. 31, p. 1805936, 2019.
[152] S. W. Yoo, G. Oh, A. M. Safi, S. Hwang, Y.-S. Seo, K.-H. Lee, *et al.*, "Endoscopic non-ablative fractional laser therapy in an orthotopic colon tumour model," *Scientific reports,* vol. 8, pp. 1-11, 2018.
[153] C. Ash, G. Town, R. Whittall, L. Tooze, and J. Phillips, "Lasers and intense pulsed light (IPL) association with cancerous lesions," *Lasers in medical science,* vol. 32, pp. 1927-1933, 2017.
[154] M. C. Zipser, J. Mangana, P. A. Oberholzer, L. E. French, and R. Dummer, "Melanoma after laser therapy of pigmented lesions-circumstances and outcome," *European Journal of Dermatology,* vol. 20, pp. 334-338, 2010.
[155] M. Myakishev-Rempel, I. Stadler, P. Brondon, D. R. Axe, M. Friedman, F. B. Nardia, *et al.*, "A preliminary study of the safety of red light phototherapy of tissues harboring cancer," *Photomedicine and laser surgery,* vol. 30, pp. 551-558, 2012.
[156] P. Avci, G. K. Gupta, J. Clark, N. Wikonkal, and M. R. Hamblin, "Low-level laser (light) therapy (LLLT) for treatment of hair loss," *Lasers in surgery and medicine,* vol. 46, pp. 144-151, 2014.
[157] F. A. Al-Watban, X. Y. Zhang, and B. L. Andres, "Low-level laser therapy enhances wound healing in diabetic rats: a comparison of different lasers," *Photomedicine and laser surgery,* vol. 25, pp. 72-77, 2007.
[158] D. Turhani, M. Scheriau, D. Kapral, T. Benesch, E. Jonke, and H. P. Bantleon, "Pain relief by single low-level laser irradiation in orthodontic patients undergoing fixed appliance therapy," *American Journal of Orthodontics and Dentofacial Orthopedics,* vol. 130, pp. 371-377, 2006.
[159] L. F. de Freitas and M. R. Hamblin, "Proposed mechanisms of photobiomodulation or low-level light therapy," *IEEE Journal of selected topics in quantum electronics,* vol. 22, pp. 348-364, 2016.

[160] M. G. Bouma, W. A. Buurman, and F. A. van den Wildenberg, "Low energy laser irradiation fails to modulate the inflammatory function of human monocytes and endothelial cells," *Lasers in Surgery and Medicine: The Official Journal of the American Society for Laser Medicine and Surgery*, vol. 19, pp. 207-215, 1996.

[161] V. H. Schartinger, O. Galvan, H. Riechelmann, and J. Dudás, "Differential responses of fibroblasts, non-neoplastic epithelial cells, and oral carcinoma cells to low-level laser therapy," *Supportive care in cancer*, vol. 20, pp. 523-529, 2012.

[162] F. F. Sperandio, F. S. Giudice, L. Corrêa, D. S. Pinto Jr, M. R. Hamblin, and S. C. de Sousa, "Low-level laser therapy can produce increased aggressiveness of dysplastic and oral cancer cell lines by modulation of Akt/mTOR signaling pathway," *Journal of biophotonics*, vol. 6, pp. 839-847, 2013.

[163] S. Y. Tam, V. C. Tam, S. Ramkumar, M. L. Khaw, H. K. Law, and S. W. Lee, "Review on the cellular mechanisms of low-level laser therapy use in oncology," *Frontiers in Oncology*, vol. 10, p. 1255, 2020.

[164] M. R. Hamblin, S. T. Nelson, and J. R. Strahan, "Photobiomodulation and cancer: what is the truth?," *Photomedicine and laser surgery*, vol. 36, pp. 241-245, 2018.

[165] K. A. Janes, "An analysis of critical factors for quantitative immunoblotting," *Science signaling*, vol. 8, pp. rs2-rs2, 2015.

[166] R.-J. Bensadoun, "Photobiomodulation or low-level laser therapy in the management of cancer therapy-induced mucositis, dermatitis and lymphedema," *Current opinion in oncology*, vol. 30, pp. 226-232, 2018.

[167] M.-F. Tsai, S.-H. G. Chang, F.-Y. Cheng, V. Shanmugam, Y.-S. Cheng, C.-H. Su, *et al.*, "Au nanorod design as light-absorber in the first and second biological near-infrared windows for in vivo photothermal therapy," *ACS nano*, vol. 7, pp. 5330-5342, 2013.

[168] P. Nastały, S. Stoupiec, M. Popęda, J. Smentoch, T. Schlomm, C. Morrissey, *et al.*, "EGFR as a stable marker of prostate cancer dissemination to bones," *British Journal of Cancer*, vol. 123, pp. 1767-1774, 2020.

[169] A. Merdad, S. Karim, H.-J. Schulten, A. Dallol, A. Buhmeida, F. Al-Thubaity, *et al.*, "Expression of matrix metalloproteinases (MMPs) in primary human breast cancer: MMP-9 as a potential biomarker for cancer invasion and metastasis," *Anticancer research*, vol. 34, pp. 1355-1366, 2014.

[170] H. Zheng, H. Takahashi, Y. Murai, Z. Cui, K. Nomoto, H. Niwa, *et al.*, "Expressions of MMP-2, MMP-9 and VEGF are closely linked to growth, invasion, metastasis and angiogenesis of gastric carcinoma," *Anticancer research*, vol. 26, pp. 3579-3583, 2006.

[171] D. Cao, M. Hou, Y.-s. Guan, M. Jiang, Y. Yang, and H.-f. Gou, "Expression of HIF-1alpha and VEGF in colorectal cancer: association with clinical outcomes and prognostic implications," *BMC cancer*, vol. 9, pp. 1-9, 2009.

[172] Y. Wang, Y.-Y. Huang, Y. Wang, P. Lyu, and M. R. Hamblin,

"Photobiomodulation of human adipose-derived stem cells using 810 nm and 980 nm lasers operates via different mechanisms of action," *Biochimica et Biophysica Acta (BBA)-General Subjects*, vol. 1861, pp. 441-449, 2017.

[173] D. Yoshikawa, H. Ojima, A. Kokubu, T. Ochiya, S. Kasai, S. Hirohashi, *et al.*, "Vandetanib (ZD6474), an inhibitor of VEGFR and EGFR signalling, as a novel molecular-targeted therapy against cholangiocarcinoma," *British journal of cancer*, vol. 100, pp. 1257-1266, 2009.

[174] H. Kim, S. W. Kim, K. H. Seok, C. W. Hwang, J.-C. Ahn, J.-O. Jin, *et al.*, "Hypericin-assisted photodynamic therapy against anaplastic thyroid cancer," *Photodiagnosis and photodynamic therapy*, vol. 24, pp. 15-21, 2018.

[175] S. Prat, S. Gallardo-Villares, M. Vives, A. Carreño, M. Caminal, I. Oliver-Vila, *et al.*, "Clinical translation of a mesenchymal stromal cell-based therapy developed in a large animal model and two case studies of the treatment of atrophic pseudoarthrosis," *Journal of tissue engineering and regenerative medicine*, vol. 12, pp. e532-e540, 2018.

[176] H. Madry, M. Ochi, M. Cucchiarini, D. Pape, and R. Seil, "Large animal models in experimental knee sports surgery: focus on clinical translation," *Journal of experimental orthopaedics*, vol. 2, pp. 1-12, 2015.

Appendix – Curriculum Vitae

I. Research Interests

- Enhancement of photothermal/photodynamic treatment for effective cancer treatment
- Development of nanomaterials for specific targeting to cancer cells
- Molecular mechanism investigation of photobiomodulative effect on cancer cells
- Evaluation of cancer cell activity under laser irradiation in vitro and in vivo
- Development of optical applicators for effective optical energy delivery to tissue

II. Technical Skills

○ **Laser-assisted technique**

- Optical fiber fabrication
- Design of optical applicators for laser treatment
- Development of optical phantoms for mimicking human skin structure
- Photodynamic/photothermal treatment with nanomaterials for cancer treatment

○ **Molecular technique**

- Western blotting analysis
- Confocal microscopic image analysis

○ **Animal experiment**

- Establishment of scar and tumor mouse models
- Establishment of hemostasis rabbit model
- Histological analysis (Hematoxylin & Eosin staining and Masson's trichrome staining)
- Immunohistochemistry staining

○ **Software skill**

- Solidworks
- COMSOL
- ImageJ analysis
- Origin
- Matlab
- SPSS statistical analysis

III. Research Experience

Period	Position	Contents
2021. 02. – current	Research Assistant	"Research Center for Marine-integrated Biomedical Technology" funded by National Research Foundation of Korea (NRF), Korea, worked on **Investigation of molecular mechanisms of photobiomodulative effects on cancer cells**
2020. 11. – current	Research Assistant	"Development of AI/AR-based smart medical system for diagnosis/treatment of pancreatic cancer" funded by the Korea government, Korea, worked on **development of optical applicator for effective cancer treatment**
2018. 02. – 2021. 01.	Research Assistant	"Research on photothermally-enhanced photoimmuno treatment of high recurrent CIS/Ta-stage bladder tumor with multi-wavelengths" funded by National Research Foundation of Korea (NRF), Korea, worked on **development and investigation of photothermally-enhanced nanomaterials for bladder cancer**
2016.04 – 2021.03	Research Assistant	"Development of intelligent micro-patterning-based light delivery catheter system for endoscopic treatment" funded by the Ministry of Health & Welfare, Korea, worked on **evaluation of in vivo model tissue and safety test**
2015. 05. – 2019. 12.	Research Assistant	"Research & Development for Commercial Marine-Integrated Bionics Materials and Technology" funded by Korea Institute of Marine Science & Technology (KIMST), Korea, worked on **marine material-assisted photothermal/photodynamic therapy on cancer cells**
2015. 06. - 2016. 05.	Research Assistant	"the Industrial Strategic Technology Development Program" funded by the Ministry of Trade, Industry & Energy, Korea, worked on **research and development of double-layered optical skin phantom for imaging system**

IV. Peer-reviewed Publications

○ **Submission**

1. **Kim H**, Kim E, Kim TH, Heo SY, and Kang HW. Stimulatory effects of wavelength-dependent photobiomodulation on proliferation and angiogenesis of colorectal cancer. Journal of photochemistry and photobiology: B 2021;
2. **Kim E, Kim H**, and Kang HW. Temporal power modulation for enhancement of gold nanorods-assisted photothermal treatment on colorectal cancer. Laser surgery and medicine. 2021;
3. **Pham TC, Kim H**, Choi Y, Kang HW, and Lee S. Facile preparation of nano platform for high efficiency of photothermal therapy in tumor. *Chemical Science* 2021;

○ **Publication**

1. **Kim H**, Pyo H, Kim H, and Kang HW. Micro-lens arrays (MLA)-assisted photothermal effects for enhanced fractional cancer treatment: computational and experimental validations. *Cancers* 2021; 13: 1146
2. Lee Y, Kim M, **Kim H**, Pyo H, and Kang HW. Phloroglucinol-combined photobiomodulation for minimizing burn-induced skin fibrosis. *IEEE Journal of Selected Topics in Quantum Electronics* 2021; 27: 7000109
3. Shanmugapriya K, **Kim H**, and Kang HW. EGFR-conjugated hydrogel accelerates wound healing on ulcer-induced burn wounds by targeting collagen and inflammatory cells using photoimmunomodulatory inhibition. *Materials Science & Engineering C* 2020; 118: 111541
4. Shanmugapriya K, **Kim H**, and Kang HW. Fucoidan-loaded hydrogels facilitate wound healing using photodynamic therapy by in vitro and in vivo evaluation. *Carbohydrate Polymers* 2020; 247: 116624
5. Tian Y, **Kim H**, and Kang HW. In vitro anti-tumor effect of high-fluence low-power laser light on apoptosis of human colorectal cancer cells. *Lasers in Medical Science* 2021: 36: 513-520.
6. Shanmugapriya K, **Kim H**, and Kang HW. Epidermal growth factor receptor conjugated fucoidan/alginates loaded hydrogel for activating EGFR/AKT signaling pathways in colon cancer cells during targeted photodynamic therapy. *International Journal of Biological Macromolecules* 2020; 158: 1163
7. Shanmugapriya K, **Kim H**, Lee YW, and Kang HW. Cellulose nanocrystals/nanofibrils loaded astaxanthin nanoemulsion for the induction of apoptosis via ROS-dependent mitochondrial dysfunction in cancer cells under photobiomodulation. *International Journal of Biological Macromolecules* 2020; 149:165
8. Shanmugapriya K, **Kim H**, Lee YW, and Kang HW. Multifunctional heteropolysaccharide hydrogel under photobiomodulation for accelerated wound regeneration. *Ceramics International* 2019; 46: 7268

9. Park S, Hwang J, Park J, **Kim H**, Ahn Y, and Kang HW. Application of ultrasound thermal imaging for monitoring laser ablation in ex vivo cardiac tissue. *Lasers in Surgery and Medicine* 2020; 52: 218
10. Tian Y, Lee Y, **Kim H**, and Kang HW. In vitro anti-tumor effect of low power laser irradiation (LPLI) on gastroenterological carcinoma cells. *Lasers in Medical Science* 2020; 35: 677
11. Shanmugapriya K, **Kim H**, and Kang HW. Nanoengineered chlorin e6 conjugated with hydrogel for photodynamic therapy on cancer. *Colloids and Surfaces B: Biointerfaces* 2019; 181: 778-788
12. Lee Y, **Kim H,** Hong N, Ahn J, and Kang HW. Combined treatment of low-level laser therapy and Phlroglucinol for inhibition of fibrosis. *Lasers in Surgery and Medicine* 2020; 52: 276
13. Shanmugapirya K, **Kim H**, and Kang HW. A new alternative insight of nanoemulsion conjugated with κ-carrageenan for wound healing study in diabetic mice: In vitro and in vivo evaluation. *European Journal of Pharmaceutical Sciences* 2019; 133: 236-250
14. Kim M, Kim SW, **Kim H**, Hwang CW, Choi JM, and Kang HW. Comparative evaluations of laser-induced mature scare model in vivo. *Biomedical Optics Express* 2019; 10: 1965-1977
15. Shanmugapriya K, **Kim H**, and Kang HW. In vitro antitumor potential of astaxanthin nanoemulsion against cancer cells via mitochondrial mediated apoptosis. *International Journal of Pharmaceutics* 2019; 560: 334-346
16. Shanmugapriya K, **Kim H**, Saravana PS, Chun B, and Kang HW. Astaxanthin-alpha tocopherol nanoemulsion formulation by emulsification methods: Investigation on anticancer, wound healing, and antibacterial effects. *Colloids and Surfaces B: Biointerfaces* 2018; 172: 170-179
17. **Kim H**, Kim SW, Seok KH, Hwang CW, Jung MJ, and Kang HW. Hypericin-assisted photodynamic therapy on anaplastic thyroid cancer. *Photodiagnosis and Photodynamic Therapy* 2018; 25: 15-21
18. K Shanmugapriya, **Kim H**, Saravana PS, Chun B, and Kang HW. Fabrication of multifunctional nanocomposite film with rapid healing and antibacterial effect for wound management. *International Journal of Biological Macromolecules* 2018; 118: 1713-1725
19. Pham NT, Song W, **Kim** H, Jung JH, Park S, and Kang HW. Feasibility of LED-assisted CMOS camera: contrast estimation for laser tattoo treatment. *Applied Sciences* 2018; 8: 661
20. Kim M, **Kim H**, and Kang HW. Comparative evaluations of hypertrophic scar formation in in vivo models. *Lasers in Surgery and Medicine* 2018; 50: 661-668
21. **Kim H**, Nguyen VP, Manivasagan P, Seok KH, Jung MJ, Kim SW, Oh J, and Kang HW. Doxorubicin-fucoidan-gold nanoparticles composite for photoacoustic image-guided synergistic chemo-photothermal treatment on eye tumors. *Oncotarget* 2017; 8: 113719-113733
22. Hwang J, **Kim H**, Truong VG, Xuan J, Hasenberg T, and Kang HW. Dual-

wavelength-assisted thermal hemostasis for treatment of benign prostate hyperplasia. *Journal of Biophotonics* 2018; 11: e201700192

23. Park HJ, Song W, Lee B, **Kim H**, and Kang HW. Effect of multi-wavelength irradiation on color characterization with light emitting diodes (LEDs). *Journal of the Korean Physical Society* 2017; 20: 1011
24. Nguyen VP, **Kim H**, Kang M, Kwak M, and Kang HW. Application of organic IR788-loaded semi-interpenetrating network (sIPN) dyes for photoacoustic imaging. *Japanese Journal of Applied Physics* 2017; 56: 07JF12
25. Nguyen VP, Kim SW, **Kim H**, Kim H, Seok KH, Jung MJ, Ahn Y, and Kang HW. Biocompatible astaxanthin as novel marine-oriented agents for dual chemo-photothermal therapy. *PLoS One* 2017; 12(4): e0174687
26. Lee B, Song W, **Kim H**, and Kang HW. Application of double-layered skin phantoms for optical flow imaging during laser tattoo treatments. *Journal of the Korean Physical Society* 2016; 68: 1137

V. Patents

○ **International**

1. Method and apparatus for dual-wavelength laser treatment (2018, US)

VI. Conferences

1. H. Kim, Y. Kim, and H. W. Kang, “Photobioodulative effects of laser wavelength on tumor tissue”, SPIE Photonics West 2022 (2022)

2. H. Kim, Y. Kim, and H. W. Kang, “Simulatory effects of laser wavelengths on proliferation and angiogenesis of colon cancer : *in vitro* and *in vivo* evaluations”, SPIE ABC 2021 (2021)

3. H. Kim, H. Pyo, H. Kim and H. W. Kang, “Micro-lens arrays (MLA)-assisted fractional photothermal therapy for effective cancer treatment”, ECBO 2021 (2021)

4. H. Kim, and H. W. Kang, “Micro-lens array (MLA)-enhanced photothermal responses for fractional cancer treatment: ex vivo and in vivo validations” ABC 2020 (2020)

5. H. Kim, and H. W. Kang, “Cell-specific photoimmunotherapy with anti-p53 antibody for selective destruction of bladder cancer cells” SPIE Photonics West (2019)

6. H. Kim, and H. W. Kang, “Photofrin-mediated photodynamic therapy combined with fucoidan for synergistic treatment of recurrent bladder tumor” ABC 2017 (2017)

7. H. Kim, S.W. Kim, K.H. Seok, C.W. Hwang, and H. W. Kang, “Hyepericin-assisted photodynamic therapy for anaplastic thyroid cancer” IBEC 2016 (2016)

8. H. Kim, H.N. Kim, N.V. Phun, and H. W. Kang, “Development of double-layered optical tissue phantom embedded artificial vessels for Port Wine Stain laser treatment” COOC 2016 (2016)

VII. Scholastic Award

2021 **Young Investigator** in SPIE-ABC 2021 Conference
2019 **Best Paper Award** in SPIE Photonics West 2019
2017 **Student Best Award** awarded by Optical Society of Korea
2016 **Best research & Oral presentation** awarded by the Korean Society of Medical & Biological Engineering
2016 **Best Reserch & poster presentation** awarded by Optical Society of Korea

Acknowledgment

어느덧 4 년간의 박사과정이 이 학위논문을 마지막으로 끝을 맺게 되었습니다. 이 과정동안 저를 북돋아주고 진심 어린 조언과 함께 큰 도움이 되어 준 주변 동료들과 교수님들이 있었기에 이 자리가 더욱더 값진 것 같습니다. 먼저 항상 저를 지지해 주시고 든든한 조력자가 되어 주신 강현욱 교수님께 진심으로 감사드립니다. 교수님의 지도와 지원이 있었기에 제가 이 자리까지 올 수 있었다고 생각됩니다. 앞으로 더 좋은 인연으로 함께 할 날이 더욱 더 많겠지만 교수님께 배웠던 모든 소중한 것들에 감사하며 가르침을 바탕으로 사회에 이바지할 수 있도록 하겠습니다. 또한, 바쁘신 와중에도 논문심사와 함께 많은 도움을 주신 이병일 교수님, 이송이 교수님, 이명기 교수님, 그리고 이형신 교수님께도 깊은 감사를 드립니다. 특히 본 연구과제에 있어 새로운 의견과 조언을 주신 이송이 교수님께 다시 한 번 더 감사하다는 말씀을 드립니다.

박사과정 동안 저를 많이 의지하고 따라준 언제나 함께 있었던 Bio Ablation Lab 동료들 모두에게 진심으로 감사드립니다. 박사과정에 있어서 큰 도움을 주었던 황지은 후배님, 이예찬 후배님, 박사 동기로서 서로 의지하며 함께 달려온 Truong Van Gia, 아낌없는 조언을 해준 Tran Van Nam, 늦게나마 인연이 되어 앞으로 더 소중한 인연이 될 임성희 후배님, 김영은 후배님, 신화랑 후배님, 이지호 후배님, 그리고 한때 실험실 원으로 있었던 표한재 후배님, 정운영 후배님, 김명진 후배님, 박진오 모두에게 진심으로 감사드립니다. 그들의 도움이 있었기에 제가 무사히 졸업을 마칠 수 있었던 것 같습니다. 그리고 저에게 많은 학술적 도움을 주셨던 해양 융복합 바이오 메디컬 연구실 동료분들께도 이 자리를 빌어 감사하다는 말씀 전하고 싶습니다.

오랫동안 저의 바로 옆에서 격려와 응원의 박수를 보내준 소중한 친구들 황선희, 정경휘, 박란희, 이윤주, 안민우, 그리고 절친한 친구들인 고은혜, 노연주, 이 외에 미처 언급하지 못한 분들 포함 모든 분들께 감사를 표합니다.

마지막으로 나의 든든한 버팀목이자 사랑하는 아버지, 어머니, 동생 지환이, 사랑하는 가족들이 없었다면 이 긴 여정 또한 끝내지 못했을 거라 생각하며 이 논문을 바칩니다.

길었던 4 년간의 박사과정을 마치고 한걸음 더 나아가보려 합니다. 쉽지 않은 여정이 되겠지만 다시 한번 더 처음의 열정을 가지고 도전해보려 합니다. 당찬 열정을 가지고 계속해서 성장해 나가는 모습 보여드릴 수 있도록 노력하겠습니다. 감사합니다.

김혜진 올림